DOCTOR OF PHILOSOPHY

Doctoral school: Physique et Sciences de la Matière

Speciality: **Energy, Radiation and Plasma**

Plasma Rotation Study in Tore Supra Radio Frequency Heated Plasmas.

by

Billal CHOULI

Thesis publicly defended December 16th 2014, in front of committee composed of:

Dr. John Rice	MIT, *Senior research scientist*	Referee
Dr. Basil Duval	EPFL, *Senior research scientist*	Referee
Dr. Lars-Goran Eriksson	European Commission	Examiner
Dr. Christopher Klepper	ORNL, *Senior research scientist*	Examiner
Dr. Yann Camenen	PIIM, *Research scientist*	Examiner
Dr. Yanick Sarazin	CEA, *Research director*	Thesis-Director
Dr. Christel Fenzi	CEA, *Research scientist*	CEA-Supervisor
Dr. Xavier Garbet	CEA, *Research director*	Invited member

Host Laboratory:
Institut de **R**echerche sur la **F**usion par confinement **M**agnétique
CEA - Cadarache
13108 Saint-Paul-lez-Durance, France

January 2012 - January 2015

Abstract

Toroidal flows are found to improve the performance of the magnetic confinement devices with increase of the plasma stability and confinement. In ITER or future reactors, the torque from NBI should be less important than in present-day tokamaks. Consequently, it is of interest to study other intrinsic mechanisms that can give rise to plasma rotation, in order to predict the rotation profile in experiments. Intriguing observations of plasmas rotation have been made in radio frequency (RF) heated plasmas with little or no external momentum injection. Toroidal rotation in both the direction of the plasma current (co-current) and in the opposite direction (counter-current) has been observed depending on the heating schemes and plasma performance. In Tore Supra, most observations in L-mode plasmas have been in the counter-current direction. However, in this Thesis, we show that in lower hybrid current drive (LHCD), the core toroidal rotation increment is in co- or counter-current direction depending on the plasma current amplitude. At low plasma current the rotation change is in the co-current direction while at high plasma current, the change is in the counter-current direction. In both low and high plasma current cases, rotation increments are found to increase linearly with the injected LH power.

Several mechanisms in competition which can induce co- or counter-current rotation, in Tore Supra LHCD plasmas, are investigated and typical orders of magnitude are discussed. How those effects evolve with plasma parameters and how they compete are important issues addressed in this thesis. Co-current change in rotation is induced by the fast electron ripple loss mechanism while thermal ripple induced neoclassical friction and absorbed lower hybrid wave momentum from resonant electrons are expected to influence the rotation in the counter-current direction. Finally, numerical simulations of angular momentum flux show that the radial turbulent momentum transport does impact the rotation behaviour inducing change in co-current directions, with increments depending on the plasma current amplitude. The estimation of the impact of the different mechanisms shows that at high plasma current the rotation evolution in the lower hybrid phase is controlled by the neoclassical friction force due to the trapped ions in banana trajectories through the toroidal diamagnetic velocity. This force results in the counter-current increment as observed in the experimental measurement of toroidal rotation. At low plasma current the rotation is dominated by turbulent momentum transport. The Reynolds stress grows strongly compared to the high plasma current case and acts as a co-current force through its residual stress contribution. Momentum transport simulations are also performed with the CRONOS code in order to assess the rotation increments induced by LHCD. The results are rather in good agreement with the experimental observations.

Other interesting observations are related to the intrinsic plasma rotation generation with ion cyclotron resonance heating (ICRH), and have in the past few years been reported to accelerate toroidally the plasma, both in the co- and counter-current directions. In particular, there was evidence that co-current acceleration occurred during hydrogen minority heating n_H/n_D, with fairly high concentration of minority ions and during the ^{3}He minority heating. In lower minority concentration discharges, counter-current acceleration was observed. Different mechanisms affected by the minority concentration have been suggested, in particular the transferred fraction of the ICRH power to the plasma bulk and the level of supra-thermic ripple ion losses. In this Thesis, Tore Supra database has been revisited and the two trends with different minority concentration were recovered. The analysis of the different mechanisms shows that the counter-current increment observed at low minority concentration can be explained with the Laplace force due to the fast ion ripple losses and the neoclassical friction due to the increase of the ion temperature gradient. The co-current change observed at high minority concentration is considered

to be due to the turbulent momentum transport, but this effect has to be confirmed by numerical simulations of angular momentum flux.

Résumé

En présence de rotation toroïdale, une amélioration de la stabilité et des performances du plasma ont été observées. Or les sources extérieures de moment angulaire seront très limitées pour les futurs tokamaks, et notamment pour ITER. Par conséquent, il apparait capital d'investiguer les différents mécanismes de génération intrinsèque de rotation toroïdale, afin de prédire les profils de rotation dans les machines à venir. D'intrigantes observations de rotation intrinsèque sont faites dans de nombreuses machines, pour des décharges plasma en présence de chauffage à la fréquence hybride basse et cyclotronique ionique. Les profils de vitesse observés sont dans la direction parallèle au courant plasma (co-courant) mais aussi dans la direction opposée au courant plasma (contre-courant). Ceci a suscité un effort important de la communauté scientifique pour la compréhension des mécanismes à l'origine des observations expérimentales. Néanmoins, à ce jour, l'ensemble des interprétations proposées n'offrent pas une vision claire des mécanismes en jeu. Le travail réalisé dans cette thèse, s'inscrit dans cette problématique et concerne plus précisément le tokamak Tore Supra, dont le chauffage dominant est assuré par les ondes radiofréquences. Dans les plasmas de Tore Supra, les profils de rotation observés sont généralement dans la direction contre-courant.

Durant le chauffage à la fréquence hybride basse (LH), des incréments de vitesse toroïdale dans les directions co- et contre-courant sont observés. Ces observations sont fortement corrélées avec l'amplitude du courant plasma. A faible courant plasma, on observe un incrément de vitesse dans la direction co-courant, alors qu'à fort courant plasma, on observe un incrément de vitesse dans la direction contre-courant. De plus, l'amplitude de l'incrément augmente en fonction de l'amplitude de la puissance injectée. Une étude théorique a été réalisée, afin d'expliquer ces observations expérimentales. Dans un premier temps, toutes les forces à l'origine de la rotation du plasma en présence de chauffage LH sont identifiées (un terme lié à l'effet du ripple sur les électrons suprathermiques *e.g.* la force de Laplace, un terme source dû à l'injection d'ondes hybrides, un terme de friction néoclassique et un terme lié aux processus turbulents). Dans un second temps, une estimation des ordres de grandeur des différents termes est effectuée, afin d'évaluer un effet éventuellement dominant. L'impact du chauffage LH sur la rotation intrinsèque par le biais des différents termes constituant l'équation d'équilibre des moments dans la direction toroïdale peut être résumé de la manière suivante:

- L'effet de la force de Laplace sur la rotation toroïdale du plasma est en partie compensé par le terme source car ils ont un effet du même ordre de grandeur mais dans des directions opposées.
- La friction néoclassique par l'intermédiaire de la vitesse diamagnétique toroïdale gouverne la rotation toroïdale à fort courant plasma, et l'effet du chauffage LH sur la friction néoclassique avec une augmentation du gradient de la température ionique, est consistant avec les résultats expérimentaux avec un effet contre-courant.
- La turbulence par l'intermédiaire du stress résiduel semble être le terme dominant à faible courant plasma et l'effet co-courant induit est consistant avec les résultats expérimentaux.

En injectant ces termes dans l'équation de transport des moments, les résultats tendent à confirmer l'approche théorique développée dans cette thèse.

Durant le chauffage à la fréquence cyclotronique ionique (ICRH), l'évolution de la rotation semble être liée à la concentration des ions minoritaires n_H/n_D utilisée pour le chauffage minoritaire. Des expériences antérieures, sur Tore Supra, ont mis en évidence des effets sur la rotation dans la direction contre-courant

à faible concentration de minoritaire et la tendance inverse étant observée, à forte concentration de minoritaire. Les nouvelles analyses réalisées dans cette thèse confirment ces deux tendances et apporte un nouvel éclairage sur la compréhension des mécanismes en jeu. Les investigations préliminaires des différents mécanismes susceptibles d'avoir un rôle sur l'évolution de la rotation durant l'ICRH, montrent que l'effet contre-courant observé à faible concentration de minoritaire peut être expliqué par la force de Laplace due aux pertes ripple d'ions suprathermiques et à la friction néoclassique. Quant à l'effet co-courant, les phénomènes de transport turbulent sont fortement soupçonnés d'en être à l'origine. Ce mécanisme doit être confirmé par des simulations numériques de flux du moment angulaire.

Contents

I

Introduction: Thermonuclear Fusion

Il n'y a pas une crise de l'énergie, une crise de denrées alimentaires ou une crise de l'environnement. Il y a seulement une crise de l'ignorance.

Richard Buckminster Fuller

Mankind has an addiction to fossil fuels which is non-sustainable and dangerous for several reasons: burning of fossil fuels is having a measurable impact on our atmosphere and could trigger serious changes in climate, much more interesting use could be made from this resource and finally, they will run out at the same point.
The number of conceivable non-fossil candidates which in the long term could sustain the energy needs is very limited: renewables, nuclear fission and fusion. Fusion is the least developed of the three, but has particularly valuable environmental and safety advantages and has virtually inexhaustible resources.

1.1. The world energy problem

With over 7 billion people in the world and a primary power consumption of about 2.5 kW (world average), the total amount of energy currently consumed in the world is about 2.5 × 7 billion people × 1 year ≈ 16 TWyr (Terra Watt year). An estimate of what might be needed in the future years can be found with the following assumptions:

- Primary power consumption will increase by about 800 W, from 2.5 kW to 3.3 kW.
- The world population will rise to about 10 billion of people in the next 50 years (M. Singer, 2000).

In fifty years, we expect the world to consume yearly amount of primary energy equal to 30 TWyr or of about two times more than what is consumed now!
The world energy council and the international institute for applied system analysis consider three different scenarios (Figure 1.1) for the future development of the energy consumption (N. Nakicenovic et al.):

- High growth scenario with impressive technological development and high economic growth (case A)
- Middle course scenario with less ambitious and more realistic technological improvements (case B)
- Ecologically driven scenario, which represents a rich and green future, both with substantial technological improvements, strict environmental control mechanism and unprecedented international collaboration for the environmental protection (case C).

The predicted world energy consumption in the future for the three scenarios described above is shown in Figure 1.1.

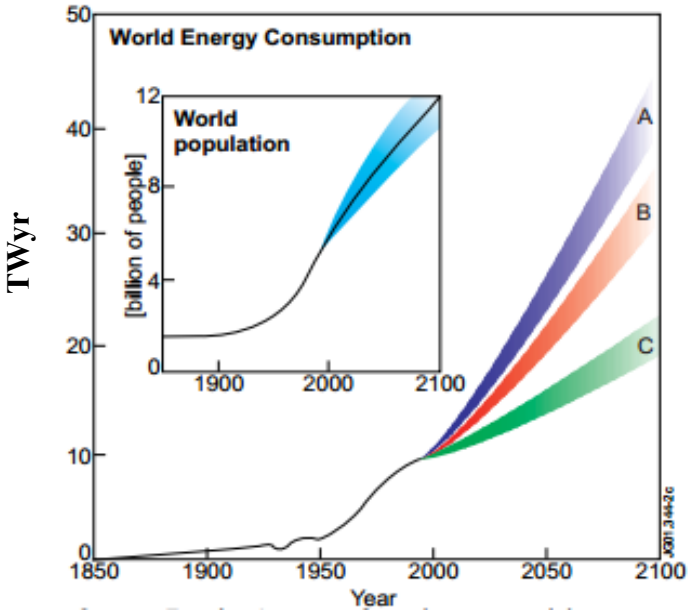

Figure 1.1. *Evolution of the world energy consumption according to three different scenarios. The inset shows the evolution of the world population. The bands reflect the uncertainties of the prediction.*

1.2. *Current energy supply and future prospects*

World primary energy consumption grew by 2.5 % in 2011, roughly in line with the 10 year average. This growth is principally due to the non-OCDE consumption which grew by 5.3 % in line with the 10 year average. Oil remains the world's leading fuel, at 33.1 % of the global energy consumption, but oil continued to lose market share for the twelfth consecutive year (www.bp.com, 2009). The world natural gas consumption grew by 2.2 % which was below the average in all regions except North America. The coal consumption grew by 5.4 % in 2011, the only fossil fuel to record above average growth and the faster growing form of energy outside renewables. Coal now counts for 30.3 % of the global consumption. This growth led by Chinese consumption. The global hydroelectric output grew by 1.6 %. Heavy rainfall drove strong growth in North America. Worldwide nuclear output fell by 4.3 % the largest decline on record, on the back of sharp declines in Japan (-44.3%) and Germany (-23.2%). Renewable energy sources saw mixed results in 2011. Global biofuel production stagnated, rising by just 0.7% or 10,000 barrels per day oil equivalent (b/doe). In contrast, renewable energy used in power generation grew by an above-average 17.7%, driven by continued robust growth in wind energy (+25.8%), which accounted for more than half of renewable power generation for the first time. Solar power generation grew even more rapidly (+86.3%), but from a smaller base. Renewable forms of energy accounted for 2.1% of global energy consumption, up from 0.7% in 2001 (United Nations, 2009). The Figure 1.2 shows the world energy consumption evolution since 1860 to 2010.

.

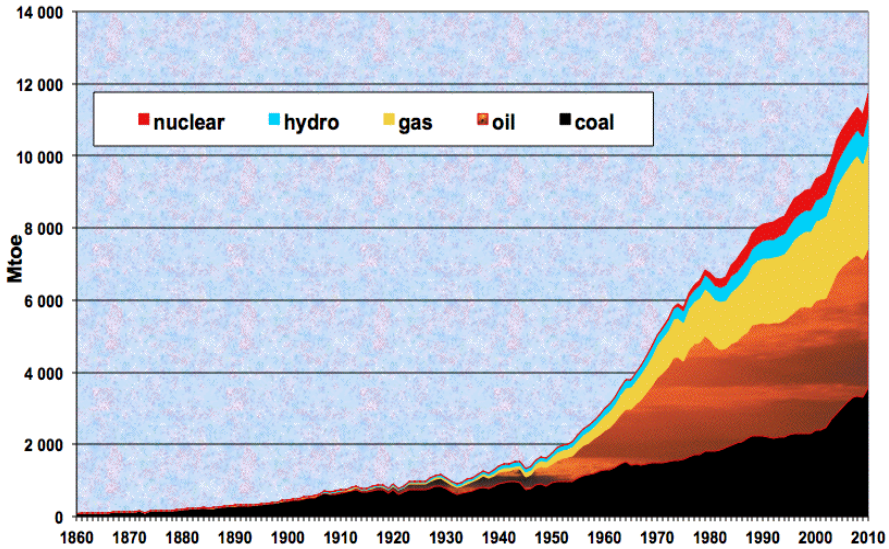

Figure 1.2. *Evolution of the world energy consumption (excluding biomass) since 1860. Sources : (Schilling & Al. (1977), IEA (2002), Observatoire de l'Energie (1997.))*

From the Figure 1.2, we can see that 90 % of our energy is currently produced by burning fossil fuels. This could pose serious problems in the future. First, depletion of the world resources will inevitably lead to political instabilities in the world. The second and most worrisome problem is the consequences to our environment of the massive use of the fossil fuels due to the inevitable release of gigantic quantities of CO_2 in our atmosphere. Measurements show a very steep increase of the CO_2 contents in the atmosphere during the few last decades (DOI-EIA, 2010; F. Joos, 1996). This can be clearly observed in Figure 1.3.

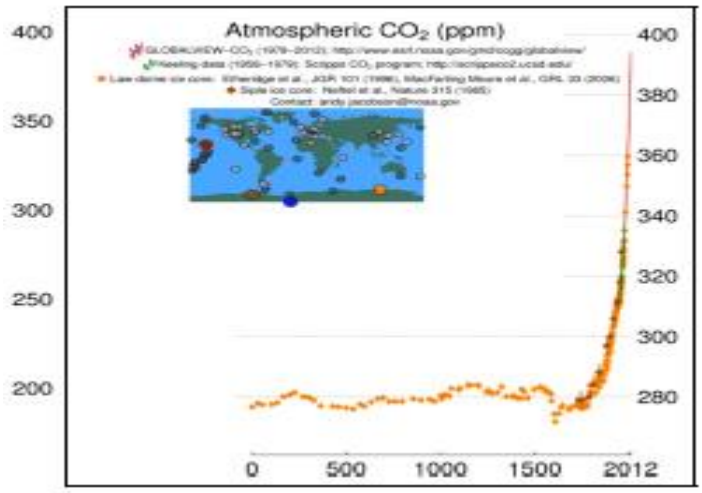

Figure 1.3. *Evolution of the CO_2 concentration in the atmosphere (in ppm) during the last 1000 years* **(Dr. Pieter Tans; F. Joos, 1996)**.

CO_2 is a greenhouse gas, and a higher concentration of this gas will lead to an increased absorption of the infrared radiation re-emitted by the earth. There is general agreement among specialists that this will cause the average temperature on earth to rise. What will happen to our environment if the average temperature increases? This is a most difficult question. Our ecosystem is very complex, with much feedback and as such probably buffered against, and able to adapt to sudden changes. However, as is the case for buffers in chemistry, there are limits to the adaptability of our ecosystem and the question remains: what are these limits? In which direction will the ecosystem evolve as soon as the stability thresholds are crossed?
Our energy production scheme leads to a possibly irreversible geophysics situation which represents the most threat for our environment.
To reduce the risk of such dramatic changes, humankind has to change its way of consumption and reduce or even stop burning fossil fuels and try to use other energy sources as soon as possible.
The only long term alternatives to burning fossil fuels are renewables, fission and fusion. Renewable energy sources in the world are large and inexhaustible, they have unfortunately only, a limited potential in term of energy density and intermittence (David.JC. Mackay, 2009). In the case of fission, highly radioactive waste is produced, but the volume is rather low and most of the irradiated fuel can be in principle reprocessed and reused in other reactors. The third option is the fusion facility. It is safe, with inexhaustible fuel and clean. The fusion could be a good compromise between the nature and the energy needs of mankind. This point of

view is confirmed by a recent study carried out by the European Commission (I. Cook et al., 2001).

The development of nuclear fusion as an energy source is one of the most complex scientific and technical tasks ever undertaken for non-military purposes and will still span several human generations. There exist presently two approaches to realise nuclear fusion on earth: inertial and magnetic fusion. Inertial fusion consists of micro-explosions of small fuel pellets by means of powerful lasers or particle beams. Confinement of the fuel is based on the inertia of the pellet fuel mass, which resists the natural expansion when it is heated to thermonuclear fusion temperatures. Magnetic fusion uses magnetic fields to confine the fuel. The European fusion effort is concentrated on the latter and hence we will briefly review only this method here. The interested reader can find a wealth of additional information in the references (J.P.Holdren et al., 1987; R.W.Conn et al., 1990). In the coming paragraph we will discuss the fusion reaction.

1.3. Nuclear fusion processes and thermonuclear fusion

The fusion reaction is the process where two light nuclei fuse to form a heavier nucleus. It is found that the mass of two light nuclei is larger than the mass of the fusion products. The difference of mass is then converted to the energy according to the Einstein's well known formula $E = mc^2$. The least fusion reaction to initiate on earth is that between the Hydrogen isotopes Deuterium D and Tritium T:

$$D + T = {}^{4}_{2}He\ (3.5\ MeV) + n\ (14.1\ MeV)$$

In which the Deuterium constitutes the stable isotope and Tritium the radioactive isotope of Hydrogen. To produce sufficient fusion reactions the temperature of the plasma has to be on the order of 100 to 200 million °C for this reaction. Fusion reaction is shown in Figure 1.4.
The reaction products are an α-particle and very energetic neutron. Twenty percent of the energy is taken by the α-particles which are confined, owing to their charge, and deliver their energy to the bulk plasma. In this way, they compensate the losses and might make the reaction self-sustaining. The kinetic energy of the fast neutrons will be converted to heat in a blanket and then into electricity using conventional technology. The fusion reaction releases about one million times more energy than the chemical one per mass unit.
To be self-sustained, the fusion reaction has to fulfill a criterion which consists on product of three parameters: the temperature T, the density n and the confinement time τ_E.

$$n\,T\,\tau_E > 5.10^{21} \quad keV\,s/m^3$$

The above criterion is the so-called Lawson criterion. The higher the product, the better the fusion reaction. We can see from this criterion that we need to have high temperature and high density in order to have enough collisions between the nuclei and we should confine the plasma energy.

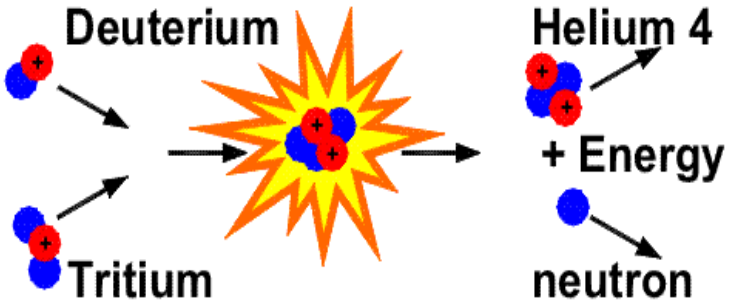

Figure 1.4. *The two hydrogen isotopes, deuterium and tritium fuse to form helium and a neutron. This reaction releases 17.6 MeV.*

In order to have a reasonable cross-section for the deuterium-tritium reaction a temperature of 1 to 10 keV (1 eV ≈ 12000 °C) is needed. In order to keep the plasma at such high temperatures we should avoid contact between the plasma and any material wall. A possible way of doing that is to use a magnetic trap that confines the plasma in the center of a vacuum chamber.

1.3.1. Tokamaks

The Lorentz force makes the particles move in helical orbits around the magnetic field lines. In a uniform magnetic field and in the absence of collisions or turbulence, the particles remain tied to the field lines but are free to move along them (Figure 1.5).

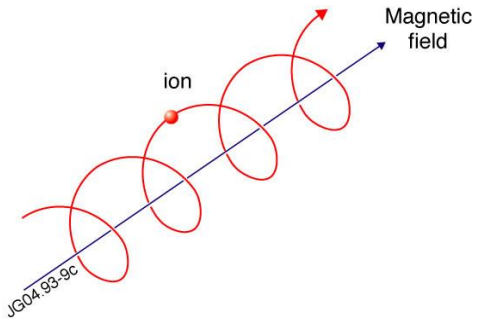

Figure 1.5. *Charged particle gyration around the magnetic field line. The geometry of the magnetic field determined the geometry of the plasma which consists of charged particles.*

The distance between the particle orbit and the magnetic field line is the Larmor radius $\rho_L = v_\perp/\omega_c$ where ω_c is the cyclotron frequency of the particle and $v_\perp$ the particle velocity

perpendicular to the magnetic field. The magnetic field is thus capable to restrict the particle motion perpendicular to the magnetic field but does not prevent from the parallel motion. In order to confine the plasma effectively the field lines should therefore close on themselves, hence form a toroidal geometry. A torus shaped vacuum vessel with a toroidal magnetic field is sufficient to confine the plasma. The curvature of the magnetic field causes particle drifts resulting in an electric field. This electric field in its turn leads to an outward drift of all particles and therefore to a loss of confinement. To avoid this effect, a poloidal magnetic field should be added. In a tokamak the poloidal magnetic field is generated by the toroidal plasma current (Figure 1.6). This plasma current is induced by a transformer, using the plasma as the secondary winding. In addition, radial and vertical components are added to the magnetic field by external positioning coils. The Figure 1.6 shows the magnetic configuration of a tokamak with the different magnetic coils. The plasma electric current is also illustrated.

It is important to mention that there are other magnetic configurations to confine the plasma, such as the stellarator and reversal field pinch.

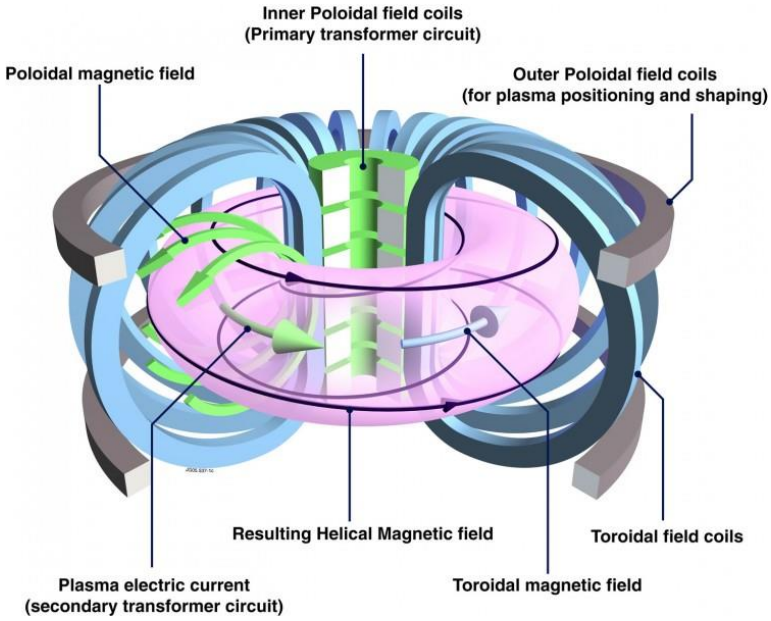

Figure 1.6. *The magnetic confinement in a Tokamak. For stability reasons an helical magnetic field is needed. The toroidal component comes from the field coils, the poloidal component is induced by the plasma current. Making the plasma column the secondary winding of a transformer, high plasma current can be reached by feeding a current ramp to the primary winding of the transformer.*

Poloidal and toroidal components add up to a set of helical field lines. These field lines lie on magnetic surfaces. The magnetic structure in a tokamak can be seen as an infinite set of nested magnetic flux surfaces. An important parameter in tokamak physics is the safety factor *q:*

$$q = \frac{m}{n} \approx \frac{rB_\phi}{RB_\theta} \qquad 1.3.1$$

It describes the number of toroidal windings of a field line needed for one poloidal winding (e.g. m=3, n=2 means that, when you follow a field line on this q = 3/2 surface, you need 3 toroidal windings and 2 poloidal windings to reach your starting point again, or 1.5 toroidal windings for 1 poloidal winding). At places with a (low) rational q-number instabilities can easily arise. The effect of a minor fluctuation at a certain position is amplified because the particles pass every q toroidal revolutions at that same position.

1.4. The crucial role of plasma rotation:

To achieve the fusion reaction, the plasma must fulfill three main criteria:

- The first criterion is the Lawson criterion, which states that the energy, density and particle confinement must be high. The input energy into the plasma has to be confined sufficiently long. In a fusion reactor we therefore have to minimize the energy transport to the wall.
- The plasma confinement has also to be stable. Because the plasma is confined by the magnetic field and many magnetic instabilities can develop, the understanding of the magnetic stability is necessary to avoid the instabilities.
- The power that goes into a fusion reactor eventually ends up at the wall of the reactor. In order to optimize the first wall materials, to face the power flux and keep the impurities and dust far from the core plasma, a good understanding of the plasma wall interaction is needed.

In tokamak, the confinement of the plasma is governed by the transport of particles, energy and momentum. The confinement is degraded when the transport increases. For the momentum for example, an indicator of the confinement is the momentum confinement time (that is the time in which the momentum is lost when the sources are switched off) which is of the order of tens of milliseconds. In the plasma coexists two different transports: the neoclassical and turbulent transport. The neoclassical transport is due to the collisions between the species. These collisions are characterized the collision time (the inverse of the collision frequency) of the order of the milliseconds for ions. The turbulent transport is due to the temperature and density gradients inducing micro-instabilities in the plasma as illustrated in Figure 1.7. It shows the ion temperature and density profiles as a function of the flux coordinate where we can see the strong gradients between the core and the edge of the plasma. The characteristic time (or correlation time) of turbulence is around the microsecond.

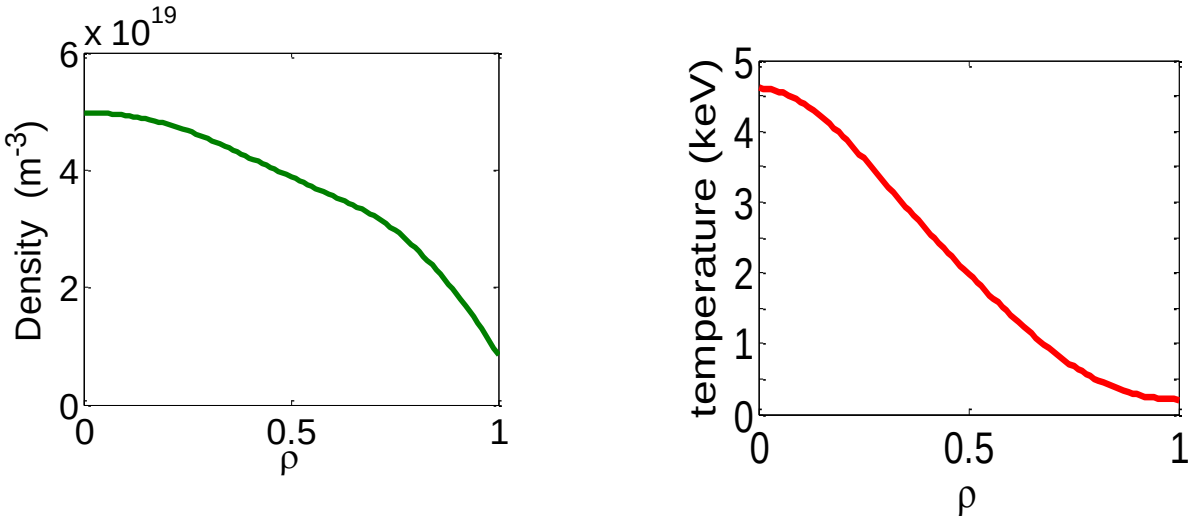

Figure 1.7. *Typical electron density (left) and temperature (right) profiles in Tore Supra. A strong gradient between the core and the edge of the plasma is observed.*

Several experiments in the world have shown that high plasma rotation can contribute to the first two criteria: the improvement of confinement (by reducing the transport such as the turbulent transport) and plasma stability (by stabilizing the MHD modes such as the resistive wall modes).

Now, the mechanism of suppression of turbulence by rotational shear is well admitted. The turbulent transport results from the fluctuations with a radial correlation length and a correlation time. These fluctuations represent turbulent cells. A sheared flow (different velocity at each radial point) will shred these turbulent cells apart, leading to smaller cells (H. Biglari et al., 1990). In (Z. Lin et al., 1998) it is clearly shown that the turbulent cells are much smaller in the case with flows than without flows. The straightforward method to increase the velocity gradient is to increase the velocity since the wall of the vessel does not move, the gradient will be larger if the plasma rotates fast.

Apart from improving the confinement, the plasma rotation increases the stability of the magnetic configuration. Sources of free energy in the plasma can break and reconnect the nested flux surfaces. The reconnected flux surfaces due to the change in magnetic configuration are called tearing modes. These magnetic islands are unfavorable for the confinement and can cause disruptions. This is why we try to avoid them. External perturbations can also create magnetic islands for example the misalignment of the coils which creates an error field. Because no machine is perfectly aligned and perfectly symmetric, magnetic islands exist in every fusion device.

The tearing modes are suppressed when the plasma rotates. The interaction between the suppressed tearing modes and the error field will slow down the plasma. Once the suppressed tearing modes are at rest in the frame of the error field, large tearing modes will develop. This is called mode excitation. A high threshold for mode excitation is expected at high plasma rotation, because the error field needs to slow down the plasma to great extent.

Another type of magnetic instability is the resistive wall mode (RWM). They occur at high plasma pressure. When they lock (they don't move with respect to the vessel wall), they cause disruptions. For high β (the ratio between the kinetic pressure and the magnetic pressure, it represents the efficiency of confinement) machine the prevention of the RWM's is therefore crucial. In fast rotating plasma the RWM's will be suppressed and the interaction between the

suppressed RWM's and the conducting tokamak wall will slow down the plasma. Once the RWM is at rest with respect to the wall the RWM grows and causes disruption.

In the plasma, the rotation results from source of momentum, transport and boundary conditions. The momentum source combined to the boundary condition lead to the rotation profile in the experiments driven by the momentum transport. The process is governed and described by the momentum balance equation (or momentum transport equation). The Figure 1.8 shows this mechanism with an arbitrary source of momentum and boundary condition.

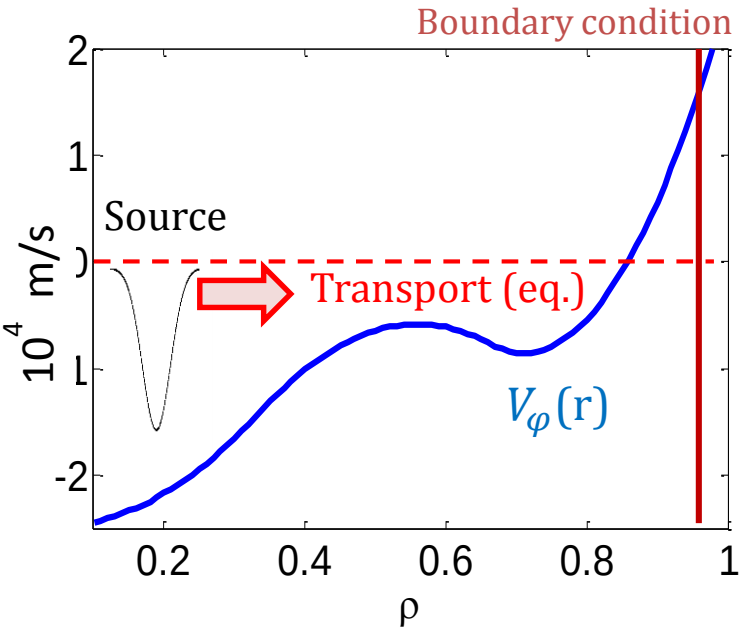

Figure 1.8. *Mechanism leading to the rotation profile in the plasma with a momentum source, a boundary condition and transport.*

In order to benefit from the advantages of plasma rotation, it is crucial to know how the plasma rotation improves the confinement and stability of the plasma and how a large plasma rotation can be driven.

1.5. Context of this thesis

Above, the main beneficial aspects of plasma rotation were mentioned: increase of the plasma stability against the tearing and resistive wall modes and turbulence suppression by flow shear. In today's tokamaks, the greatest source of torque (momentum) on the plasmas is due to neutral beam injection (NBI). On the other hand, in ITER or future reactors the torque from NBI should be less important than in present-day tokamaks and is expected to be low. There are several reasons for this; one is that the injected momentum scales as $P_{NBI}/\,E_{inj}^{1/2}$ and that the injection energy must be much higher in dense and high volume reactor plasma than in today's machines (L-G. Eriksson et al., 2009). Consequently, it is of interest to study other mechanisms

that can give rise to plasma rotation. Intriguing observations of plasma rotation have been made in radio frequency (RF) heated plasmas with little or no external momentum injection (L-G. Eriksson et al., 1992; A. Scarabosio et al., 2006); this phenomenon is often referred to as

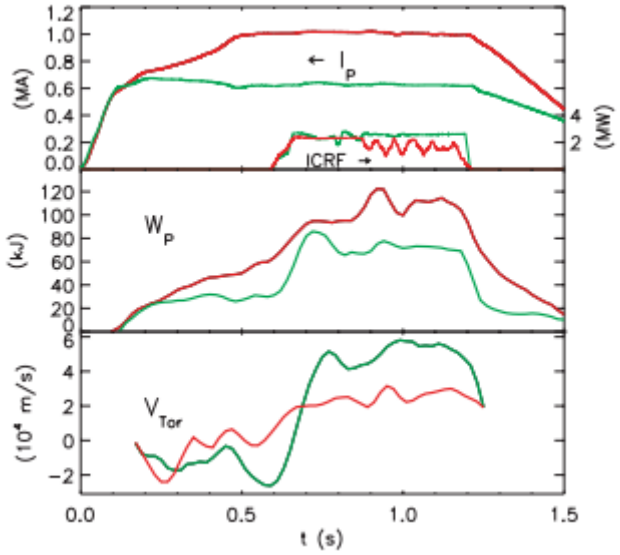

Figure 1.9. *Time histories of plasma current and ICRF pulse (top), plasma stored energy (middle) and argon toroidal rotation velocity (bottom) for a 0.6 MA discharge (green) and a 1.0 MA discharge (red)* **(J.E. Rice et al., 1999)**. *A significant change is observed in toroidal rotation is observed during the ICRH, in the co-current direction.*

'intrinsic' or 'spontaneous' rotation. The rotation evolution during radio-frequency heating is shown in Figure 1.9. The toroidal rotation is found to be modest with small external momentum input in the plasma compared to the plasmas heated by the NBI. Hence, an important question arises: is the observed intrinsic rotation significant enough to suppress the turbulence and increase the plasma stability (RWM stabilization) in ITER and future reactors? Unfortunately, the origins of the spontaneous rotation are not really understood and it is at present difficult to predict and develop models of the plasma rotation.

Toroidal rotation in both the direction of the plasma current (co-current) and in the opposite direction (counter-current) has been observed depending on the heating schemes and plasma performance. Most observations in H-mode plasmas have been in the co-current direction, while the trend in L-mode plasmas is less clear.
One of the first questions that will be addressed in this thesis is therefore:

- **How does the toroidal plasma rotation in L-mode Tore Supra discharges evolve during the radio frequency heating (LHCD and ICRH)?**

To answer this question, a large database of LHCD and ICRH plasmas is analysed. Scans of plasma rotation as a function of different parameters are realised in order to better understand the rotation behaviour in the plasma.

Another point is that, there are likely different dominant mechanisms behind the observed rotation in L- and H-mode plasmas. Intensive work is therefore initiated to establish a multi machine database in order to study the scaling of the plasma rotation with different plasma parameters. This scaling is shown in Figure 1.10 and indicates that the extrapolated intrinsic rotation for ITER using an empirical scaling law might be sufficient to stabilize the turbulence and the RWMs (J. Rice et al., 2007).

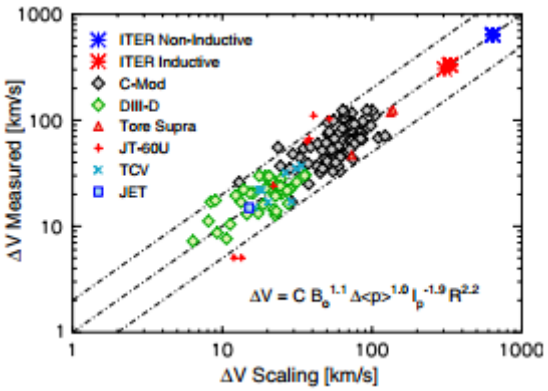

Figure 1.10. *The measured change in the rotation velocity as a function of the scaling with* $\Delta \boldsymbol{V} = \boldsymbol{C}\, \boldsymbol{B_0^{1.1}} \Delta \boldsymbol{P^{1.0}} \boldsymbol{I_p^{-1.9}} \boldsymbol{R^{2.2}}$*. strong intrinsic rotation is predicted for ITER* **(J. Rice et al., 2007)**.

To be confident in predictions for ITER and future machines, it is important to develop a better understanding of the mechanisms behind the intrinsic rotation with efforts in theory development, transport simulations and pertinent new experiments. While it is important to understand rotation in H-mode plasmas, which is the main focus in (J. Rice et al., 2007), it is also of interest to gain a better understanding of its origin in L-mode plasmas (the plasma is in L-mode before its transition to the H-mode).
The second question that will be discussed is:

- **What are the different mechanisms that govern the intrinsic plasma rotation and how do they evolve during the LHCD and ICRH?**

To answer this question, the different mechanisms involved in intrinsic rotation are analyzed and an estimation of their impact on toroidal rotation during the RF heating is calculated.
Several theories aimed at understanding the origin of the intrinsic rotation have been developed, since many initial observation of rotation with low momentum input were reported in ICRH and LHCD plasmas. Theories related to the fast accelerated particles (electrons and ions) have been proposed. Counter-current resp. co-current rotation could be due to the loss of fast trapped ions resp. electrons. The finite orbit width effects (F.W. Perkins et al., 2001) and the spatial transport of the resonating ions induce a radial transport of the toroidal angular momentum (the integral of the angular momentum over the plasma is null). The mechanism predicts co- resp. counter- current rotation if the inner lobe of the dipolar torque is in the co- (low field side) resp. counter- current (high field side) direction. This change has not been supported by experimental results (L-G. Eriksson and F. Porcelli, 2002). Another possibility

investigated in (L-G. Eriksson and F. Porcelli, 2002) is the wave particle momentum transfer due to the differential absorption of launched power by resonating particles (difference between the positive and the negative toroidal mode numbers). The experimental evidences for ICRH antennas where the phasing of the antennas was varied from launching waves propagating predominantly in the direction of the plasma current to counter-current propagating ones show that this effect does not induce a significant change in toroidal rotation (L-G. Eriksson et al., 2004).
Investigations of rotation on bulk plasma and in ohmic phase are important, since the effects directly related to the heating mechanisms and fast particles do not explain the observed rotation. The neoclassical theory predicts counter-current rotation in the core plasma (M.N. Rosenbluth et al., 1971). For the edge rotation, a co-current rotation is predicted by neoclassical theory in the Pfirsch-Schlüter regime while in the Banana regime a counter-current rotation is predicted (A.L. Rogister et al., 2002). The Figure 1.11 shows the neoclassical rotation profiles for carbon and deuterium impurities and the measured CXRS toroidal rotation. A rather good agreement is observed between the measured and neoclassical rotations. Neoclassical effects due to the symmetry breaking with the magnetic field ripple can also influence the plasma rotation. The thermal friction force due to the radial flux generated by banana particle which banana tips perturbed by the ripple perturbation and also due to the collisions of banana particles with passing ones is also identified to influence the plasma rotation. These effects related to ripple are expected to be significant in Tore Supra.

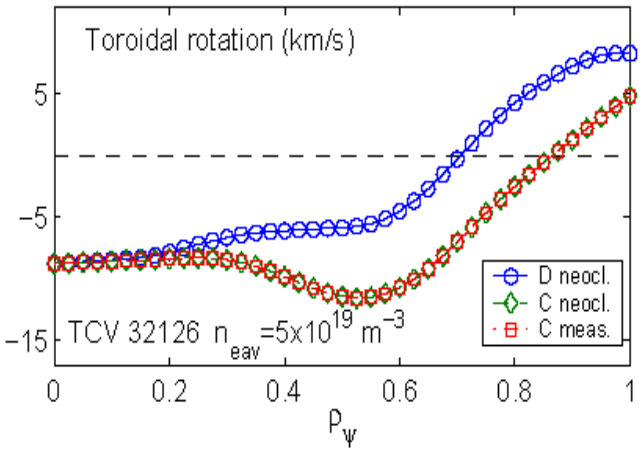

Figure 1.11. *Measured carbon toroidal rotation and calculated carbon and deuterium neoclassical rotation profiles in TCV (B. Duval, 2nd EFDA TTG Workshop, September 2009, JET).*

Other potential mechanisms are offered by the turbulent or anomalous transport which can drive rotation in the plasma. An example is given by the so called accretion theory where the preferential direction of the turbulent modes in the edge of the plasma is invoked to provide a torque on the plasma. It suggests a co-current rotation in H-mode (B. Coppi et al., 2002). Another theory is related to the flow driven in the scrape off layer by ballooning type transport. The effect of this theory on the plasma rotation is dependent on the grad-*B* drift (B. LaBombard et al., 2004). The $E \times B$ shear in the plasma leads to different pinch terms in the transport equation for the angular momentum (O.D. Gurcan et al., 2007). This pinch term can explain

the co-current accelerations observed at the transitions to H-mode. A Coriolis drift effect has also been discussed in (A.G. Peeters, 2007). It acts as a pinch term in toroidal rotation.
The above overview of mechanisms that could impact the toroidal plasma rotation with little external momentum input shows the complexity of the problem. Many theories are proposed but no dominant mechanism is identified. There is no doubt that several of them may be contributing for any given discharge.
Consequently, the third question that will be addressed in this work is:

- **What are the dominant mechanisms responsible for the rotation evolution during the LHCD and ICRH in Tore Supra?**

To answer this question and to assess the importance of individual effects, a large database of experimental discharges with reliable toroidal rotation measurements is analysed. Then an estimation of the effect of each mechanism on toroidal rotation is completed. Numerical simulations of the torque exerted on the bulk plasma due to the RF heating and transport simulations are also carried out.

The thesis is structured as follows: In chapter II, the basic theoretical framework of plasma rotation is introduced. A selection of pertinent information and theories is made from the literature. In chapter III, the Tore Supra tokamak is introduced with the main diagnostics used in this thesis, as the charge exchange recombination spectroscopy technique which will be discussed in detail.

In chapter IV, we analyse the measurements of toroidal plasma rotation during Lower Hybrid (LH) and Ion Cyclotron Resonance Frequency (ICRF) heating. The main trends of the toroidal rotation depending on plasma parameters are extracted, and the obtained results are compared to other machines such as JET and C-Mod.

In chapter V, we investigate the different mechanisms involved in the intrinsic rotation in order to explain the experimental observations. The estimation of the impact of each effect is realised, and the dominant mechanisms are extracted.

Finally, in the chapter VI, the main conclusions are discussed and put into perspective with what should be expected in ITER.

1.6. List of publications and contributions to conferences

In this section, a list of publications and conference contributions achieved during this thesis is given.

[1] **B Chouli**, C Fenzi, X Garbet, C Bourdelle, J Decker, T Aniel, J-F Artaud, V Basiuk, F Clairet, G Colledani, R Dumont, D Elbeze, C Gil, P Lotte, Y Sarazin, and the Tore Supra Team. "Co- and counter-current rotation in Tore Supra lower hybrid current drive plasmas". Plasma Phys. Control. Fusion **56** (2014) 095018 (8pp) http://stacks.iop.org/0741-3335/56/095018

[2] **B. Chouli**, C. Fenzi, X. Garbet, C. Bourdelle, Y. Sarazin, J-F. Artaud, B. Baiocchi, P. Cottier, J. Decker, J. Rice, M. Schneider, V. Basiuk, T. Aniel, F. Imbeaux, M. Irishkin, D. Mazon and the Tore Supra team. "Investigations of LHCD induced plasma rotation in Tore Supra ". Submitted to Nuclear Fusion.

[3] J. E. Rice, Y. A. Podpaly, M. L. Reinke, R. Mumgaard, S. D. Scott, S. Shiraiwa, G. M. Wallace, **B. Chouli**, C. Fenzi-Bonizec, M. F. F. Nave, P. H. Diamond, C. Gao, R. S. Granetz, J.W. Hughes, R. R. Parker, P. T. Bonoli, L. Delgado-Aparicio, L.-G. Eriksson, C. Giroud, M. J. Greenwald, A. E. Hubbard, I. H. Hutchinson, J. H. Irby, K. Kirov, J. Mailloux, E. S. Marmar, and S. M. Wolfe "Effects of Magnetic Shear on Toroidal Rotation in Tokamak Plasmas with Lower Hybrid Current Drive". PRL **111**, 125003 (2013) http://prl.aps.org/pdf/PRL/v111/i12/e125003

Conference contributions

B Chouli, C Fenzi, X Garbet, C Bourdelle, J Decker, T Aniel, J-F Artaud, V Basiuk, F Clairet, G Colledani, R Dumont, D Elbeze, C Gil, P Lotte, Y Sarazin, and the Tore Supra Team. "Co- and counter-current rotation in Tore Supra lower hybrid current drive plasmas". 40 th EPS Conference on Controlled Fusion and Plasma Physics (2013).

B. Chouli, C. Fenzi, X. Garbet, C. Bourdelle, Y. Sarazin, J-F. Artaud, B. Baiocchi, P. Cottier, J. Decker, J. Rice, M. Schneider, V. Basiuk, T. Aniel, F. Imbeaux, M. Irishkin, D. Mazon and the Tore Supra team. "Investigations of LHCD induced plasma rotation in Tore Supra ". 41 st EPS Conference on Controlled Fusion and Plasma Physics (2014).

C. Fenzi, **B. Chouli**, R. Dumont, D. Elbeze, Z. O. Guimarães-Filho, P. Hennequin, P. Lotte, P. Maget and the Tore Supra team. " RF driven rotation in Tore Supra". 17th Joint EU-US Transport Task Force Meeting, Padova - September 3-6, 2012.

B. Chouli, C. Fenzi, X. Garbet, C. Bourdelle, Y. Sarazin, J-F. Artaud, B. Baiocchi, P. Cottier, J. Decker, J. Rice, M. Schneider, V. Basiuk, T. Aniel, F. Imbeaux, M. Irishkin, D. Mazon and the Tore Supra team. "Investigations of LHCD induced plasma rotation in Tore Supra ". ITPA meetings (2014).

H.P. Laqua, E. Chlechowitz, **B. Chouli**, S. Marsen, T. Stange, M. Otte, J. Urban. "Multi-frequency microwave heating and current drive in over dense plasmas at the WEGA stellarator". 38th EPS Conference on Controlled Fusion and Plasma Physics (2011).

II

Theory of plasma rotation

As far as the laws of mathematics refer to reality, they are not certain; and as far as they are certain, they do not refer to reality

Albert Einstein

Before getting to the heart of the matter and answering the questions raised in the previous chapters, a theoretical framework is necessary. The theory of the plasma dynamics is well described in the literature (D. J. Tritton, 1977; J. Wesson, 1997; R.J. Rutherford and P.H. Goldston, 1995). In this chapter, we have selected all the information needed to deal with plasma rotation.

We start with the general description of the plasma as a collection of different individual charged particles, in electromagnetic environment. Considering each species as a fluid in a collective description, the fluid model is then derived.

At this point, the magnetic configuration of the plasma comes to the discussion. We will show that the magnetic configuration of the plasma consists of nested flux surfaces. The fluid velocity can therefore be split in two parts, the fluid velocity perpendicular to the flux surfaces (convection) and the fluid velocity parallel to the magnetic flux surfaces (called rotation). After

that, considering the toroidal geometry of the tokamak, the fluid velocity can be split in toroidal and poloidal components.

Afterwards, the physical mechanisms underlying the plasma rotation are examined. The sources, sinks and transport of the momentum are discussed. Classical, neoclassical and turbulent transports are therefore addressed. We will also show that, from the neoclassical theory the plasma has tendency to rotate spontaneously. This intrinsic or spontaneous rotation which is beneficial for the plasma confinement and stability is then considered.

Finally, an introduction to the ripple theory is developed since it influences the plasma rotation (symmetry breaking). Different mechanisms inducing ripple in the plasma are given and the role of ripple in plasma rotation is then discussed.

2.1. Fluid description of the plasma

The plasma is constituted by a large collection of particles: neutrals, ions and electrons. The behaviour of the particles in the plasma is described by the kinetic equation (or Boltzmann equation in magnetised plasmas) in terms of the distribution function $f_\alpha(\boldsymbol{x},\boldsymbol{u},t)$ of the particle α (α being ion or electron), where $\boldsymbol{x}$ describes the position and $\boldsymbol{u}$ the velocity in a six Dimensional phase space. This model is a function of seven dimensions. For many purposes (numerical limitations), it is adequate to simplify this kinetic model by the fluid model, in term of moments of the distribution function (macroscopic variables) such as the particle density $n_\alpha(\boldsymbol{x},t)$, fluid velocity $V_\alpha(\boldsymbol{x},t)$ and pressure $P_\alpha(\boldsymbol{x},t)$ which are functions of only four dimensions.

The fluid equations derive from the Boltzmann equation:

$$\frac{\partial f_\alpha}{\partial t} + \boldsymbol{u}.\frac{\partial f_\alpha}{\partial \boldsymbol{x}} + \frac{q_\alpha}{m_\alpha}(\boldsymbol{E}+\boldsymbol{u}\times\boldsymbol{B}).\frac{\partial f_\alpha}{\partial \boldsymbol{u}} = \left(\frac{\partial f_\alpha}{\partial t}\right)_c \qquad (2.1)$$

where $q_\alpha(\boldsymbol{E}+\boldsymbol{u}\times\boldsymbol{B})$ is a force on the particle namely the Lorentz force, $\boldsymbol{u}$ is the phase space velocity which is distinguished from the fluid velocity $\boldsymbol{V}$ and $\left(\frac{\partial f}{\partial t}\right)_c$ is the collision operator. Collisions between different plasma species result in friction forces (momentum sources), viscosity (momentum transport) and resistivity. The Boltzmann equation coupled to Maxwell equations constitutes the kinetic model. This model is simplified by the fluid model multiplying the equation 2.1 by chosen moment A of this equation and integrating over the velocity space to obtain equations for:

$n_\alpha = \int f_\alpha(\boldsymbol{x},\boldsymbol{u},t)\, d^3\boldsymbol{u}$,

$\boldsymbol{V_\alpha} = \frac{1}{n_\alpha}\int f_\alpha(\boldsymbol{x},\boldsymbol{u},t)\,\boldsymbol{u}\, d^3\boldsymbol{u}$,

$\boldsymbol{P_\alpha} = m_\alpha \int f_\alpha(\boldsymbol{x},\boldsymbol{u},t)\,(\boldsymbol{u}-\boldsymbol{V_\alpha})\otimes(\boldsymbol{u}-\boldsymbol{V_\alpha})\, d^3\boldsymbol{u}$,

where $\boldsymbol{P_\alpha}$ is the pressure tensor. For an isotropic distribution function the pressure is a scalar and is given by:

$$p_\alpha = \frac{1}{3}\, m_\alpha \int f_\alpha(\boldsymbol{x}, \boldsymbol{u}, t)\, (\boldsymbol{u} - \boldsymbol{V_\alpha})^2\, d\boldsymbol{u}$$

Thus, the first moment ($\mathrm{A} = 1$) of the equation 2.1 gives the reconstituted mass conservation equation:

$$\frac{dn_\alpha}{dt} + n_\alpha\, \nabla .\, \boldsymbol{V_\alpha} = 0 \qquad (2.2)$$

The momentum conservation equation is obtained by taking the $m\boldsymbol{u}$ moment of the equation 2.1:

$$n_\alpha m_\alpha \left(\frac{\partial \boldsymbol{V_\alpha}}{\partial t} + \boldsymbol{V_\alpha}.\nabla \boldsymbol{V_\alpha}\right) = q_\alpha n_\alpha (\boldsymbol{E} + \boldsymbol{V_\alpha} \times \boldsymbol{B}) - \nabla . \boldsymbol{P}_\alpha + \boldsymbol{R_\alpha} \qquad (2.3)$$

where $\boldsymbol{R_\alpha}$ is the collision term and represents the change of momentum due to collisions with all other species. The pressure tensor can be split into a scalar pressure part p and an anisotropic part $\boldsymbol{\pi}$, which gives: $\boldsymbol{P} = p\boldsymbol{I} + \boldsymbol{\pi}$. $\boldsymbol{\pi}$ depends on collisions and the velocity gradient, and gives rise to the resistivity. It also describes the plasma viscosity, and is therefore also called the viscous tensor. The scalar pressure is related to the density and temperature via: $p = nT$.

The equation 2.3 is also known as the force balance equation and it is indeed similar to the Newton's law: $m\left(\frac{\boldsymbol{dV}}{dt}\right) = \boldsymbol{F}$ where $\boldsymbol{F}$ is the sum of the forces**.** It is seen from the above procedure that each conservation equation of specific moment introduces a higher order moment. The procedure doesn't therefore lead to a closed set of equations. Closure is usually achieved by making simplifying assumptions in the equation of pressure tensor $\boldsymbol{P_\alpha}$**.** For example, it is often assumed that the motion is adiabatic $\frac{\boldsymbol{d}}{dt}(p\rho^{-\gamma}) = 0$ where ρ is the mass density, or that the third moment, the heat flux vector, may be calculated using a simple form of thermal conduction.
The fluid model assumption is valid when the particle behavior is sufficiently localized. This is achieved if the mean free path of the particles is sufficiently small compared to the macroscopic lengths under-consideration. At high temperature the mean free path is long and the justification of the equations is not valid so far. Combining the fluid equations for ion and electrons, and together with the Maxwell equations form the magnetohydrodynamics (MHD) model.

When considering two particle species in the plasma: ions and electrons, in this case, the mass density reads $\rho = n_i m_i + n_e m_e$ and the center mass of fluid velocity $\boldsymbol{V} = \frac{\boldsymbol{V}_i n_i m_i + \boldsymbol{V}_e n_e m_e}{n_i m_i + n_e m_e}$. Due to the mass ratio $\frac{m_e}{m_i} \ll 1$, and the quasi-neutrality $n = n_e = n_i$, the mass density can be approximated by $\rho = n_i m_i = nm$ and the center mass velocity $\boldsymbol{V} = \boldsymbol{V}_i$. Therefore, the mass of the plasma is dominated by the mass of ions $m = m_i$ and the average fluid velocity of the plasma by the ion fluid velocity $\boldsymbol{V}_i$.

The charged particles move in helical orbits around the magnetic field lines due to the Lorentz force. In a uniform magnetic field and in the absence of collisions or turbulence, the particles remain tied to the field lines but are free to move along them. The ion motion can therefore be decomposed into components parallel and perpendicular to the magnetic field (P. Helander and D.J. Sigmar, 2002):

$$\boldsymbol{V}_i = \boldsymbol{V}_{i,\perp} + \boldsymbol{V}_{i,\parallel} \qquad (2.4)$$

Within the adiabatic limit, the transversal fluid velocity at first order of development can be written as:

$$\boldsymbol{V}_{i,\perp} = \frac{\boldsymbol{E} \times \boldsymbol{B}}{B^2} - \frac{1}{en_i}\frac{\nabla p_i \times \boldsymbol{B}}{B^2} \qquad (2.5)$$

The first term in the right hand side is the so called $\boldsymbol{E} \times \boldsymbol{B}$ velocity which represents the particle drift and the second term is the diamagnetic velocity which depends on the pressure.
The second order of derivation leads to the polarization velocity which is indeed smaller than the particle drift velocity.

2.2. Tokamak equilibrium

Equilibrium of magnetically confined plasma in tokamaks is a stationary situation, where all partial time derivatives are set to zero $\frac{\partial}{\partial t} = 0$. Furthermore, hot tokamak plasmas have low viscosity. They can therefore be neglected. Finally, assuming that the plasma is an incompressible fluid $\nabla\rho = 0$ leads to $\nabla . \boldsymbol{V} = 0$ due to the mass conservation equation. Those reductions lead to the ideal MHD equations. The ideal force balance equation expresses the balance between the kinetic pressure gradient and the Laplace force.

$$\boldsymbol{j} \times \boldsymbol{B} = \nabla p \qquad (2.6)$$

We can deduce from this equation that in plasma equilibrium (in absence of plasma rotation) the magnetic field lines and the current lines lie on the surfaces of constant pressure:

$$\boldsymbol{B} . \nabla p = 0 \qquad (2.7)$$

$$\boldsymbol{j} . \nabla p = 0 \qquad (2.8)$$

These surfaces of constant pressure are also surfaces of constant poloidal magnetic flux; they are called flux surfaces (Figure 2.12). The plasma parameters such as pressure and density are functions of the flux; they are constant on flux surfaces. The geometry of the flux surfaces can be calculated with the Grad-Shafranov equation.

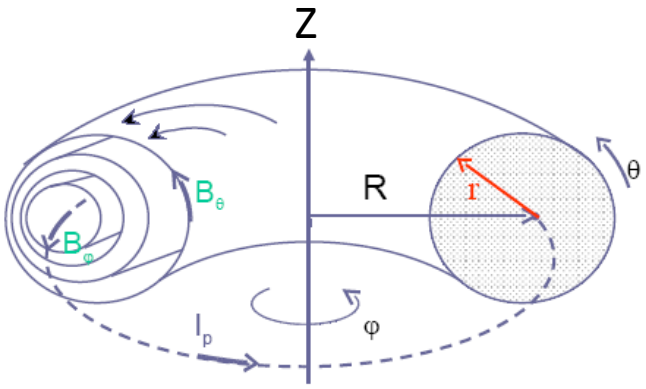

Figure 2.12. *Magnetic flux surfaces in a tokamak characterized by circular concentric geometry.*

2.2.1. Grad-Shafranov equation

The magnetic configuration in a tokamak is usually expressed as a flux function $\psi = \int_S B_\theta . dS$ which describes the poloidal flux going through a surface going from the magnetic axis outwards in the radial direction. The magnetic field can be rewritten in the right-handed cylindrical coordinate system (R, ϕ, Z) where ϕ is the angle of symmetry and R measures the distance to the axis of symmetry using the flux function:

$$B_R = -\frac{1}{R}\frac{\partial \psi}{\partial Z}, \; B_Z = \frac{1}{R}\frac{\partial \psi}{\partial R} \qquad (2.9)$$

It is obvious that $\vec{B}.\vec{\nabla}\psi = 0$, which means that the magnetic surfaces are surfaces of constant ψ.

Defining $F = RB_\phi$ and using Ampère's law: $\nabla \times \boldsymbol{B} = \mu_0 \boldsymbol{j}$, $\boldsymbol{j}$ can be rewritten as:

$$j_R = -\frac{1}{\mu_0 R}\frac{\partial F}{\partial Z}, \qquad j_Z = -\frac{1}{\mu_0 R}\frac{\partial F}{\partial R} \qquad (2.10)$$

Substituting these equations in equation 2.7 gives: $\nabla F \times \nabla p = 0$. Including the two previous equations in the force balance equation, we end with a partial differential equation describing the magnetic equilibrium in tokamak: the Grad-Shafranov equation.

$$R\,\frac{\partial}{\partial R}\left(\frac{1}{R}\,\frac{\partial \Psi}{\partial R}\right)+\frac{\partial^2 \Psi}{\partial Z^2} \;=\; -\,\mu_0 R^2\,\frac{\partial \mathrm{p}}{\partial \Psi} \;-\; F\,\frac{\partial \mathrm{F}}{\partial \Psi} \qquad (2.11)$$

This equation has three variables Ψ, F which are related to $\boldsymbol{B}$ and $\boldsymbol{j}$, and p. The topology of the equilibrium field is shown in Figure 2.12. It shows that the magnetic flux surfaces are nested.

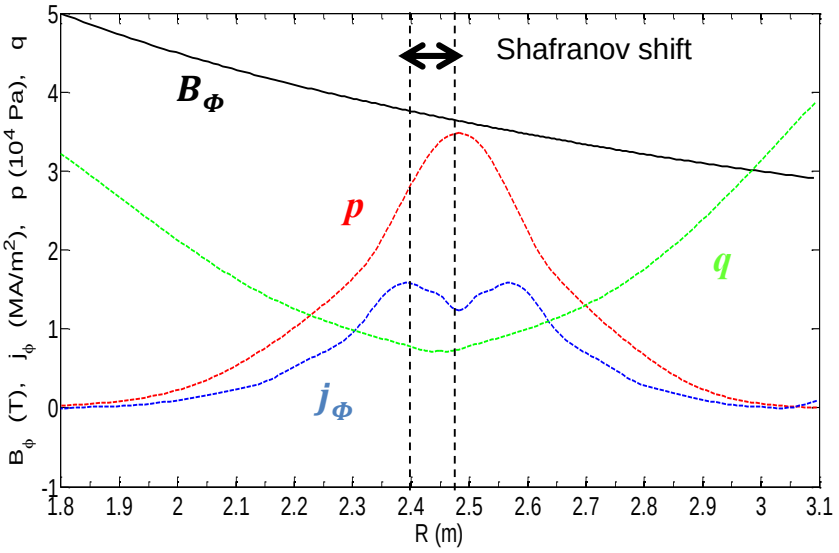

Figure 2.13. *Magnetic field, current density, pressure and q-profile for a standard Tore Supra discharge.*

The Figure 2.13 shows typical radial values for the toroidal magnetic field B_ϕ, the toroidal current density j_ϕ, the total kinetic pressure and the *q*-profile. The Shafranov shift is also displayed.

2.2.2. Effect of plasma rotation on the equilibrium

The Grad-Shafranov equation expresses the balance between the gradient of the pressure and the Lorentz force. The plasma rotation introduces a centrifugal force, which should be accounted for in the Grad-Shafranov equation as soon as it reaches the order of magnitude of the Lorentz force. The effect of rotation is to throw the plasma towards the outboard side of the flux surface. The centrifugal force should be considered to calculate a new equilibrium. To get a full description of the equilibrium, a single Grad-Shafranov equation doesn't suffice and second equation as a function of plasma rotation velocity is required. In most tokamaks the plasma velocity is subsonic (at low Mach numbers), so it is reasonable to neglect its influence on the equilibrium (J.W.S. Blokland et al., 2005).

2.2.3. Toroidal flux coordinate

The Grad-Shafranov equation is written in terms of derivatives with respect to ψ and is solved using this coordinate. However, it will appear that ψ is not a good coordinate for solving the transport and stability equations of the plasma quantities. We define here, the toroidal flux coordinate which is better for this purpose. Let us first introduce the toroidal flux Φ which is the flux of the toroidal field through the poloidal cross-section which is enclosed by the magnetic surface. Φ is constant on a magnetic surface and thus is a possible candidate for labelling it. Most often, the radial coordinate used is the toroidal flux coordinate:

$$\rho = \sqrt{\frac{\Phi}{\pi B_{\phi,0}}} \qquad (2.12)$$

2.2.4. Safety factor q

The safety factor *q* is so called because of the role it plays in determining the stability of the plasma. In general term, higher value of *q* leads to greater stability (J. Wesson, 1997). It also appears as an important factor in transport theory. Each magnetic field line is characterized by a value of *q*. The field lines are helical around the torus. If at some toroidal angle Φ, the field line has a certain position in the poloidal plane, it will return to that position in the poloidal plane after a change in toroidal angle $\Delta\Phi$. The *q*-value of this line is defined by:

$$q = \frac{\Delta\Phi}{2\pi} \qquad (2.13)$$

Rational values of *q* play an important role in stability. If $q = \frac{\mathrm{m}}{n}$ where *m* and *n* are integers, the field line joins up on itself after *m* toroidal and *n* poloidal rotations around the torus. From the previous equation and using the field line equation $\frac{\mathrm{R\,d}\phi}{ds} = \frac{B_\phi}{B_\theta}$ where ds stands for the curvilinear increment along the magnetic field line, and B_ϕ and B_θ are the toroidal and the poloidal magnetic field we obtain:

$$q = \frac{1}{2\pi}\oint \frac{1}{R}\frac{B_\phi}{B_\theta}\, ds \qquad (2.14)$$

where the integral is carried out over a poloidal circuit around the flux surface.
For the large aspect ratio tokamak the equation 2.14 can be approximated by:

$$q = \frac{r}{R_0}\frac{B_\phi}{B_\theta} \qquad (2.15)$$

2.2.5. Beta

The efficiency of confinement of the plasma pressure by the magnetic field is represented by the ratio:

$$\beta = \frac{p}{B^2/2\mu_0} \qquad (2.16)$$

2.3. Definition of the plasma rotation

From the collective motion plasma particles, a fluid velocity is derived and the single fluid velocity time evolution is described by the MHD equations. In this section, we will show the different parts of the fluid velocity and which part is the plasma rotation and which part represents the particle flux.

The total fluid velocity consists of toroidal V_ϕ and transverse components. The component in the poloidal plane splits in a part contained in the flux surfaces V_θ and a part perpendicular to the flux surface V_r. For circular ideal flux surfaces, θ and r are the polar coordinates in the poloidal plane. V_θ and V_r are called the poloidal and the radial components of the plasma velocity. The toroidal and the poloidal velocities set on a flux surface and constitute the plasma rotation. Sometimes, the plasma rotation is expressed by the angular frequencies: $\Omega_\phi = V_\phi/R$, $\Omega_\theta = V_\theta/r$.

From a physical point of view, the plasma rotation velocities are described by the parallel to the magnetic field component $V_\parallel$ and perpendicular to the magnetic field $V_\perp$. The different components of the plasma rotation are shown in Figure 2.14.

The behavior of the rotation velocity in the plasma is governed by the momentum balance equation. The perpendicular rotation velocity i.e. perpendicular to the magnetic field but not to the flux surface has a dependence on viscosity $(\nabla.\boldsymbol{\pi})_\perp$ and a direct driving term $\boldsymbol{j_r} \times \boldsymbol{B}$. In the parallel velocity, the only term in the right hand side of the equation (2.3 is $(\nabla.\boldsymbol{\pi})_\parallel$. The parallel velocity depends on viscosity and has no direct driving term in the absence of external sources. The viscosity influences the plasma rotation but doesn't drive rotation by itself. The parallel velocity is usually due to the redistribution of the perpendicular rotation by collisions and viscosity.

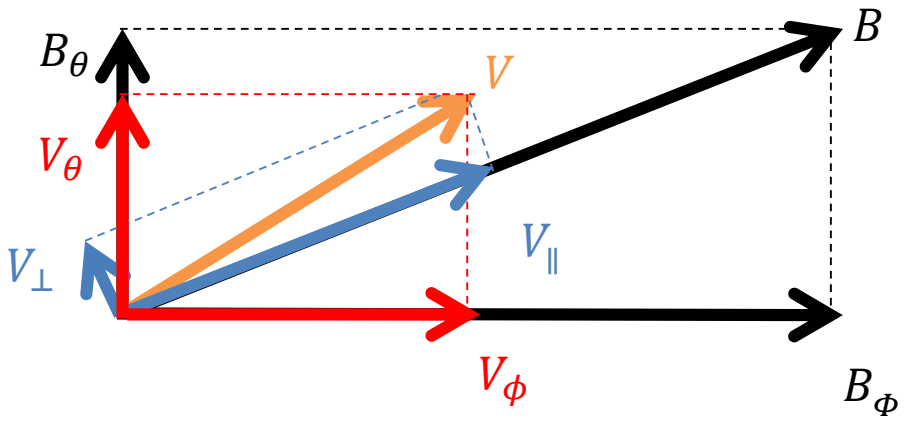

Figure 2.14. *Plasma rotation components. The toroidal and poloidal components are shown. The rotation can also be expressed in term of parallel and perpendicular to the magnetic field components.*

2.4. Momentum balance equation

The evolution and the behaviour of the plasma rotation are described by the momentum balance equation. In this section, we will focus on the definition of the different sources and momentum fluxes acting on the toroidal plasma rotation. Usually, the poloidal velocity is neglected, because it is strongly damped in a tokamak.

2.4.1. Momentum confinement time

The momentum confinement time τ_ϕ is the time in which the momentum is lost when the input torque is turned off. It is the characteristic time for momentum transport in the radial direction. The momentum diffusion coefficient $\chi_{v\phi}$ describes the momentum transport in the plasma. The momentum diffusion coefficient is related to the momentum confinement time by $\chi_{v\phi} = a^2/\tau_\phi$ where a is the plasma radius.

Considering the toroidal force balance:

$$\left(\frac{d\rho V_\phi}{dt}\right) = F_\phi \qquad (2.17)$$

Integrating over the whole plasma, it becomes:

$$d\left(\int_0^a mn\Omega_\phi R dr^3\right) = \left(\int_0^a \mathrm{F}_\phi R dr^3\right) dt \qquad (2.18)$$

$$\int_0^{L_\phi} dL'_\phi = T_\phi \int_0^{\tau_\phi} dt \qquad (2.19)$$

$$\tau_\phi = \frac{L_\phi}{T_\phi} \qquad (2.20)$$

where $L_\phi$is the total angular momentum of the plasma and T_ϕ is the total input torque (A. Kallenbach et al., 1991). The definition of the momentum confinement time is similar to the energy confinement time $\tau_E = \int \frac{3}{2} nTdx^3/P$, P being the total power input. Measurement of τ_E and τ_ϕ in several tokamaks show a linear relation between the two times. Increasing τ_E induces an increasing of τ_ϕ.

Many experiments carried out in different machines show that both in L-mode and H-mode regimes the energy confinement time τ_E reduces with increasing power input. Taking into account that the momentum confinement time $\tau_\phi$scales with the energy confinement time τ_E, we can state that the momentum confinement time τ_ϕ also reduces with increasing power input (deGrassie, et al., 2003). This dependence is taken into account when investigating plasma rotation in discharges with varied power input. Exceptions are also found considering the relation between τ_ϕ and τ_E (A. Kallenbach et al., 1991).

2.4.2. Momentum sources in the plasma

In the right hand side of the momentum balance equation, three forces that can drive plasma rotation: $\boldsymbol{j} \times \boldsymbol{B}$, $-\nabla p$, $-\nabla . \boldsymbol{\pi}$. The ∇p term is a force perpendicular to the flux surfaces and therefore has no contribution to the plasma rotation. The two other force terms have an influence on plasma rotation.

$\boldsymbol{j} \times \boldsymbol{B}$ is the Laplace force and acts in the perpendicular direction to the magnetic field. This force is applied in the plasma via two mechanisms: the first is by creating a radial current j_r and it will result in two forces $j_r\, B_\theta$ in the toroidal direction and $-j_r\, B_\varphi$ in the poloidal direction. This current includes the one created by the locally trapped particles in ripple wells. Indeed, these particles are lost to the walls of the device. Then, because of the ambipolarity condition, a return current is created. This term and its dependencies will be developed in chapter 4. The second mechanism arises from a perturbed magnetic field, which exhibits a radial component B_r. Again, this leads to two forces in the poloidal $j_\varphi\, B_r$ and toroidal $-j_\theta\, B_r$ directions.

The divergence of the anisotropic part of the pressure tensor $\boldsymbol{P}$ known as the viscous tensor $\boldsymbol{\pi}$ depends on collisions (friction) and velocity gradients. This implies that the plasma rotation in one region drives forces in other region of the plasma. From the viscous tensor and using the mass conservation equation, we can define the stress tensor $\boldsymbol{\Pi}$ as:

$$\boldsymbol{\Pi} = \boldsymbol{\pi} + mn\, \boldsymbol{V}\, \boldsymbol{V} \qquad (2.21)$$

The term $\nabla . \boldsymbol{\Pi}$ is a momentum flux and is responsible for momentum transport. In steady state and without external sources, it determines the shape of the rotation profile (P. Helander and D.J. Sigmar, 2002).

In the toroidal direction, the neoclassical part of the stress tensor leads to the neoclassical friction Π_φ^{neo} in presence of ripple (axisymmetry breaking, section 2.3), while the anomalous

(turbulent) part Π_{φ}^{ano} can be formulated in terms of diffusivity, convection and intrinsic source. It represents the Reynolds stress (F. L. Hinton and R.D. Hazeltine, 1976).

$$\Pi_{\varphi}^{neo} = -nmv_{neo}\left(V_{\varphi} - k_T V_T^*\right) \qquad (2.22)$$

$$\Pi_{\varphi}^{ano} = nm(-\chi_{v\varphi}\nabla_r V_{\varphi} + v_{\varphi}V_{\varphi} + \pi_{RS}) \qquad (2.23)$$

where k_T is a function related to the collisionality regime, $V_T^* = \frac{\nabla_r T_i}{eB_\theta}$ the toroidal diamagnetic velocity and v_{neo} is the damping rate. In the ripple plateau regime (observed regime in Tore Supra) an estimate of the damping rate is $v_{neo} = \sqrt{\frac{\pi}{2}} G_2(\alpha) N \delta^2 \frac{V_{Ti}}{R}$ and $k_T = 1.67$ (X. Garbet et al., 2010), where V_{Ti} is the ion thermal velocity. The function $G_2(\alpha)$ is the flux ripple average, which can be approximated by 1 (C. Fenzi et al., 2011). v_{φ} is the velocity pinch coefficient and π_{RS} is the residual or intrinsic stress. The diffusive term $\chi_{v\varphi}\nabla_r V_{\varphi}$ is roughly comparable to the ion thermal diffusivity. The residual stress is independent of the toroidal flow and constitutes a local momentum source which means that this source may drive a flux in the absence of initial toroidal velocity (nevertheless, wave momentum could be required for such as a local source). This velocity-independent stress π_{RS} is often related to the pressure gradient contribution to the radial electric field (O.D. Gurcan et al., 2007).
Also, external forces can add to the force balance equation such as momentum due to the NBI sources F_{NBI}, and the momentum S_{RF} transferred from RF waves to particles in heating schemes like LHCD scenarios. We will show that a non-negligible amount of momentum is transferred to the plasma during LHCD, in the core region where resonances occur. It is also worth mentioning the possible role of the turbulent acceleration as suggested in (X. Garbet et al., 2013), but it appears that this effect on plasma rotation is small.

As already mentioned above, the plasma consists of electrons and ions, and due to the mass ratio, the mass and the fluid velocity of the plasma are dominated by ions.

2.4.3 Momentum balance

In steady state situation and with the external force due to the RF waves, the force balance equation for ions becomes:

$$-e_i n_i(\boldsymbol{E} + \boldsymbol{V_i} \times \boldsymbol{B}) = -\nabla p_i - \nabla.\boldsymbol{\Pi_i} + \boldsymbol{R_i} + S_{RF} \qquad (2.24)$$

The collision operator $\boldsymbol{R_i}$ is often expressed as a friction term $\sum_{s'} n\, m\, v_{ss'} \left(V_s - V_{s'}\right)$ between the different plasma species: s. Assuming that the collisions are elastic and because of the action-reaction principle, the collisions do not generate any net toroidal momentum in the plasma.

The toroidal and radial projections of the momentum balance equation of ions 2.24 give:

$$n_i m_i \nabla.\left(-\chi_{i,v\varphi}\nabla_r V_{i,\varphi} + v_{i,\varphi}V_{i,\varphi} + \pi_{RS}\right) = e_i n E_\varphi + j_r \times B_\theta - n_i m_i \nu_{neo}\left(V_{i,\varphi} - V_T^*\right) - S_{RF,\varphi} \quad (2.25)$$

$$E_r - V_{i,\phi}B_\theta + V_{i,\theta}B_\phi = \frac{\nabla p_i}{e_i n_i} \quad (2.26)$$

where E_r is the radial electric field. The stress tensor is replaced by its components. Most of the neoclassical results can be derived from this set of two equations.

The ambipolarity

The neoclassical radial fluxes are independent of the radial electric field (in the absence of orbit squeezing and ripple) and they are ambipolar $\Gamma_{re} = \Gamma_{ri}$. This result comes out assuming the electro-neutrality condition $\sum_s n_s e_s = 0$.

Consequently, the neoclassical theory doesn't make any prediction for the magnitude of the radial electric field. Indeed, the ambipolarity excludes any charge separation. Breaking the axisymmetry assumption (presence of ripple per example) allows us to surmount this indetermination.

2.5. Neoclassical transport and rotation

There are several channels leading to the transport of momentum, energy and particles in the plasma: classical, neoclassical and turbulent. The classical model describes the transport caused by collisions in cylindrical plasma. When we take the torus shape into account, we find that the collision driven transport is higher than in the classical case. The collision driven transport in a torus geometry confined plasma is identified by the neoclassical transport. Additional to the collisions, also turbulence can drive transport. The neoclassical model which gives us the lower limit of particle, energy and momentum transport is the transport in absence of turbulence.

From the neoclassical theory, it is found that the poloidal velocity is strongly damped due to the parallel viscosity. The effect of the poloidal flows on the poloidal rotation is small and very localized. Another result from the neoclassical theory is the existence of a spontaneous or intrinsic rotation. This spontaneous rotation develops in absence of any applied external torque and has an impact on the confinement and stability of the plasma. In this chapter, the neoclassical transport is discussed and the neoclassical expression of the intrinsic rotation will be given.

2.5.1. Neoclassical theory

Classical transport is solely governed by collisions. This theory was developed independently by several authors, but the most well-known and pedagogic formulation is due to Braginskii (S.I. Braginskii, 1965). It considers the plasma with a single ion and electron species and assumes a large-flow ordering $\frac{E_r}{B} \sim V_{Ti}$. It is remarkable that the complete theory for the small-flow case was worked out only half century after Braginskii's original work (P.J. Catto and A.N.Simakov, 2004).
Classical transport is a diffusion process (random walk) with $D_s \propto \rho_{L,s}^2/\tau_{c,s}$ the diffusion coefficient for particle s. $\tau_{c,s}$ is the collision time and $\rho_{L,s}$ is the Larmor radius. The classical transport is only valid when the magnetic field is homogeneous and stationary.
Due to the toroidal shape of the tokamak, the magnetic field is stronger in the inner side of the torus. The curvature and the gradient of the field lead to additional forces and flows which are not present in the cylindrical configuration. The classical model cannot therefore describe the particle, energy and momentum transport. The neoclassical theory takes into account this inhomogeneous field, which results in the correct description of the collisional transport in a tokamak.

The charged particles traveling from the outer side of the torus to the inner side go from a region with lower magnetic field to a region with higher magnetic field. The particles see a ∇B and experience a force $F = -\mu \nabla_{\parallel} B$ where $\mu = m V_{\perp}^2/2B$ is the magnetic moment which is a constant of motion. This force will slow down the parallel velocity of the particles when they are moving towards the high-field side of the tokamak. Particles with low enough $V_{\parallel}$ will be stopped and reflected before reaching the high field side.

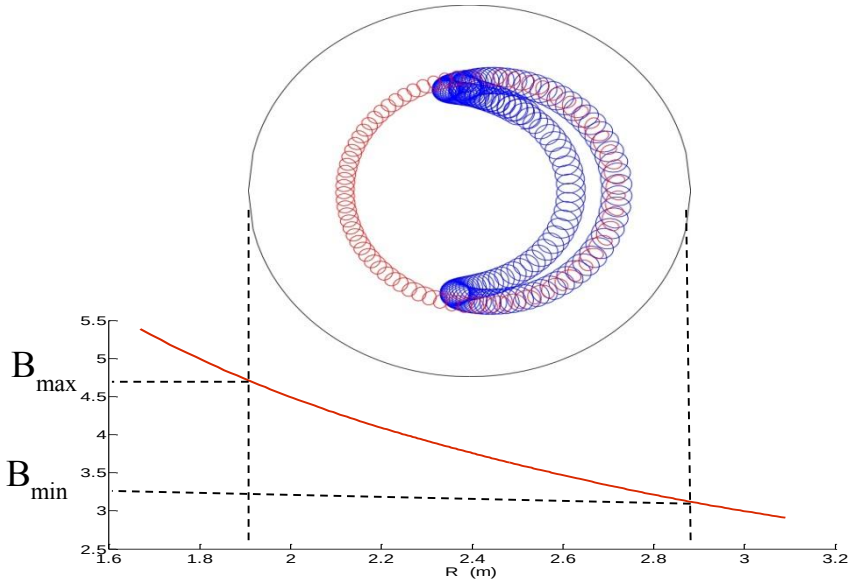

Figure 2.15. *Poloidal projection of the passing (with small pitch angle $V_{\perp}/V_{\parallel} \ll 1$) and trapped particle orbits. Due to the drift the orbits do not follow the magnetic flux surfaces, but are slightly shifted.*

They oscillate in banana orbits and they are called trapped particles (Figure 2.15). Particles that are fast enough will not bounce back and continue their trajectory parallel to the field line; they are called passing particles. Due to the drifts, the passing and trapped particles are shifted with respect to the magnetic field lines. For trapped particles, this means that they have a certain width δ_b. Characteristics of the trapped particles are given bellow:

- The width of the banana orbit $\delta_b \approx 2q\epsilon^{-1/2}\rho_L$
- The fraction of trapped particles $f_t \approx \sqrt{2\epsilon}$
- The bounce frequency $\omega_b \approx V_{th}\sqrt{\epsilon}/qR$

The existence of banana orbits has a significant influence on the collisional transport. For example, if the bounce frequency is lower than the collision frequency, the trapped particle will collide with other particles before completing its banana orbits, it doesn't know it is trapped and the transport is therefore close to classical.

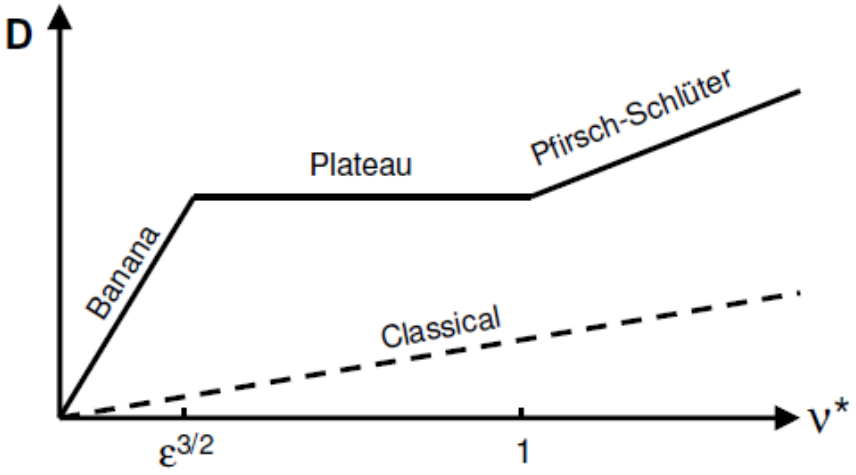

Figure 2.16. *The variation of the diffusion coefficient with the collisionality through the three neoclassical transport regimes. The classical diffusion coefficient is also displayed. The neoclassical theory predicts a larger transport than the classical theory.*

When the collision frequency is lower than the bounce frequency, the trapped particles can at least complete one banana orbit without colliding. In a tokamak, three different transport regimes are defined: the low collisionality banana regime, the high collisionality Pfirsch-Schlüter regime and the intermediate regime. In Figure 2.16, the diffusion coefficient is drawn as a function of the collisionality. The three neoclassical transport regimes are easily discriminated.
The poloidal momentum of the trapped particles is null, because they never make a complete poloidal turn.

2.5.2. The poloidal damping

The toroidal shape of a tokamak is the reason for the inhomogeneity of the magnetic field, stronger inside of the torus and weaker outside. The poloidally rotating plasma does see the varying field when moving from the outside to the inside of the torus. Through the magnetic pumping, the poloidal rotation decays, because the kinetic energy of the poloidal rotation is used to heat the plasma (J.M. Berger et al., 1958; T. H. Stix, 1973).

When the particle moves to the high field side, the particle will gain perpendicular energy $m V_{\perp}^2/2$. Due to the energy conservation, the parallel velocity will decrease. When returning to the low field side, the particle will lose the perpendicular gained energy, and the net change over one period is zero. Also, the net change in the parallel velocity is null. However, when the collision occurs in the high field side, the particle will redistribute its extra energy, and heat the plasma. After the collision, the magnetic moment μ is lower than before the collision and the parallel velocity will reduce over one period (J.M. Berger et al., 1958).
When the collision time is larger than the perturbation period, the poloidal rotation is damped. This is due to the trapped particles. Those particles for which the parallel velocity $\mathrm{V}_{\|}$ gets zero before reaching the high field side. Therefore, they do not contribute to the poloidal momentum. This poloidal damping is usually called transit-time magnetic pumping. Collisions between trapped and passing particles will reduce the poloidal flow (the collisional part of the poloidal flow damping).
The toroidal momentum of trapped particles is different from zero because the banana orbits of the trapped particles have a toroidal precession around the torus.

2.6. Spontaneous neoclassical rotation

In the case where no external momentum is provided (e.g. by neutral beams), plasma rotation is still possibly due to the density gradients, temperature gradients and local radial electric field. The parallel electric $\mathrm{E}_{\|}$ field which exerts a parallel force $F = eE_{\|}$ on ions is also a possible source of toroidal momentum. However, due to the higher mass of ions compared with electrons, $E_{\|}$ will predominantly accelerate the electrons, giving rise to the current rather than rotation. Nevertheless, the momentum due to $E_{\|}$ is not negligible.

From the conservation equations of ions, the ohmic spontaneous rotation is derived. In order to get a clear picture of the different mechanisms at play, we will consider the mass and momentum conservation equations for the ion fluid and in steady state, no momentum exchange with other species and isotropic conditions (F. F. Chen, 1993).

$$n_i \nabla . \boldsymbol{V_i} = 0 \qquad (2.27)$$

$$e_i n_i (\boldsymbol{E} + \boldsymbol{V_i} \times \boldsymbol{B}) = \nabla p_i \qquad (2.28)$$

The cross product of the equation eq. 2.28 with $\boldsymbol{B}$ leads to the perpendicular velocity of ions: $\boldsymbol{V}_{i,\perp} = \frac{\boldsymbol{E}\times\boldsymbol{B}}{B^2} - \frac{1}{e_i n_i}\frac{\nabla p_i \times \boldsymbol{B}}{B^2}$. It is the drift velocity due to the forces $e\boldsymbol{E}$ and $-\nabla p_i$. The second term of the equation is the diamagnetic velocity and it is hidden in the diamagnetic current:

$$en_i\boldsymbol{V}_{i,\perp} - en_e\boldsymbol{V}_{e,\perp} = \frac{\nabla p_i \times \boldsymbol{B}}{B^2} - \frac{\nabla p_e \times \boldsymbol{B}}{B^2} \qquad (2.29)$$

$$\boldsymbol{j}_\perp = -\frac{\nabla p \times \boldsymbol{B}}{B^2} \qquad (2.30)$$

The above derivation indicates that the electric field and the pressure gradient can induce both poloidal and toroidal rotation. Neoclassical theory in presence of ripple (H. A. Claassen et al., 2000; X. Garbet et al., 2010) is used to derive the natural neoclassical poloidal rotation V_θ^{neo} and the derivative of the neoclassical toroidal velocity V_ϕ^{neo}:

$$V_\theta^{neo} = \frac{k_1}{eB_\phi}\frac{\partial T_i}{\partial r} \qquad (2.31)$$

$$V_\phi^{neo} \approx \frac{k_2}{eB_\theta}\frac{\partial T_i}{\partial r} \qquad (2.32)$$

where k_1 and k_2 are constants and depend on the collisionality. The values of k_1, k_2 in different collisionality regimes, are reported in the Table 2.1 (C. Fenzi et al., 2011).

Regime	**Banana**	**Plateau**
Coll.	$\nu^* \ll \frac{1}{N^2q^2}$	$1/N^2q^2 \ll \nu^* \ll Nq\frac{\delta^2}{\varepsilon^2}$
$\boldsymbol{k_1}$	1.17	1.17
$\boldsymbol{k_2}$	3.54	1.67

Table 2.1. *Neoclassical regimes for various collisionality limits (see* (X. Garbet et al., 2010; R. D. Hazeltine, 1974; H. A. Claassen et al., 2000) *for more details).*

The neoclassical toroidal rotation depends on the radial electric field (Y.B. Kim et al., 1991) and can be considered as a result of momentum transport from spontaneous rotation in other positions in the plasma.

The rotation can improve the confinement and the stability of the plasma; this is why spontaneous rotation has a beneficial role. From above, we know that the spontaneous rotation is expected in tokamaks. However, the values of the spontaneous rotation predicted by the neoclassical theory can differ depending on the assumptions made. Moreover, the models used to derive the above expressions are far from complete; the friction forces of the trapped particles on passing particles were for example not included. Also turbulent transport was not taken into account. Due to the complexity of the topic, there exists a wide range of models that yield a large range of spontaneous rotation predictions.

2.6.1. Impurity and MHD rotation

The rigorous physical picture of the plasma is that it consists of many different species, and each has a fluid like behavior (depending on the time scales). When the plasma is diagnosed, the properties of one of the plasma species is measured, instead of the properties of the single plasma fluid. It is therefore important to know the relationship between the plasma velocity $\boldsymbol{V}$ used in the MHD equations, and the fluid velocity of the main ions $\boldsymbol{V_i}$, electrons $\boldsymbol{V_e}$ and impurities $\boldsymbol{V_I}$.
The fluid velocity in the center of mass velocity of all fluids reads:

$$\boldsymbol{V} = \frac{\boldsymbol{V_i} n_i m_i + \boldsymbol{V_e} n_e m_e + \sum_l \boldsymbol{V_I}\, n_I m_I}{n_i m_i + n_e m_e + \sum_l n_I\, m_I} \qquad (2.33)$$

Assuming that the impurity density is low $n_I m_I \ll n_i m_i$ and taking into account the mass ratio between ions and electrons $\frac{m_e}{m_i} \ll 1$, the plasma fluid velocity can be approximated by the main ion velocity $\boldsymbol{V} \approx \boldsymbol{V_i}$.

Measurements of plasma rotation are principally done with spectroscopy based on the emission of the impurities. This means that $\boldsymbol{V_I}$ is measured. Other diagnostics like ECE or reflectometry measure the fluctuations of the electron temperature or density. these fluctuations are usually related to the electron fluid velocity. In this section, we will discuss how the measured impurity velocity can be translated into the plasma velocity.

Impurity rotation
Usually, it is assumed that the temperatures of the impurities and the main ions are equal because the collision frequency is high enough. However, the fluid velocity of the main ions is not necessary the same as the impurities. A differential rotation is observed when there is a difference in the pressure gradient $\frac{\nabla p}{Z_I}$, Z_I being the charge number of the impurities. This occurs typically in a situation with continuous momentum input like neutral beams. It is also found that a significant differential rotation between these two ion species exists in the regions where the second radial derivative of the ion temperature is large (D. Testa et al., 2002).
The neoclassical moment approach of Hirshman and Sigmar (Y.B. Kim et al., 1991; S. P. Hirshman and D. J. Sigmar, 1981) provides an expression for the differential rotation between the main ions and impurities. The difference in rotation $\Delta V = V_i - V_I$ is given by (S. P. Hirshman and D. J. Sigmar, 1981; D. Testa et al., 2002):

$$\Delta V_\theta^{neo} \approx \frac{1}{2eB_\phi} \frac{\partial T_i}{\partial r} \left[-3k_3 + 2\frac{L_T}{L_{p,i}} \left(1 - \frac{Z_i L_{p,i}}{Z_I L_{p,I}} \right) \right] \qquad (2.34)$$

$$\Delta V_\phi^{neo} \approx -\, k_3 \frac{1}{eB_\theta} \frac{\partial T_i}{\partial r} \qquad (2.35)$$

where the θ-dependence is neglected. L_T is the temperature gradient length and $L_{p,i}$, $L_{p,I}$ are the pressure gradient lengths of the main ions and impurities, respectively. k_3 is a function depending on the collisionality.

The difference in the poloidal rotation depends on the impurity pressure gradient and main ion pressure, while the difference in the toroidal rotation depends on the temperature gradient only. The difference in toroidal rotation becomes significant when the temperature profile is peaked ($\frac{dT}{dr}$) and when the plasma current is low ($\frac{1}{B_\theta}$). The validity of the above equations has been tested on several machines (D. Testa et al., 2002; L.R. Baylor et al., 2004). It was also found that a strong pressure gradient doesn't induce a significant change in toroidal rotation (B. A. Grierson et al., 2012).
In Tore Supra, the analysis of the difference in toroidal rotation between the heavy impurity ions and the main ions shows that this difference is small (<12%) and takes the following form (A. Romannikov et al., 2000):

$$\frac{\Delta V_\phi^{neo}}{V_{i,\phi}} \approx \frac{1.5\, k_\Delta}{k_2} \qquad (2.36)$$

with $k_\Delta \approx 0.3$ in the core plasma for standard plasma parameters (Y.B. Kim et al., 1991). The conclusion here is that in Tore Supra, main heavy impurity ions and main ions move in the counter-current direction with approximately the same velocity.

MHD rotation

The current in the plasma represents the difference between the electron and ion velocities $\boldsymbol{j} = -ne(V_e - V_i)$, when the plasma impurities are neglected. If we measure the current density and the electron fluid velocity, then, one can get the ion fluid velocity. The main part of the current is parallel to the magnetic field, but there is also a component perpendicular to the magnetic field (diamagnetic current).

It is difficult to directly measure the electron fluid velocity, although it can be done with the tangential Thomson scattering (F. A. Karelse et al., 2001). Diagnostics like ECE or reflectometry measure the fluctuations of the electron temperature or density. The frequency of these fluctuations can be translated into plasma rotation. These fluctuations occur when the MHD modes are present in the plasma and under certain conditions, flux surfaces can break up and reconnect, thus changing the magnetic topology. The relation between the electron diamagnetic drift, MHD frequency f_{MHD} of the modes and the plasma velocity allows us to deduce the plasma rotation from the measured MHD frequency.

$$f_{MHD} = n\frac{V_\phi}{2\pi R_0} + f_e \qquad (2.37)$$

where f_e is the diamagnetic frequency referring to the magnetic island present in the plasma (F. C. Schuller, 1991).

2.7. Turbulent or anomalous transport

The neoclassical transport is responsible for 10% of ion transport and for about 1% of the electron transport, in most cases. The confinement time of the plasma is ten times longer with the neoclassical approach than the experimental measurements. The particle, energy and momentum transport is still not fully described, and we usually speak about the anomalous transport. This transport is generated by the micro-instabilities induced by the temperature and density gradients. Due to the magnetic pressure and the external heating, the plasma is thermodynamically out of equilibrium. In order to transport the applied power, the plasma will generate micro-instabilities through non-linear mechanisms like turbulent convection. The collisional processes are not really efficient to transport the energy and the MHD instabilities have a tendency to destroy the magnetic configuration. On the other side, the turbulent micro-instabilities can transport the energy over long distances and in short times, thus decreasing the plasma confinement time. In the following section, we will discuss the main micro-instabilities, in particular the ITG modes and TEMs.

2.7.1. Micro-instabilities

The micro-instabilities are due to the microscopic structure of the plasma. The existence of the gradients in the plasma makes the plasma response to the perturbation non-adiabatic. Because the magnetic field is non-uniform, the electric field non-null and the temperature and the density gradients are strong (the temperature goes from few eV at the edge to few keV in the core) the plasma will have a non-adiabatic response to the electromagnetic perturbations. The plasma will therefore propagate the growing instabilities. The drift waves (Figure 2.17) are the archetype of the instabilities in the magnetized plasma, like ITG modes and TEMs.

In a magnetised plasma, one has to account for the electric fluctuations $\delta E/E$ and magnetic fluctuations $\delta B/B$. Since the factor β is small, the magnetic fluctuations are negligible. Then, only the fluctuations in the electric potential are considered and transport is realised through the fluctuations of the drift velocity $E \times B$. Moreover, the $E \times B$ velocity is capable of stabilising the plasma and improving the confinement. Many other drift mechanisms exist as the drifts due to the gradient of the magnetic field and the curvature of the field lines (R.J. Rutherford and P.H. Goldston, 1995).

ITG modes and TEMs

The ion temperature gradient (ITG) modes concern the passing and trapped ions. Their frequencies are associated to the temperature and density gradients in the plasma. The particles become adiabatic to the instability when the wavelength of the modes is smaller than the characteristic length of the particles or when the velocity of the particles is high enough to be insensible to the perturbation.

The ITG modes are destabilised in the presence of ion temperature gradients. These instabilities are particularly prominent when the ion heating is dominant and their growth rate γ_{ITG} is:

$$\gamma_{ITG} \propto \frac{C_s}{\sqrt{L_{Ti}R}} \qquad (2.38)$$

where $C_s = \sqrt{T_e/m_i}$ is the sound velocity and L_{Ti} the ion temperature gradient length.

The ITG modes have two branches:

- The slab branch: it is an unstable mode due to the compression effects along the field lines. This mode persists in the cylindrical geometry.
- The toroidal branch: specific to the toroidal geometry of a tokamak. It is due to the magnetic field curvature effects.

For the instability threshold of the toroidal ion mode, there is a critical gradient $(R/L_{Ti})_{crit}$ beyond which the mode becomes unstable for small density gradients R/L_{ne}. However, at high R/L_{ne}, the instability threshold increases with the parameter L_{ne}/L_{Ti}.

Due to the radial variation of the magnetic field, the toroidal symmetry is broken and mode coupling occurs in the plasma. The mode coupling induces structures radially extended over the correlation length. The correlation length for the ITG modes is $\rho_{mixte}(qR/L_T)$, with $\rho_{mixte} = \sqrt{m_i T_i}/eB$ the Larmor radius. The modes become global for the plasma stability. The radial transport becomes more important and occurs over longer lengths.

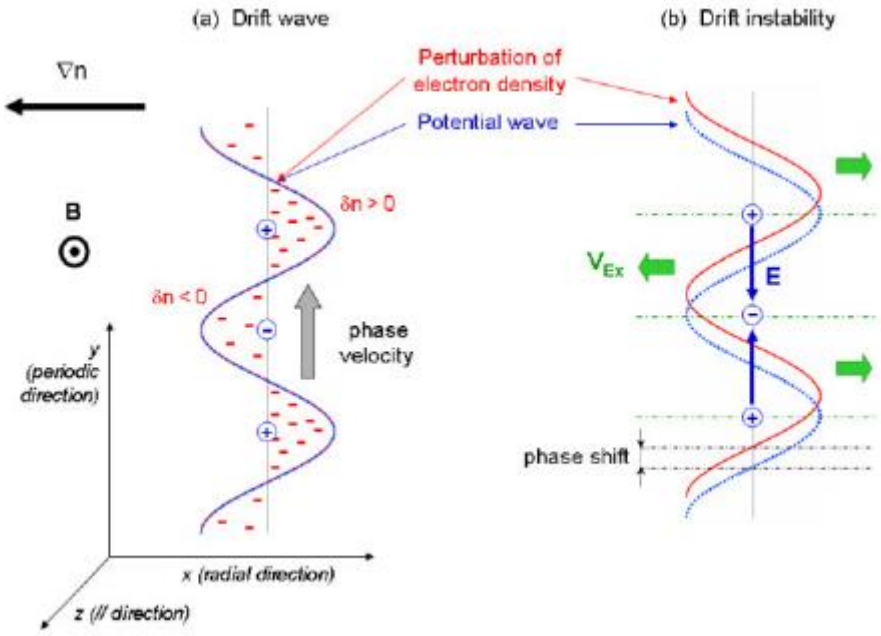

Figure 2.17. *Drift wave propagation due to the density perturbation and the drift wave instability.*

The trapped electron modes (TEMs) are electrostatic modes due to the trapped electrons. Their free energy is due to the electron temperature and density gradients. Two types of trapped electron modes can be distinguished: the dissipative (due to the collisions) and the

collisionless trapped electron modes. They don't have a precise wavelength limit since they overlap with the ITG.

Other turbulent structures are also observed in numerical simulation and experiments like the zonal flows (Z. Lin et al., 1999), electromagnetic modes and streamers (P.H. Diamond et al., 1995).

$E \times B$ shear stabilisation

Turbulence stabilisation permits reaching the high confinement regimes of the plasma. There are principally three stabilizing effects: the density peaking, the magnetic shear and the poloidal velocity shear. In this paragraph we will focus on the $\boldsymbol{E} \times \boldsymbol{B}$ shear.

The $\boldsymbol{E} \times \boldsymbol{B}$ shear is efficient to decrease the turbulent transport coefficient. It acts on the growth rate and the width of the mode. In the plasma, there are turbulent vortices, which can be considered as a superposition of convective cells extending over the characteristic correlation lengths. The velocity shear stretches these cells to the breaking point beyond which they lose their coherence.

It is shown that the stabilisation needs a shear of the component dependent on the radial electric field E_r in the rotation frequency, in other words E_r/RB_θ (R.E. Waltz et al., 1994). The shear of this rotation frequency affects the stability of the plasma. In toroidal geometry the velocity shear due to the radial electric field and adapted to the interchange turbulence which the most common in the tokamak reads (T.S. Hahm et K.H. Burrell, 1995):

$$\gamma_{E\times B} = \frac{RB_\theta}{B}\frac{\partial}{\partial r}\left(\frac{E_r}{RB_\theta}\right) \qquad (2.39)$$

The impact of the velocity shear on the plasma confinement is considered as the principal cause of the H-mode. The stabilisation process can be simply seen as follow: when the pressure gradient increases, the radial electric field augments and induces a drift wave stabilisation. This leads to a more pronounced increase of the pressure gradient which allows generating and maintaining the transport barrier.

2.8 Ripple and stochastic diffusion

The discrete structure of the magnetic system of a tokamak, which is made up of *N* separate coils, destroys the axial symmetry of the system and leads to enhanced radial transport. The periodic modulation of the magnetic field is then identified as the magnetic ripple (Figure 2.18). The study of ripple losses is mainly of interest in connection with the design of tokamaks and with reactor parameters. The ripple transport depends strongly on the depth of the ripple, which in its turn is determined by the design and the number of toroidal field coils. The toroidal field coils are a major and extremely expensive part of the thermonuclear systems. An analysis of ripple transport could help to decrease the cost depending on the adequate physics.

The ripple transport that augments the neoclassical transport is produced primarily by two groups of particles: locally trapped particles which are captured in the minimum *B* between

two toroidal field coils (Figure 2.18), and the banana particles due to the radial variation of the magnetic and which are trapped in the outboard side of the torus. For relatively large ripple, the losses owing to locally trapped particles dominate.

The effect of ripple on the orbit of the banana particles reduces to radial displacement at each transit of the bounce point (banana tips). The trapped particles in ripple wells experience a variety of transport regimes and then are lost to the wall.
The complete analysis of ripple in tokamaks can be found in (P.N. Yushmanov; P.N. Yushmanov, 1990; R.J. Rutherford and P.H. Goldston, 1995).

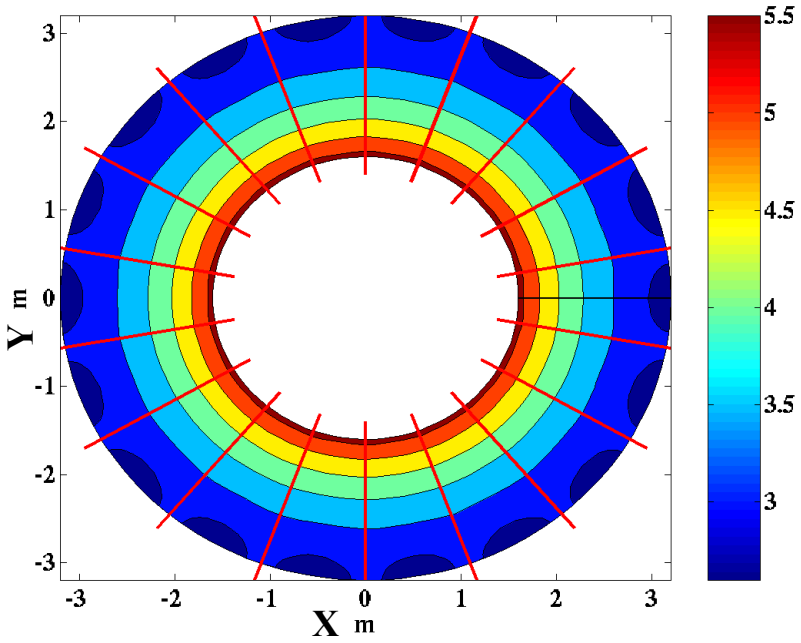

Figure 2.18. *Top view of the Tore Supra Tokamak. The red lines represent the toroidal field coils. The magnitude of the magnetic field is represented by colour code. One can see the radial decreasing of the magnetic field.*

2.8.1. Toroidal magnetic field in tokamaks

In a narrow sense, ripple refers to the inhomogeneity of the magnetic field caused by the discreteness of the magnetic system. In term of similarity of the resulting physical processes, however, ripple can include all the weak perturbations in the axial symmetry of the toroidal magnetic field, independently of their causes, e.g error fields.

Two mechanisms are responsible for locally trapped particles in magnetic mirrors:

- Direct trapping due to the collisions which induce angular diffusion of the velocity vector. The pitch angle is modified when the particles fly-over the magnetic ripple wells.

- Non-collisional trapping due to drift velocity. The particle that experiences the gradient of the magnetic field modulation will be trapped during the bounce above the magnetic mirror.

In order to understand the ripple trapping, one should describe the magnetic field. In the toroidal coordinate system r, θ, φ given by:

$$R = R_0 + r\ cos\ \theta = R_0\ (1 + \varepsilon \cos\theta), \quad Z = r \sin\theta \tag{2.40}$$

where $\varepsilon = r/R_0$ is the inverse aspect ratio of the torus. The toroidal magnetic field of an ideal axisymmetric tokamak decreases as $1/R$.

$$B \approx B_0\ R_0/R \tag{2.41}$$

with B_0 the main toroidal magnetic field. Here we assume that the magnetic surfaces are circular.

We shall define the ripple depth as the amplitude of the perturbation in the toroidal magnetic field:

$$\delta(r, \theta) = \frac{B_{max} - B_{min}}{B_{max} + B_{min}} \tag{2.42}$$

where B_{max} is the maximum (under the TF coil) and B_{min} the minimum (between two coils) values of the magnetic field taken at constant r and θ. The perturbation amplitude alone is not sufficient to analyse the physical processes due to the ripple. The shape of the wells is also important. The perturbation can be represented as a sum of sinusoidal harmonics. In most cases, only one harmonic is important inside the vessel. We have to describe the overall amplitude of the perturbation δ for this harmonic. Then the toroidal magnetic field of a tokamak has the form:

$$B_\varphi = (1 + \delta \cos(N\varphi))\ B_0\ R_0/R \tag{2.43}$$

The field perturbation is now characterized by the amplitude δ and the harmonic *N* which represents the number of the toroidal field coils (because the symmetry breaking is due to the discreteness of the magnetic system).

During the particle motion (non-collisional), the magnetic moment μ and the energy w are conserved. These two invariant are linked by:

$$\frac{w}{\mu} = \left(1 + \left(\frac{V_\parallel}{V_\perp}\right)^2\right) B \tag{2.44}$$

2.8.2. Non-collisional trapping

This mechanism concerns mostly the fast particles (ions or electrons). The collisional braking doesn't affect the particles and keep the pitch angle $\frac{V_{\parallel}}{V_{\perp}}$ unchanged. The drift velocity induces a displacement of the local maxima of magnetic field which modifies the depth of the magnetic wells. If the particle explores during its bounce a local maximum B_{max} stronger than $\frac{w}{\mu}$, the particle will be trapped.

$$B_{max} > \frac{w}{\mu} \qquad (2.45)$$

In other words, the drift velocity drives the particles away from the equatorial plane (the direction depends on the nature of the particle). The particles are therefore driven outwardly where the magnetic field modulation is stronger and then can be trapped (Figure 2.19).

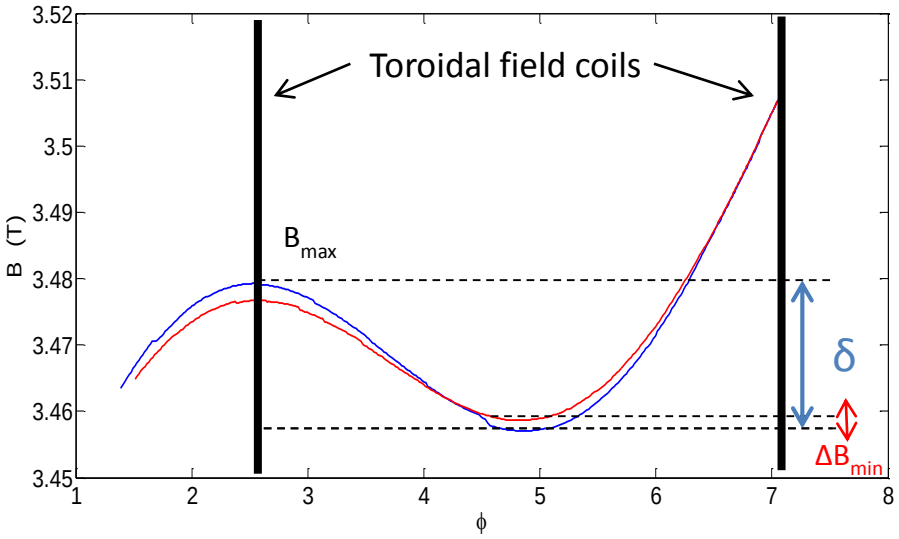

Figure 2.19. *Non-collisional trapping mechanism. The magnetic moment and the energy conservations fix the bounce point of the particle. The particle will be trapped when it experiences a stronger magnetic field.*

2.8.3. Collisional trapping

This mechanism concerns the thermal particles. The collisions induce a dispersion of the pitch angle. The collisions during the particles fly-over of the ripple wells can trap them but also can de-trap the trapped particles. The probability of de-trapping due to the collisions decreases with the particle energy. The collisional trapping can be summarised as a de-correlation of the toroidal position of the particle bounce points due to the collisions.

In Tore Supra, the trapped fast particles undergo the vertical drift to the top side of the machine for electrons and to the bottom side for ions. The fast particles leave the plasma very quickly.

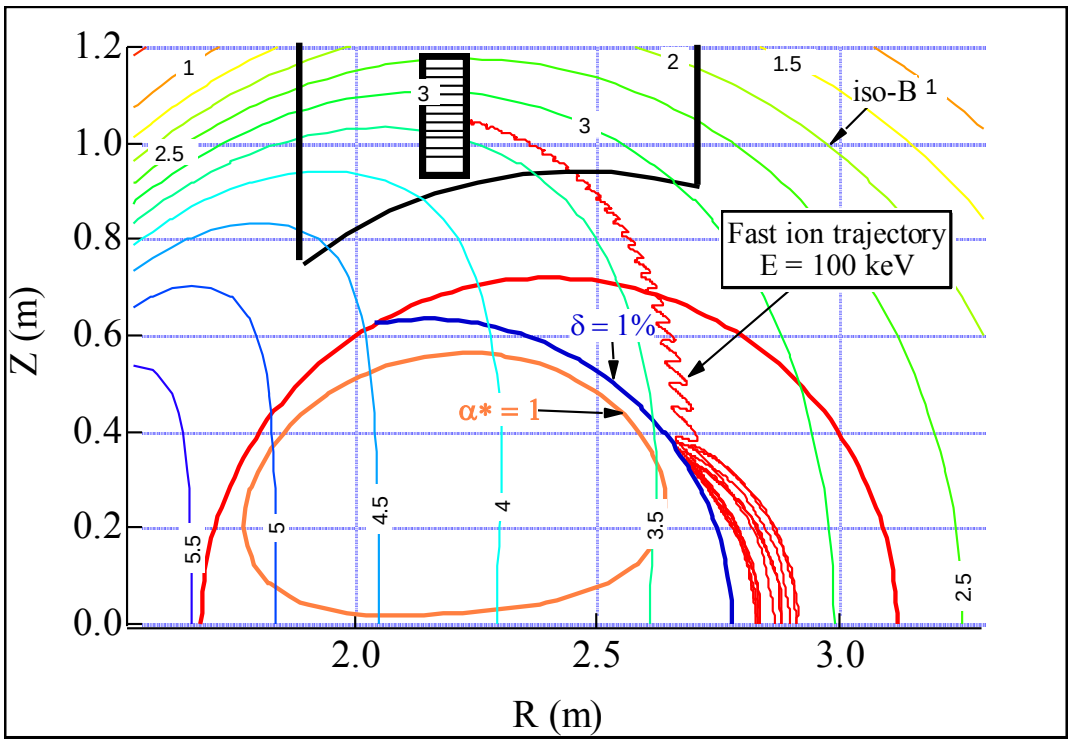

Figure 2.20. *Poloidal cross section of 100 keV fast particle trajectory. The vertical lines represents the iso-B, and also the iso-ripple line of 1% is also represented. The figure shows also the good confinement zone where any trapping occurs. The black curves represent a window where ripple diagnostic is installed.*

The Figure 2.20 represents a poloidal cross section showing the fast particle trajectory and the iso-ripple line of 1%. The good confinement zone where the ripple has no influence and any trapping occurs is also illustrated. At the top of the figure, the diagnostic DRIPPLE used to detect the locally trapped particles is indicated.

2.8.4. Stochastic diffusion

Stochastic diffusion as illustrated in Figure 2.21 is a transport process that occurs in the good confinement region where there are any ripple wells. Ripple de-correlates the position of the banana tips between two successive rebounds. This mechanism induces a random walk of the banana tips, and therefore engenders a stochastic diffusion (R.J. Goldston et al., 1981). If the toroidal angle between two rebounds is higher than the angle between two coils, the radial motion of the particle becomes stochastic. The stochastic diffusion depends on the energy of the particles. This mechanism becomes dominant at high energy inducing flux particles on different structures in the equatorial plane like antennas (A. Ekedahl et al., 2007).

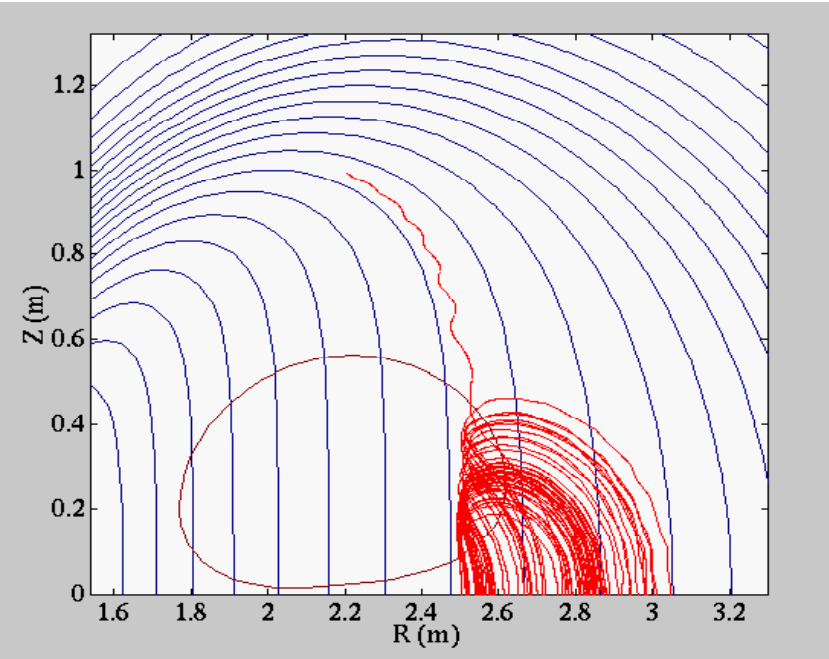

Figure 2.21. *Transport process induced by the stochastic diffusion in the direction of the iso-B. The banana tips are transported to the local trapping region. In some cases, the banana width can exit the particle from the plasma through the first orbit.*

2.8.5. Ripple diagnostic in Tore Supra

Tore Supra is a well suited machine for ripple studies, because it presents a ripple magnitude of 5% at the plasma edge. To achieve this analysis, two diagnostics are installed in Tore Supra (V. Basiuk et al., 1992). One is installed at the top of the torus, which allows the investigation of the fast electron drift, and the second being installed on the bottom of the torus for the fast ion drift. Both are designed to measure the particle current flow I_{lost} lost along iso-*B* lines at different vertical positions, each diagnostic consisting of twelve graphite collectors. Owing to the fact that the electron drift trajectories follow the iso-*B* lines, the radial profile of the density of the fast electrons and ions which are trapped and then lost in the local magnetic well can be deduced.

In our study, for fast electron ripple losses, the ripple measurements of the recent campaigns (2008-2011) are analysed, while, for fast ion losses, discharges before 1999 (before the CIEL configuration) are analysed (M. Lipa et al., 1997). After the CIEL configuration, the ions drift to the bottom of the machine and they are therefore not detected.

From a database of more than 100 discharges, it is found that the fast electron loss current I^e_{lost} scales depending on the plasma parameters like:

$$I^e_{lost}[mA] = \frac{60\ P^{\alpha}_{LH}[MW]\ \ I^{\beta}_{p}[MA]\ \ B^{\gamma}_{tor}[T]}{n^{\delta}_{l}[10^{19}m^{-2}]} \qquad (2.46)$$

With $\alpha = 1.06 \pm 0.05$; $\beta = 0.76 \mp 0.06$; $\gamma = 0.28 \pm 0.06$; $\delta = 1.96 \pm 0.13$.

The observed parametric dependences are due to a complex mix of several mechanisms, such as the dynamics of the LH wave, in both the configuration and momentum spaces, and the electron trapping process itself. Indeed, at fixed B_{tor} values, the LH power deposition profile tends to broaden and fast electrons are accelerated up to higher energy as I_p increases, while the trapping domain shrinks radially. However, ray tracing and Fokker Planck calculations show that LH power absorption always takes place in the plasma volume where ripple losses occur. Therefore, the increase of I^e_{lost} with I_p, already observed in previous experiments, is probably a consequence of a variation of the mean tail energy. A similar mechanism may also be invoked for the reduction of I^e_{lost} as n_l increases, since the electron tail is driven up to lower energies at high density, as a consequence of the larger plasma collisionality.

The ripple analyses in Tore Supra show that the ripple losses are symmetric in the toroidal direction. This symmetry avoids damages of the plasma facing components. Due to the toroidal procession of the particles (the particle turns several times around the torus before being trapped in ripple wells) the asymmetric ripple losses are small. The large part of the external injected RF power is absorbed in the plasma core (good confinement region), this also contributes to the symmetry of the fast particle ripple losses.
The ripple losses influence the toroidal plasma rotation through the radial transport processes. Locally trapped particle losses induce a return current which generate a $j_r \times B_\theta$ force carried by the thermal ions in the radial direction, to insure the ambipolarity condition. This mechanism appears to be dominant for fast particles.

2.9 Conclusions

In this chapter we summarized the derivation of the fluid equations for mass and momentum, as it is described in the literature. The toroidal and poloidal components of the fluid velocity of the plasma were defined as plasma rotation.
The toroidal rotation profile is calculated using the toroidal momentum balance equation 2.25, when the toroidal forces are known. The radial derivative in this equation indicates that a toroidal force at given position will influence the whole plasma depending on the level of the toroidal momentum transport. The momentum transport in the plasma is governed by the momentum diffusion coefficient which is related to the momentum confinement time by the plasma radius $\chi_{v\phi} = a^2/\tau_\phi$. It is often observed that the energy confinement time is equal to the momentum confinement time.

The toroidal rotation is damped due to the ripple neoclassical effect. Trapped particles (poloidally) do not contribute to the poloidal momentum. Moreover, collisions of passing particles on trapped particles will further slow down the poloidal rotation. The poloidal momentum balance equation has no dependence in the radial direction. It means that the poloidal rotation will only change at the position where the force is applied. There is no transport of poloidal momentum. The poloidal rotation velocity in the core plasma is assumed to be small, because there is no strong poloidal force in that region.

Plasma rotation is also observed in the presence of any external input momentum. The neoclassical expressions of the intrinsic rotation are given in section 2.6. The neoclassical theory doesn't suffice to describe the spontaneous rotation and it is believed that additional models including turbulence give a wide range of prediction on spontaneous rotation.

Diagnostics analyze the properties of the different species in the plasma, and do not consider the plasma as a single fluid. In section 2.6.1, the relation between the impurity rotation and the main ion rotation is given. Also the link between the MHD frequency and toroidal plasma rotation is proposed.

Turbulent transport is also described in order to explain the experimental observations. The drift wave instability is presented as an example of the variety of instabilities which develop in the plasma. The main classes of tokamak instabilities like ITG modes and TEMs, which are believed to be responsible for the anomalous transport of particles, energy and momentum in the plasma core are introduced. Most of them can be ascribed to the drift wave mechanism.

Owing to its impact on the plasma rotation, the definition of magnetic ripple in tokamak is provided, and descriptions of different mechanisms which induce ripple trapping are given. Tore Supra is the most suited machine for the ripple transport analysis because of its high ripple strength (5%). Two ripple diagnostics were installed in Tore Supra and a description of these diagnostics is also delivered.

In this chapter, we have summarized the theoretical needs in order to deal with plasma rotation in rippled devices.

III

Plasma rotation measurement in Tore Supra

It doesn't matter how beautiful your theory is, it doesn't matter how smart you are. If it doesn't agree with experiment, it's wrong.

Richard P. Feynman

3.1. The Tore Supra tokamak

Tore Supra is a circular large size tokamak with a major radius R = 2.4m and a minor radius of a = 0.7m. The machine is equipped with 18 superconducting coils, allowing for a magnetic field up to 4.2 T and long pulse operation. The maximum plasma current in Tore Supra is 1.5 MA, but typically, the machine operates at 0.7 MA. The duration of the discharges is of about a few tens of seconds but a long discharge of about 6 minutes was achieved. The ripple amplitude is strong, around 5% at the plasma boundary, in the low field side under standard plasma conditions. It has a perpendicular diagnostic neutral beam injection (DNBI) in the direction of the plasma current.

For toroidal rotation analyses in Tore Supra, charge exchange recombination spectroscopy is used. Due to its importance for this thesis, it is discussed below in detail in section 3.4. The

main diagnostics that measure the plasma parameters such as the temperature and density are introduced in the following sections.

Tore Supra is a limiter tokamak, but recently, a new project called WEST (A. Becoulet et al., 2013) project (W – for tungsten – Environment in Steady-state Tokamak) with the ambition of transforming Tore Supra from a limiter based tokamak with carbon PFCs into a diverted tokamak with full-tungsten armour, in order to adapt it to a unique relevant facility as a test bed for ITER is under-realization (J. Bucalossi et al., 2011; A. Grosman et al., 2013). The WEST project is targeted at minimizing risks in the support of the ITER divertor strategy, bringing together for the first time actively cooled tungsten component technology in a tokamak environment. Combined with its long pulse active cooling capability, the WEST project will primarily offer the key capability of testing the ITER technology in real plasma environment. In particular, the main divertor (i.e. the lower divertor) of the WEST project will be based on actively cooled tungsten mono-block components and will follow as closely as possible the design and the assembling technology foreseen for the ITER divertor units (inner vertical target – IVT). The new X-point configuration will allow H-mode regimes, hence providing relevant plasma conditions for validating plasma facing component technology. The first plasma of Tore Supra under the WEST configuration is expected for 2016.
This chapter gives a concise introduction to the Tore Supra tokamak, where the main work of this thesis was carried out. A more detailed overview can be found in (P. Garin, 2000; P. Garin et al., 1998).

3.2. Heating systems

The heating of the plasma in Tore Supra is provided by several sources. First, the plasma current supplies the ohmic heating which is typically ~0.8 MW. Additional heating is provided by the radio frequency (RF) heating: the ion cyclotron heating (ICRH), lower hybrid (LH) heating and the electron cyclotron resonance heating (ECRH). A schematic representation of the RF heating system in a tokamak is shown in Figure 3.22.

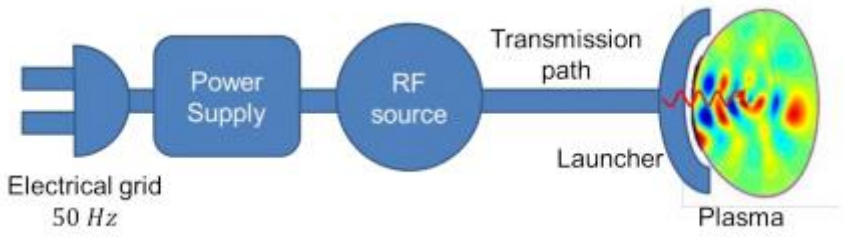

Figure 3.22. *Schematic diagram of R-F heating system in Tokamak* **(J. JACQUOT, 2013)**.

3.2.1. Electron cyclotron resonance heating

The concept of the electron cyclotron resonance heating relies on the property of the movement of charged particles in magnetic fields. They have a cyclotron motion around field lines. By coupling to the plasma a wave whose frequency coincides with the cyclotron frequency of the electrons Ω_e, one can obtain a transfer of the wave electromagnetic energy to the electron's kinetic energy. The corresponding frequency bandwidth is 100 − 200 GHz. As B_T varies as 1/R in the tokamak cross section, the location of the power deposition due to cyclotron resonance can easily be controlled by tuning either the magnetic field or the wave frequency. The possibility of current drive ECCD, and its localization make this method a very powerful tool for tailoring the current profile in a tokamak. The maximum ECRH power available in Tore Supra is around 1 MW

3.2.2. Ion Cyclotron Resonance Heating

An ICRH antenna excites the waves propagating to the plasma center. In the plasma, for densities of the order of 10^{20} m^{-3}, the propagating waves are represented by the fast magneto-sonic waves. When the frequency of the wave is close to the cyclotron frequency of the plasma $\omega_{ICRH} = \omega_{ci}$ the wave is absorbed. The power absorption from the wave induces a change in the distribution function generating a tail in the distribution composed by very energetic ions. The energy gained by the fast ions will be transferred to the bulk plasma by collisions. The frequency range used is from 25 MHz to 100 MHz. The ICRF heating is the main heating system dedicated for heating the ions in the plasma with high efficiency. This method is very developed in Tore Supra.
In the absence of high power neutral beams in Tore Supra, the main additional heating for ions is the ICRH system which plays a central role in plasma scenarios in Tore Supra (H. Kuus et al., 1988).

On Tore Supra, three horizontal ports are dedicated to ICRH antennas. These ports are fed by six transmission lines connected to the RF power plant composed of three modules of two generators each, one per launcher. The six identical RF power lines each feature a synthesizer, a modulator, a solid-state wideband amplifier and a three-stage THALES tetrode amplifier. The high power stage is based on a TH525 tube. The pulse duration is limited to 30 s at nominal power (2.2 MW per generator) and 500 kW in steady-state operation. Because of the launcher electrical circuit, the six 80 m long coaxial transmission lines installed from the generator to the torus hall operate in nearly matched conditions in most situations. They are pressurized to 3 bar of nitrogen to raise the arcing threshold (i.e. lower the sensitivity to arcs). In terms of operation and development, the most critical part of the transmission line is the vacuum window, located just behind the vessel port plate for easy maintenance and replacement. The present thermal limitation of the RF lines is 2.5 MW for 30 s or 800 kW in steady state.

There are several heating scenarios with the fast magneto-sonic ion wave. The two main possibilities are presented here. The first possibility is the *harmonic absorption*. This, happens when the wave pulsation is a multiple of the ion cyclotron frequency ($\omega = n\Omega i$, with *n* an integer). Let us take an example with n = 2. The ion is thus accelerated during half the

cyclotron period and decelerated during the other half. If the wave electric field is homogeneous, there is no net transfer of energy between wave and ion. On the contrary, with an inhomogeneous electric field, the field will be larger on one side of the revolution. There is thus a net transfer of energy. The efficiency of the transfer depends on the inhomogeneity of the electric field (linked to the plasma parameters) and on the Larmor radius of the ion (linked to the perpendicular velocity). The efficiency is also decreasing with increasing harmonic number (M. Brambilla, 1998).

The second possibility is *minority heating*. It consists in adding in the plasma a small quantity (≈ 5%) of another species where the resonant species is largely in minority. The wave frequency is chosen to produce wave-resonance at the fundamental of the minority. The damping zone is localized at the ion-ion hybrid resonance located between the individual cyclotron resonances of the two species. It is desirable for the minority species to have a higher cyclotron frequency than the majority species. In practice, hydrogen (^1_1H) or helium-3 (^3_2He) are chosen in deuterium plasma. The efficiency is independent of the temperature and weakly dependent on the density. The wave energy is then distributed to the majority ions through collisions (F.W. Perkins, 1984). The ICRH discharges that will be discussed in this thesis are in H-minority heating scenarios.

3.2.3. Lower Hybrid Resonance frequency

Another frequency method is the Lower Hybrid Heating and Current Drive. The large parallel electric field carried by LH waves propagating along the magnetic field was shown to lead to strong electron Landau damping and consequently to electron heating and non-inductive current drive (LHCD). The capability to also produce off-axis current allows the development of advanced tokamak scenarios by controlling the current profile to create internal transport barriers in the plasma, in addition to the bootstrap current. The frequency range used is from 1 GHz to 10 GHz.
For the lower hybrid waves to have access to the plasma in this frequency range, the parallel refractive index $n_{\|}$ must satisfy an accessibility condition (R.A. Cairns, 1991). The LH waves are consequently evanescent at the plasma edge and efficient coupling of the waves requires the LH wave's antenna at proximity to the plasma. Furthermore the current drive efficiency is inversely proportional to the square of $n_{\|}$ index: small $n_{\|}$ is favored (R.A. Cairns, 1991). To generate the required spectrum necessary to satisfy to the accessibility condition, antennas composed of multiple phased waveguides are used.

The LH heating system of Tore Supra consists of two types of launchers with passive active multijunction (PAM) (D. Guilhem et al., 2009) and full active multijunction (FAM) units (D. van Houtte et al., 2004). PAM units consist of sixteen modules, each module comprising six active waveguides and six passive waveguides, while FAM units consist of sixteen 500kW klystrons. The two launchers are actively cooled in order to be able to operate in long pulse configuration, up to 1000 s (low power operation). The maximum power expected to be coupled to the plasma with the present system is in the range of 5–6 MW (short plasma discharges). LH waves are launched into the plasma with a parallel refractive index $n_{\|} = c\ k_{\|} / \omega$ between 1.5 and 3.2.

Expected wave-induced momentum input is in the counter-current direction (the electrons being accelerated). The LH power deposition is off-axis, with a maximum deposition at *r/a* ~ 0.3, then decreasing towards the edge with a minimum power deposition at *r/a* ~ 0.7. As usually observed in Tore Supra, the deposition profiles broaden and the maximum deposition location is shifted outwards when the plasma current increases (Y. Peysson et al., 1996; F. Imbeaux et Y. Peysson et al., 2005).
In Tore Supra, a total injected power of about 10 MW was coupled to the plasma. The Figure 3.23 summarizes the three frequency ranges used for additional heating systems.

Figure 3.23. *Diagram showing the frequency bandwidths used to heat or for current drive in tokamaks.*

The main Tore Supra parameters are indicated in the Table 3.2, together with expected WEST and ITER parameters as a perspective.

	Tore Supra	WEST	ITER
Major radius *R* (m)	2.5	2.5	6.1
Minor radius *a* (m)	0.7	0.5	2.0
Ellipticity κ	1	1.3-1.8	1.85
Plasma volume (m^3)	25	15	830
Plasma current I_p (MA)	1.5	0.5-0.8	15
Magnetic field amplitude B_T (T)	3.8	3.7	5.3
Configuration	Pumped limiter	Divertor	D- divertor
Fuel mix	D-D	D-D	D-D/D-T
Pulse duration (s)	100	1000	400 (3000)
ICRH power (MW)	12	9	20 (40)
LH power (MW)	7	7	0 (40)
NBI power (MW)	0.5	0	33 (50)
ECRH power (MW)	0.8	0.8	20 (40)
Fusion power (MW)	10^{-3}	10^{-3}	500
Amplification power *Q*	<<1	<<1	>10

Table 3.2. *Principle parameters for Tore Supra, WEST and ITER tokamaks.*

3.3. Diagnostics

The plasma parameters that are important for this thesis are the plasma rotation velocity, the ion and electron temperatures and the density. In the following paragraphs several diagnostics capable to measure these parameters are introduced. The charge exchange recombination spectroscopy is fully described in the next section due to its importance for this thesis. A description of the main diagnostics available in Tore Supra can be found in (C. Gil et al., 2009).

3.3.1. Electron Cyclotron Emission

The electrons that gyrate around the magnetic field lines emit electron cyclotron radiation. At the electron cyclotron frequency the plasma is optically thick. This means that the electron cyclotron emission (ECE) is black body radiation. According to the Raleigh-Jeans law, the long wavelength approximation of Planck's law, the intensity of black body radiation is related to the temperature. The ECE intensity is therefore proportional to the electron temperature T_e. The frequency of the ECE radiation $\omega_e = eB/m_e$ is proportional to the magnetic field B that in turn depends on the major radius R. This means that the ECE intensity as a function of frequency can be transformed to the electron temperature as a function of major radius: $T_e(R)$. Microwave detectors with a high sampling rate allow for measurements of $T_e(R, t)$ profiles with fast time resolution. An absolute measurement of the intensity is needed, which means that an intensity calibration of the detectors is needed. This can be done by using a 'hot' source or by cross calibration with another T_e-diagnostic like e.g. Thomson scattering.

A 16-channel heterodyne radiometer, 2 GHz spaced, is used on Tore-Supra to measure the electron cyclotron emission in the frequency range 78-110 GHz for the O-mode and 94 -126 GHz for the X-mode. In the equatorial plane, a dual polarization Gaussian optics lens antenna, with a perpendicular line of sight (with respect to the magnetic field), gives ECE measurements with very low refraction and Doppler effects. A separate O/X-mode RF front-end allows the use of an IF electronic mode selector. This improves time stability calibration and gives the potentiality of simultaneous O/X-mode measurements in the 94 -110 GHz RF band for polarization studies (C. Gil et al., 2009).

A precise absolute spectral calibration is performed outside the vacuum vessel by using a 600°C black body, a digital signal averaging on the waveform generated by a mechanical chopper placed directly in front of it , and a simulation window without Fabry-Pérot effects.

3.3.2. Thomson Scattering

The Thomson scattering diagnostic is based on the scattering of laser light byt free electrons. The velocity of the electrons causes the scattered light to have a Doppler shift with respect to the wavelength of the incoming laser light. For a Maxwellian velocity distribution of the electrons, the spectrum of the scattered light has a Gaussian shape. The width of the spectrum gives the electron temperature T_e. The intensity of the scattered light is proportional to the

electron density n_e. So apart from being a T_e measurement, Thomson scattering provides a n_e measurement as well. For the density measurement an absolute calibration is needed. The scattered light originates where the laser passes through the plasma. Imaging the scattered light therefore gives the local T_e and n_e along the path of the laser light. For Thomson scattering measurements a powerful laser is needed, so that the intensity of the scattered light is high enough. It also has to be a pulsed laser, so that the scattered light rises significantly above the plasma background light.
Currently, in Tore Supra there are 12 spectrometers in use on the Thomson scattering diagnostic. In 2009 one spectrometer was replaced by a new spectrometer prototype to improve the signal to noise ratio during plasma heating phase. There are three channels in the spectrometer. Each of them has an electronic chain composed of avalanche photo diode (APD), a trans impedance amplifier (TIA) and a line driver amplifier (10×). A sampling rate of 2 GHz and a 100 ns window sampling width is required to make efficient noise reduction. The real time calculation must be accomplished for each laser shot at a 27 Hz rate.

3.3.3. Interferometry

Another technique for measuring the electron density is interferometry. In interferometry the light of a laser beam that has gone through the plasma is compared with that of a reference beam that travelled over the same length, but in vacuum. As the phase velocity of laser light depends on the refractive index of the medium it is going through – plasma for one beam, vacuum for the reference beam – there is a phase difference between the light of the plasma beam and the reference beam. From the interference pattern of the two beams the phase difference and thus the line-averaged refractive index of the plasma can be determined. The refractive index of plasma is proportional to the electron density, so that interferometry yields the electron density n_e averaged over the line along which the laser passes through the plasma.

In Tore Supra, it is a Mach-Zender interferometer, with the frequency in one arm shifted 100 kHz by a rotating grating. The line density measurement is obtained by the phase change measurement between a probing beam and the reference beam. Because the change of the path length is of the order of 400 μm during a discharge, it is necessary to add a second wavelength phase measurement. For each channel, the two 119- and 195-μm beams are superposed along the plasma crossing and then are separated toward two detectors, either by a plane grating or by a 60-μm Mylar sheet.
A combined far-infrared (FIR) interfero-polarimeter diagnostic is used for electron and current density measurements in Tore Supra. The sources are two H_2O and DCN lasers, at 119- and 195-μm wavelengths. Continuous 5 kV/1A discharges are maintained in 3-m-long double-envelope tubes and deliver a power of, respectively, 30 and 150mW. The beam transport is done by plane and focusing mirrors positioned to minimize the Gaussian diameters of the infrared beams; they are mounted in dried air boxes. The separation and recombination plates are thin films of Mylar and Kapton. The detectors are helium-cooled InSb and GeGa bolometers.

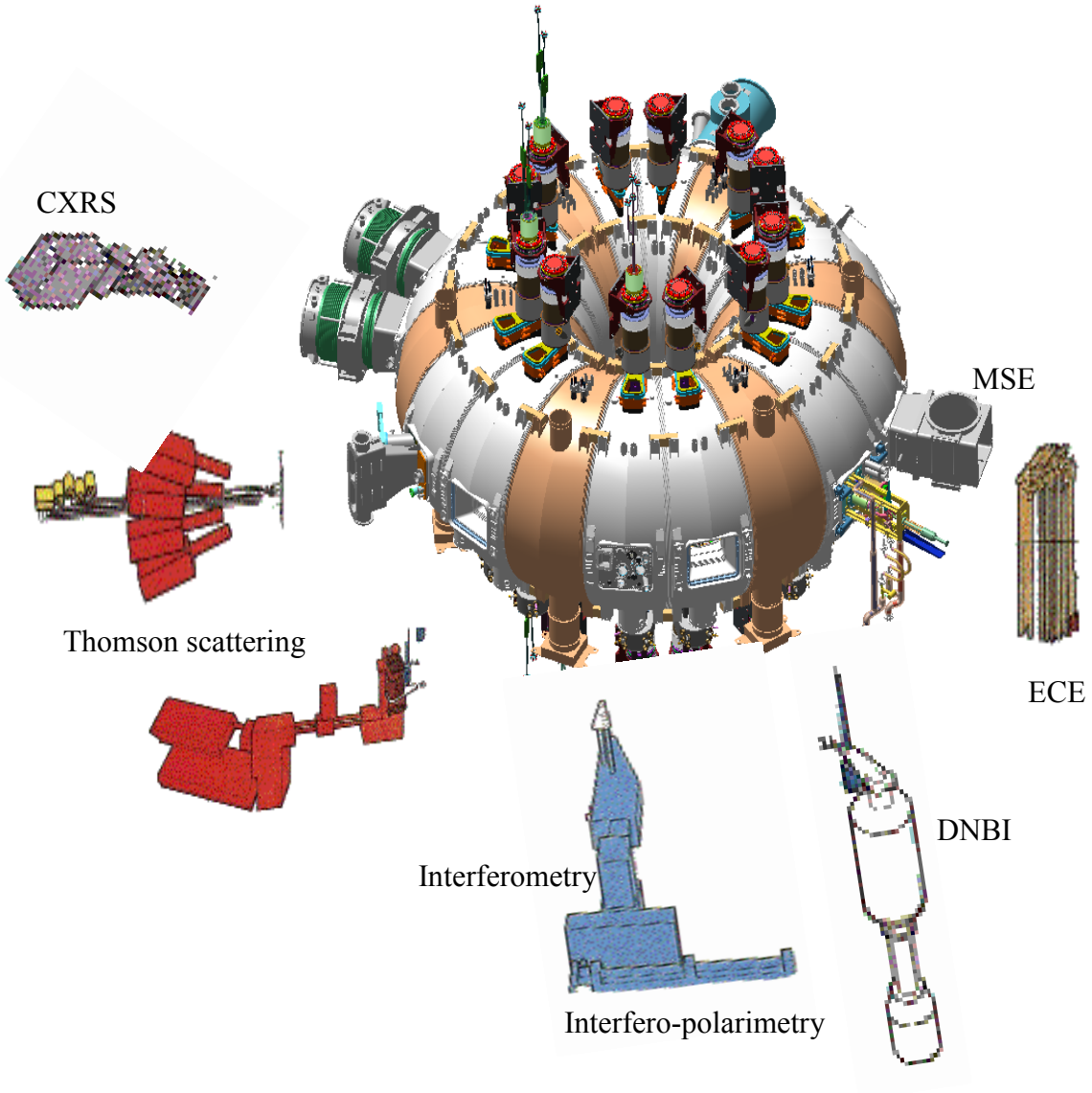

Figure 3.24. *Schematic view of Tore Supra with the pertinent diagnostics for this thesis.*

3.3.4. Magnetics

The Tore Supra magnetic diagnostics measure the variations of the magnetic field vector along the radial, poloidal, and toroidal directions, as well as the vertical flux and the toroidal flux variations. The amplitude of these parameters differs by several orders of magnitude; therefore, sensor design and equivalent surface area are different. Six types of sensors are mainly used. The shape of the coils is a compromise between the tokamak geometrical constraints and the area of the sensor that is linked to its magnetic field sensitivity. For this reason, some sensors have an elongated cross section, making the wiring particularly delicate. To minimize stray fields and avoid noise in the signal, there is an even number of layers of windings. To minimize the number of connections in the vacuum vessel, the electrical wire of

the magnetic diagnostic sensors is long enough to be twisted, and to reach its assigned feed-through a few meters away.

To reconstruct the equilibrium of the plasma a real time code EFIT (W. Zwingmann, 2003) is used. The EFIT code is able to use data from the Faraday rotation, motional Stark effect (MSE), total kinetic pressure, safety factor, and the diamagnetic effect of the plasma. The safety factor is not readily available and requires careful pre-processing of experimental data. The EFIT used in Tore Supra takes into account the measurements of far infrared polarimetry. A transport code CRONOS (J-F. Artaud et al., 2010) that solves the diffusion equations is also used to calculate the current density profiles and *q*-profiles with high accuracy.
The above described diagnostics are illustrated in Figure 3.24.

3.4. Charge Exchange Recombination Spectroscopy

3.4.1. Introduction

The study of the plasma rotation requires a reliable method to measure that rotation. Charge eXchange Recombination Spectroscopy (CXRS) is a powerful technique which allows local measurements of the ion velocity distribution. Then the ion temperature and the fluid velocity are derived. In CXRS, the Doppler shift and the broadening of the line emission by ions in the plasma are a measure of the fluid velocity and the ion temperature. Line emission in the plasma doesn't occur spontaneously, but an atomic reaction by receiving at least one electron is necessary. The ions in the plasma are fully stripped, except for heavy ions which permits the charge exchange reaction. Neutral ions are provided by neutral beam injection which delivers at least one electron to the plasma ions during the charge exchange recombination spectroscopy. The ion receives this electron in a high quantum level. It will return from its excited state to the ground state, losing its excess energy through line emission.
In the literature (M. von. Hellermann et al., 1995; R. C. Isler, 1994), a complete description of the charge exchange recombination spectroscopy is provided. In this chapter, the necessary elements to understand and interpret the measurements of toroidal rotation in Tore Supra are given.

3.4.2. Principle of the diagnostic

The charge exchange reaction and the impurity choice

During the charge exchange reaction, an electron is transferred from the neutral atom to the ion. The electron is most likely transferred to a specific preferential quantum level of the plasma ion depending on the type of the neutral atom and the ion. The probability for an electron to be

transferred to both lower and higher quantum levels deceases monotonically (R. C. Isler, 1994).

For the reaction $H + C^{6+} \rightarrow H^{+} + C^{5+}$ the C^{5+} level most likely to be populated is $n = 4$, but also for the levels $n = 7$ and $n = 8$ the chances of population are significant. These quantum levels differ from the ground levels (M. von. Hellermann et al., 1995). It means that during the charge exchange reaction the resulted ion is in an excited state and it will return to the ground state after a cascade of transitions (Figure 3.25). The wavelength of the emitted radiation by the transitions varies over a wide range depending on the populated states. The transitions that emit visible light are of interest, the advantage is that it can be easily collected and also plenty of spectroscopical techniques are available for the analysis.

In Tore Supra, the $n: 8 \rightarrow 7$ transition of C^{5+} is used. The emission is in the visible and it has a wavelength of 529 nm. The charge exchange reaction is analysed for the carbon impurity instead the bulk ions hydrogen and deuterium because of the high complexity of the hydrogen-deuterium spectrum.

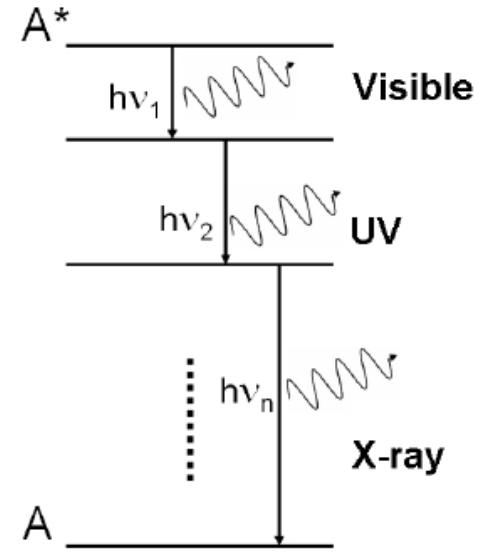

$$H + A^{+} \rightarrow H^{+} + A^{*}$$
$$\rightarrow H^{+} + A + h\nu_1 + h\nu_2 + \ldots$$

Figure 3.25. *Diagram of cascade of transitions from exited state to ground state.*

In the plasma the charge exchange (CX) emission lines of deuterium and hydrogen overlap. Apart from CX emission, neutral deuterium and hydrogen in the plasma edge have a strong line-emission due to excitation by electrons. This emission lies in the same wavelength range as the charge exchange emission. Finally the neutral beam species is commonly hydrogen as well, resulting in a beam spectrum on top of the charge exchange spectrum. As a result one

gets a spectrum that is the sum of two charge exchange lines, electron excited emission and beam emission (M. von. Hellermann et al., 1995).
Decomposing this spectrum into its components in order to regain the charge exchange line results in large error bars on the derived quantities.

The most common used impurities are helium and carbon because helium is the reaction product of the fusion reaction and the carbon spectrum is easy to analyse and the carbon is always present in tokamaks since it is commonly used as a wall material.
The measured temperature, rotation velocity and density are those of the carbon. The energy transfer time between hydrogen and carbon is shorter than the energy confinement time. This means that the assumption of the bulk ion temperature by the carbon temperature is valid. The carbon rotation is different from the bulk rotation. In section 2.6.1 the expression of this difference is given (A. Romannikov et al., 2000), nevertheless, this difference is usually small (B. A. Grierson et al., 2012; D. Testa et al., 2002) and therefore can be neglected. The measurement of the carbon density profiles are used for impurity transport studies.

3.4.3. Spectral line analysis

Doppler width and shift

The CVI emission has a natural wavelength of $\lambda_n = 529\ nm$ and natural line width of $\Delta\lambda_n = 5.10^{-5}\ nm$ (National Institute for Standards and Technology). If an ion moves with a velocity u_z in the direction of the observer, the light emitted by this ion experiences a Doppler shift $\Delta\lambda_d = u_z/c\ \lambda_n$. For an ion temperature of 10 eV, the Doppler shift due to the thermal velocity is $\Delta\lambda_d = 5.10^{-2}\ nm$. Compared to this Doppler shift, the natural line width can be neglected. The emission line is then described by the delta-function $f(\lambda) = \delta\ (\lambda - \lambda_n\ \left(1 + \frac{u_z}{c}\right))$.
Considering a Cartesian system, the emission intensity coming from a volume (dx, dy, dz) around the point (x, y, z) depends on the density of the neutral hydrogen, the density of the carbon ion and the effective emission rate $< \sigma v >$. This effective emission rate depends on the cross-section σ for charge exchange reactions and expresses the likelihood of interactions between carbon and hydrogen in which the $n = 8$ state is populated.

The Maxwellian distribution of the carbon ion velocity is:

$$g(u_x, u_y, u_z) = \sqrt{(\frac{m_c}{2\pi T_c})^3}\ \exp(\ \frac{(u_x - u_x)^2 (u_y - u_y)^2 (u_z - u_z)^2}{2T_c/m_c}) \qquad (3.1)$$

where u_x, u_y, and u_z are the component of carbon velocity.
The spectrum coming from the volume (dx, dy, dz) emitted in the direction z then is:

$$f_{local}(\lambda) = \frac{1}{4\pi} n_H n_C \iiint < \sigma v > \delta \left(\lambda - \lambda_n \left(1 + \frac{u_z}{c}\right)\right) g(u_x, u_y, u_z)\ du_x\ du_y\ du_z$$

$$f_{local}(\lambda) = Iexp\left(-\frac{\lambda-\lambda_0}{\Delta\lambda^2}\right) \tag{3.2}$$

where:

$$\lambda_0 = \lambda_n\left(1+\frac{u_z}{c}\right)$$

$$\Delta\lambda = \sqrt{2T_c/m_c}\frac{\lambda_n}{c}$$

$$I = n_H n_C \frac{\lambda_n < \sigma v >}{4\pi^{3/2} c\,\Delta\lambda}$$

We can see that from the above equation we can derive the carbon velocity in the direction *z* from the peak position of the Gaussian line emission, the carbon temperature from the width of the Gaussian and the intensity of the Gaussian line gives us the carbon density.

The observed charge exchange spectrum results from the sum of the all light locally emitted along the line of sight:

$$f(\lambda) = \int Iexp\left(-\frac{\lambda-\lambda_0}{\Delta\lambda^2}\right) dz \tag{3.3}$$

In the plasma we can consider that there is no neutral hydrogen $n_H = 0$. The neutral particles in the plasma originate from two regions: from the wall, the neutral particles will penetrate a certain distance into the plasma before ionisation and from the neutral beam which injects neutral highly energetic particles over the whole way till the plasma centre. From this, we can deduce that on the line of sight, there are two positions where the neutral density is not null: where the line-of-sight goes through the plasma edge and at the position where the line-of-sight crosses the neutral beam. It means that the spectrum can be split in two parts: a passive charge exchange component from the plasma edge and an active component due to the neutral beam. The two components are shown in Figure 3.26. The passive spectrum contains only the data from the edge while the active spectrum ensures local measurements over the whole minor radius of the plasma (with multiple lines of sight).

$$f(\lambda) = \left(\int Iexp\left(-\frac{\lambda-\lambda_0}{\Delta\lambda^2}\right) dz\right)_{passive} + \left(\int Iexp\left(-\frac{\lambda-\lambda_0}{\Delta\lambda^2}\right) dz\right)_{active} \tag{3.4}$$

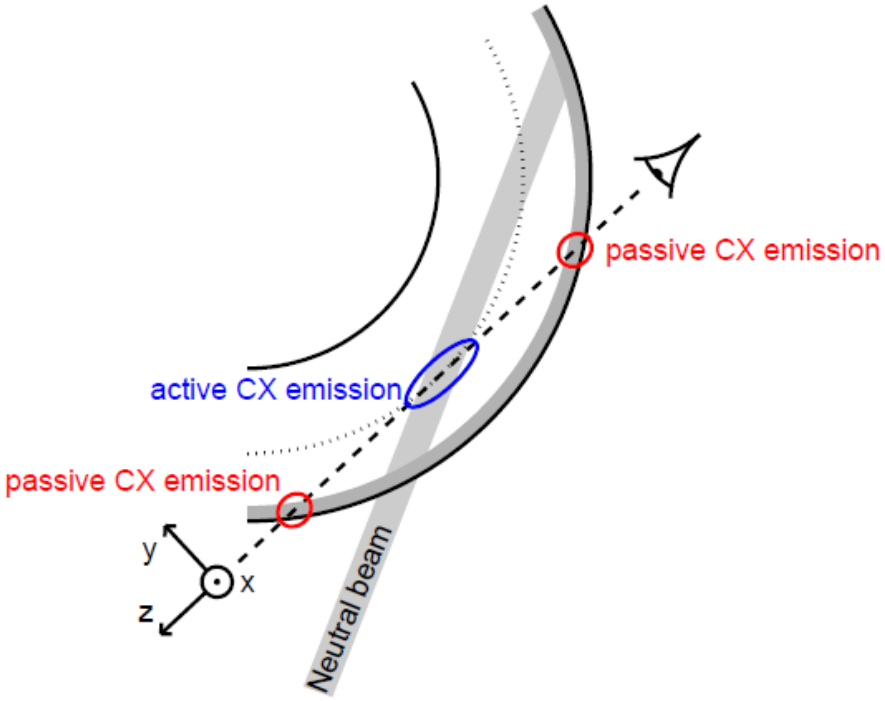

Figure 3.26. *A top view of a tokamak with a CX line-of-sight. The passive component of the CX spectrum is caused by neutral particles in the edge, the active CX signal is emitted where the line-of-sight crosses the neutral beam.*

The line of sight is tangential to a flux surface where it crosses the neutral beam (Figure 3.26). Then the active part of the spectrum becomes:

$$f_{active}(\lambda) = I \ exp\left(-\frac{\lambda - \lambda_0}{\Delta\lambda^2}\right) \qquad (3.5)$$

with

$$\lambda_0 = \lambda_n \left(1 + \frac{V_z}{c}\right)$$

$$\Delta\lambda = \sqrt{2T_c/m_c}\frac{\lambda_n}{c}$$

$$I = n_C \frac{\lambda_n < \sigma v >}{4\pi^{3/2} c\, \Delta\lambda} \int_{beam} n_H \, dz$$

The active part of the CX spectrum provides the local measurements of n_C, T_C and V_z. If we assume that the radial fluid velocity of the carbon is much smaller than the toroidal and poloidal component, we can write $V_z = V_\phi \cos\alpha + V_\theta \cos\beta$ where α is the angle between the line of sight and the toroidal direction and β is the angle between the line of sight and the

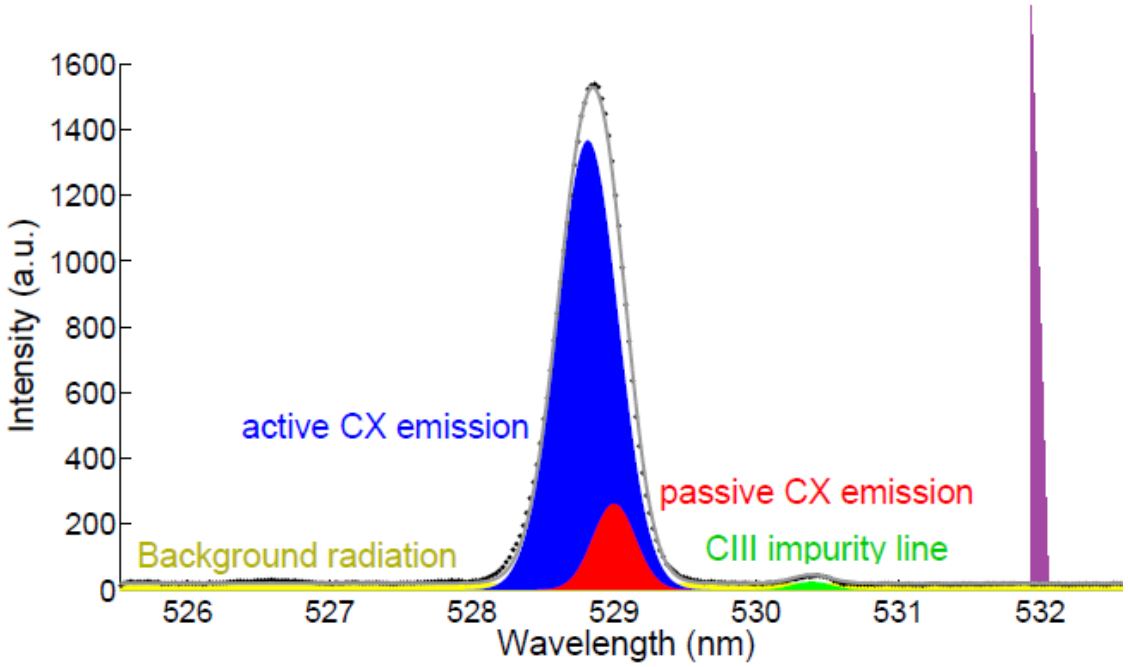

Figure 3.27. *A typical CX spectrum. The black dots represent the measured spectrum, the solid gray line is the result of a fitting routine. The different components of the CX spectrum are indicated: the active CX in blue, the passive CX in red, a CIII impurity line in green and the background radiation is yellow. The laser line is also show in violet* (M. De Bock, 2006).

poloidal direction. When we choose the line of sight perpendicular to the poloidal direction, V_z is proportional to the toroidal direction.

To extract the active spectrum from the total spectrum, two methods can be used. The first is based on the neutral beam modulation. The passive spectrum is measured when the neutral beam is switched off and then subtracted from the total spectrum measured when the neutral beam is switched on, only the active spectrum remains. This method is often used; however, there are some disadvantages. It presents a loss in time resolution because the beam is switched off half of the time. The second weak point is that we assume that the passive spectrum is the same with and without the neutral beam. But a neutral beam can change the edge conditions of the plasma. This method also increases the error bars.

The second method consists on modeling the passive CX spectrum. For this modeling, measurements of temperature and density at the plasma edge can be used as well as the spectrum by a line of sight that does not cross the neutral beam. However, a very accurate model is necessary.

In the wavelength range of passive and active CX emission, light from other sources is also present; e.g. a continuum background of Bremsstrahlung and line radiation from partly ionized impurity ions. In Figure 3.27 a measured charge exchange spectrum is given. When this spectrum is fitted, all different components – active CX, passive CX, impurity lines and background radiation – have to be taken into account.

In Tore Supra, a laser line at $\lambda = 532.04\,\mathrm{nm}$ is used as reference line for the Doppler shift calculation. This line is present during the entire discharge and it is injected in the all lines of

sight. The position of this line is fixed during the calibration campaign and remains stable during the experiments. The system allows us to determine very accurate toroidal rotations with small error bars.

3.4.4. Other mechanisms contributing to the spectrum

Several other mechanisms cause a broadening and shift of the CX emission lines. Passive and active spectra are not the only emission in the measured wavelength range and they complicate the charge exchange spectrum. We can mention the line emission from the edge impurities, the secondary emissions from the CX ions and the background emission et cetera. A discussion of those effects will be led in this section.

The energy dependence of the emission rate

In the previous section the effective emission coefficient $< \sigma v >$ is considered constant. But as shown in (M. von. Hellermann et al., 1995) this coefficient depends on the collision velocity between the neutral particles and the plasma ions. This collision velocity has a distribution around the neutral particle velocity. If the value of $< \sigma v >$ changes significantly around the neutral particle velocity or if the distribution of the collision velocity is wide, the effective emission coefficient $< \sigma v >$ cannot be taken out of the integral in the equation 3.2.

The result of the collision rotation distribution and the dependence of $< \sigma v >$ on this collision velocity is a change in Doppler shift and Doppler broadening of the emission line. This will induce effects on the measured temperature, velocity and density. Usually the width of the emission line is smaller than expected, which means that the observed temperature is smaller than the real temperature. Due to the low temperature in Tore Supra (few keV), we can neglect this effect for Tore Supra. The reason for that is the geometry of the core CXRS in Tore Supra, where the lines of sight are almost perpendicular to the neutral beam system (M. von. Hellermann et al., 1995). The energy dependence of $< \sigma v >$ is also responsible for a shift in poloidal rotation due to the effect on the gyro-motion of the ions. Despite the higher temperature that we can achieve in ITER, this effect will also be negligible.

Non-thermal line broadening effects

Broadening effects of the CX emission line that are independent on the ion temperature are observed. In this section we will discuss two effects: the Zeeman effect due to the magnetic field and *l*-state mixing (R. C. Isler, 1994).

Non-degeneracy of the l-state: the $n = 8$ and $n = 7$ levels of the ion C^{5+} have a substructure. There is a number of possible transitions between the $n = 8$ and $n = 7$ levels. The energy of the transition depends on the sublevels of $n = 8$ and the sublevels of $n = 7$.

The energy level diagram of the C^{5+} ion is shown in Figure 3.28. For each principal quantum number n, there are orbital quantum numbers: $l = 0, \dots, n - 1$ and also referred as s,p,d,f,… orbitals. When electron spin is taken into account each l level – except l = 0 – splits in two

levels, defined by $\mathrm{J} = l - 1/2$ and $\mathrm{J} = l + 1/2$. The allowed radiative transitions between the $n = 8$ and $n = 7$ level are those for which $\Delta l = \pm 1$ and $\Delta\mathrm{J} = 0, \pm 1$.

Due to the fine-structure each allowed transition has a slightly different wavelength, and the total emission spectrum consists of a set of lines instead of one line.

The populated l levels depend on the neutral beam. If the life time of the exited state is larger than the ion-ion collision time, collisions will induce a transfer between the different l states of $n = 8$ before the charge exchange electron drops to the lower level and emits a photon. This phenomenon is called collisional l mixing. It induces a statistical population of the l levels. If the all l levels are populated, 37 transitions are possible instead of one. Then, the measured spectrum consists of by 37 lines and covers a wavelength range of about 0.015 nm which corresponds to a Doppler broadening of about 4 eV.

Zeeman effect: The energy levels in the same principal quantum number n are slightly different due to the fine structure. The presence of high magnetic fields in tokamaks, will cause a Zeeman effect, which consist of splitting of one J level into $2\mathrm{J} + 1$ energy levels separated by $\Delta E = \mu_b g B m_j$, $m_j = -J, \ldots, +J$, where μ_b is the Bohr magneton ($5.789.10^{-5}$ eV/T) and g the Landé factor (depends on l, J and the spin, of the order 1). The allowed transitions are now: $\Delta l = \pm 1$, $\Delta\mathrm{J} = 0, \pm 1$ and $\Delta\mathrm{m}_j = 0, \pm 1$. The estimation of Zeeman split gives $\Delta\lambda = 0.03\mathrm{nm}$.

In the CX spectrum, the total profile of the all transitions is presented as a single but broadened Gaussian where the width and the peak position of the line depend on the l mixing and Zeeman splitting. The non-thermal broadening puts a lower limit to the ion temperature measurements with CXRS.

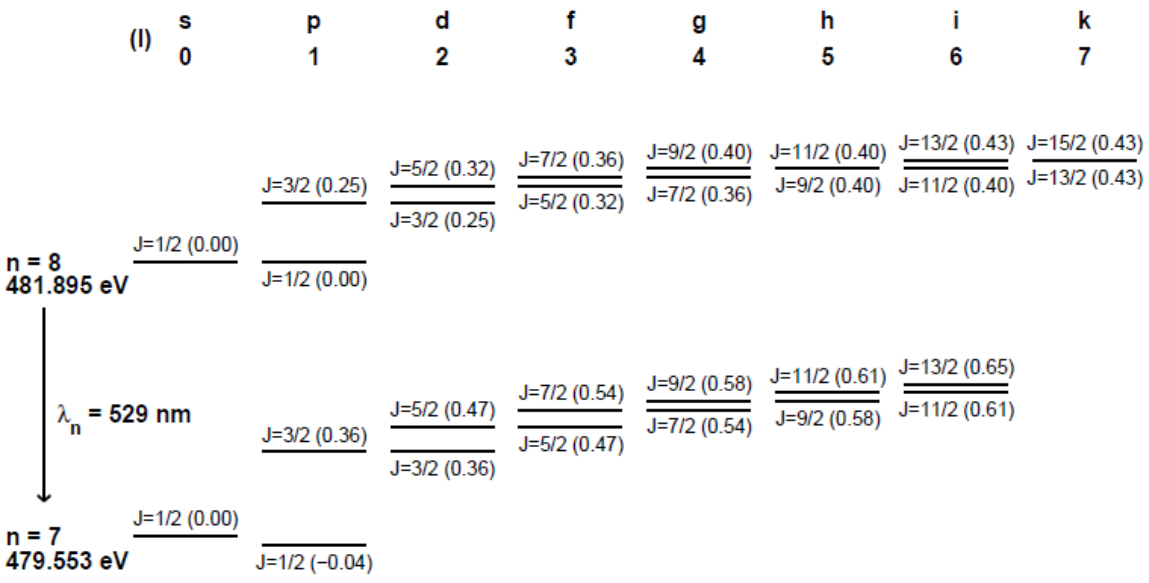

Figure 3.28. *Energy level diagram for the principle (n = 8)- and (n = 7)-shells of CV+. Each principal n-shell is divided in l-subshells and J-levels. The energy within the principal n-shell differs slightly. That difference is exaggerated in this plot. The energy difference with the (l = 0)-level, within the same n-shell, is given in parentheses. The energy level of the (l = 0)-level, for both n = 8 and n = 7 is given at the left (eV)* (National Institute for Standards and Technology)

Non-Charge Exchange emission

In the same wavelength range, there is not only the charge exchange emission, but other parasitic emissions are present. Some of them are totally different from the charge exchange reaction and others are secondary effects of charge exchange. When the CX active emission is low (in the plasma centre for example where the neutral beam density is low), those parasitic emissions will hide the active emission and therefore make the measurements impossible to realise.

Halo and Plume

In a charge exchange interaction a plasma ion receives an extra electron. After some time it will of course lose this electron again. However, if the ionisation time is long enough, the plasma ion can be excited again by electron impact. This causes a delayed, secondary emission. This secondary emission is especially important for low Z ions, like hydrogen and helium, because they don't have to be excited to a high level in order to emit visible light. For C^{5+} the electron impact should excite the ion from the ground state n = 1 to the n = 8 state in order to have a secondary emission at 529 nm. The chance for such an excitation by electron impact is negligible.

If the plasma ion remains charged after the CX interaction, it still moves along the magnetic field and the delayed emission is seen as a 'plume'. If the plasma ion is neutralized in the CX interaction, e.g. when H^+ or He^+ undergoes a CX reaction, it is no longer confined to the magnetic field and it can escape in all possible directions. The delayed emission is therefore called a 'halo'.

Impurity lines

Due to the low temperature at the edge of the plasma, there are several non-fully stripped particles (impurity ions) which can be excited by electrons and therefore emit radiation. If the wavelength of these impurity lines overlaps the wavelength of the CX emission, the analysis of the spectrum will be complicated. To surmount this difficulty the impurity emission can be done in the same way as the passive CX emission.

Impurity emission can be useful is some cases. If the wavelength of the impurity line is different from the CX emission, the impurity line can be used as a real time wavelength calibration. At the edge the temperature is very low and the velocity is very small, such that the emission line is narrow (the peak position can be determined easily) and the Doppler shift is negligible (its position can be considered as fixed). The measured pixel position of this impurity line on the camera, together with the known λ, is then used to derive the relation between the pixels on the camera and the wavelengths.

Bremsstrahlung

Continuum emission is also observed in the spectrum, this emission is due to the Bremsstrahlung generated by the relative movements of the charged particles in the plasma (J. Wesson, 1997).

The continuum emission depends on the square of the plasma density and the $Z_{eff.}$ For example in ITER this effect will be significant and could therefore impact the active CX-signal.

3.4.5. The CXRS diagnostic in Tore Supra

The charge exchange recombination spectroscopy system installed in Tore Supra uses a low power diagnostic neutral beam. The lines of sight of the system are tangential to the toroidal direction and are mainly used for the ion temperature and toroidal rotation measurements. In Tore Supra, one peculiar specificity of the system is that it uses a laser as a reference line for the Doppler shift of spectral lines in order to get very accurate measurements of toroidal rotation.

The device has fifteen tangential viewing lines allowing for a spatial coverage from the plasma core to r/a = 0.9 normalized minor radius in the equatorial plane, with 2 cm spatial resolution at the plasma edge and 6 cm in the core. They are plotted in Figure 3.29. These lines are all located in the equatorial plane and are directed tangentially to the flux surfaces.

Diagnostic Neutral Beam Injection characteristics

A diagnostic neutral beam injector DNBI system is used on Tore Supra to measure the ion temperature and plasma rotation profiles by spectroscopic methods: CXRS. It is worth mentioning that the DNBI is also used for MSE to measure the plasma current profiles. The diagnostic NBI system is a modified version of the previous Tore Supra heating injectors (P. Bayetti etal., 1988); it is based on the energy recovery concept where the non-neutralized beam fraction is electrostatically decelerated and recovered at low energy. Although the NBI is routinely operated in hydrogen at 60 keV / 375 kW (up to 70 keV / 450 kW has been obtained), it can also work in deuterium up to 90 keV / 700 kW.

The NBI system consists of a box housing one injector connected to the torus via a gas-tight valve, and spatially oriented to provide a nearly tangential neutral beam with an incidence angle of 23 deg with the plasma perpendicular at the plasma entrance. The provided beam power is high enough to allow a large neutral density up to the plasma center and therefore the resulting CX signal is high. In normal operating conditions the time resolution is 30 ms, but faster sampling is possible up to 10ms. The radial resolution of the measurements is about 2 cm.

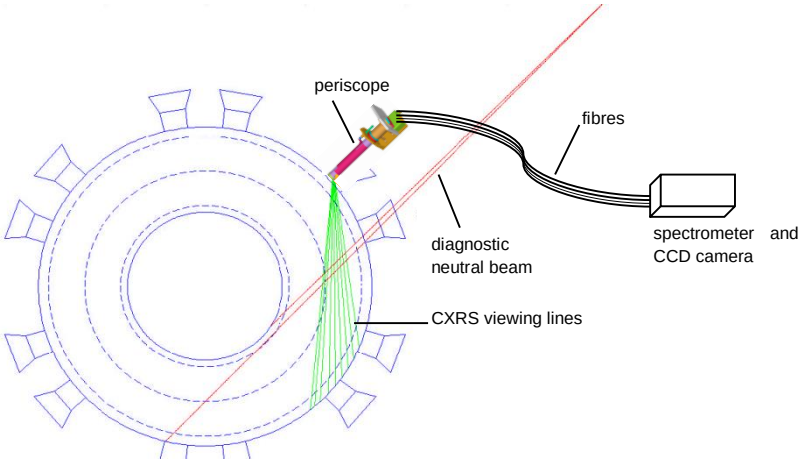

Figure 3.29. *The NBI-CXRS setup at Tore Supra. The top view of Tore Supra with the set of lines-of-sight. The red beam represents the DNBI system. Also shown, the CCD camera, the fibers and the periscope.*

The input torque from the DNBI in Tore Supra is expected to be low. Experimental evidence is provided by Doppler reflectometry measurements. The perpendicular fluctuation velocity measured by Doppler reflectometry (P. Hennequin et al., 2006) $V_\perp = V_{E\times B,\perp} + V_{fluc}$ has been compared in several times before, during and after the DNBI. The Figure 3.30 shows the Doppler frequency spectra during and after DNBI. One can see that there is no significant change between the two spectra; the observed slight change is due to the slight modification of the electron density during the DNBI.

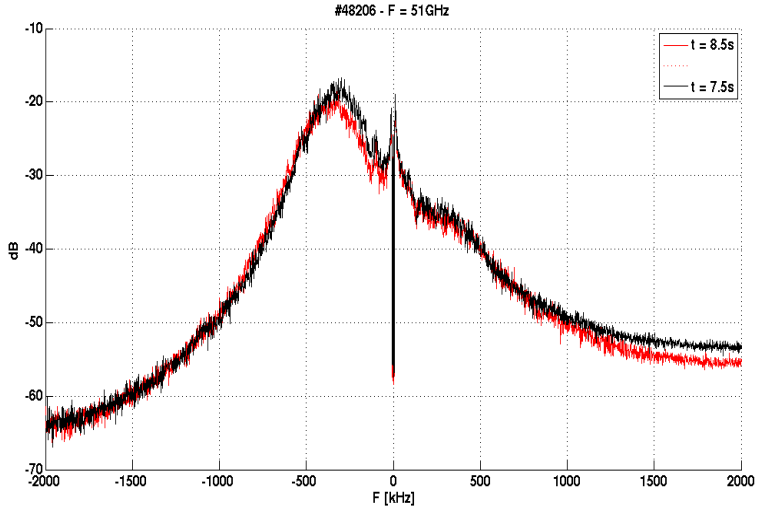

Figure 3.30. *Frequencial Doppler spectrum before and during the DNBI. The very slight difference between the two spectra is due to the slight density change during the DNBI.*

The calculation of the perpendicular velocity is presented in Figure 3.31. It can be noted that there is no significant difference between the perpendicular velocities calculated at different times: before, during and after the DNBI. The projection of the force balance equation in the radial direction reads: $E_r - V_\phi B_\theta + V_\theta B_\phi = \frac{\nabla p}{en}$. Assuming that the toroidal rotation is the dominant term, one can find that $V_{E\times B,\perp} = V_\phi B_\theta / B_\phi$. If the perpendicular velocity remains constant over the DNBI pulse, we can state that the toroidal rotation remains constant as well (at least over the plasma radius interval where measurements are performed). In other words, it means that the DNBI torque is likely very small and can be neglected in our analyses.

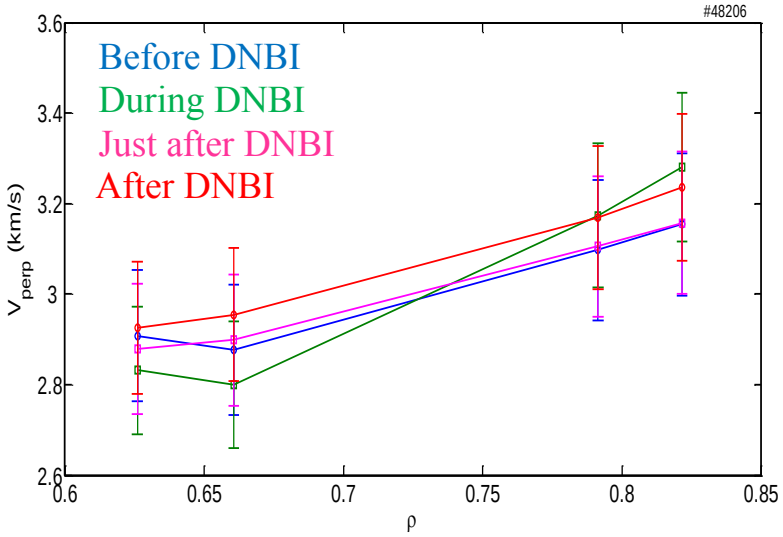

Figure 3.31. *Perpendicular velocities calculated from Doppler reflectometry measurements before, during and after the DNBI.*

In order to confirm this statement, simulations of neutral beam induced-fast ions in steady state have been performed with the SPOT (M. Schneider et al, 2005) code. Figure 3.32 shows the radial profiles of the torque contribution from the DNBI with and without ripple. While the initial torque without ripple peaks at 0.12 N/m^2 in the plasma center (co-current), it becomes negative for 0.6 < ρ < 1 because the ripple induces a counter-current torque which is large enough to cancel the co-current torque in this region. The integration of the local momentum over the core plasma volume (ρ < 0.6) gives a torque of about ~ +0.54 N.m, which corresponds to an increment in toroidal rotation of about ~4 km/s, provided the total momentum stored inside the plasma can be approximately: $T_{DNBI} \approx \Delta V_\varphi 2M_i R/\tau_\phi$, where τ_ϕ (50-100 ms) and M_i is the total mass of the plasma in this region. In conclusion, although this would need to be confirmed by momentum transport simulations in order to obtain the rotation profiles, the DNBI induced torque can be considered as negligible.

.

In this thesis, one can reasonably state that the DNBI effect on the plasma rotation in Tore Supra can be neglected. Even if short and low power DNBI pulses typically 200 ms at 0.3–0.6 MW have been used for CXRS measurements, the analyses have been performed just after the application of the DNBI pulse with time resolution between 10 and 30 ms, hence, well adapted for the intrinsic rotation studies.

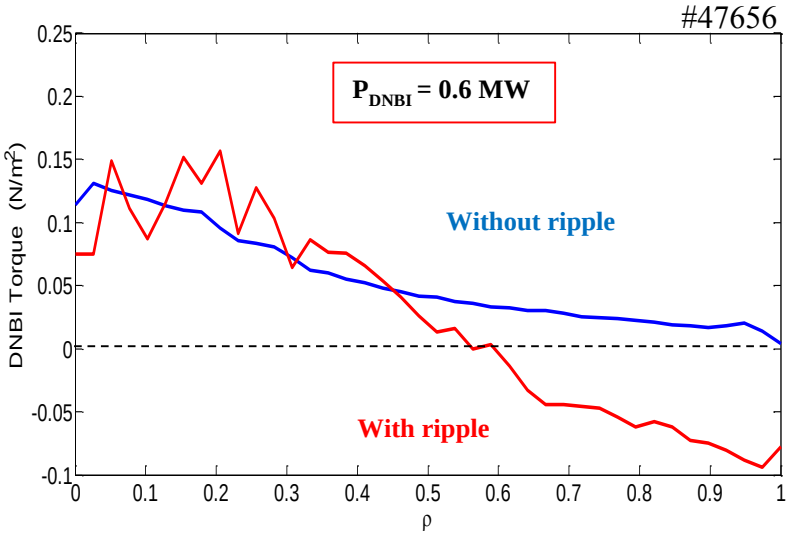

Figure 3.32. *Torque due to the NBI (P_{DNBI} = 0.6 MW, t_{DNBI} = 220 ms) calculated from SPOT with and without ripple contribution. The counter-current torque contribution from the ripple induced fast ion losses (related to the fast ions generated during the DNBI) cancels the beam co-current torque. The total torque is dominated by the collisional torque in the center, hence, it is not affected by ripple.*

Spectrometer characteristics and detector

The spectrometer and associated optical sub-system layout is well illustrated in Figure 3.33. The fifteen 1mm diameter Si-Si fibres (N.A. = 0.22, f/2, clad diameter 1.1mm, core diameter 1.0mm) collecting the plasma charge exchange emission light are coupled to the spectrometer through an injector, consisting of an optical lens group that matches the fibre array to the CCD camera size. The spectrometer entrance slit system consists of a set of curved slits with different widths, the slit curvatures aiming to compensate distortion effects. The whole set is laser engraved on a single metallic foil that is held between two glass strips and can translate vertically.

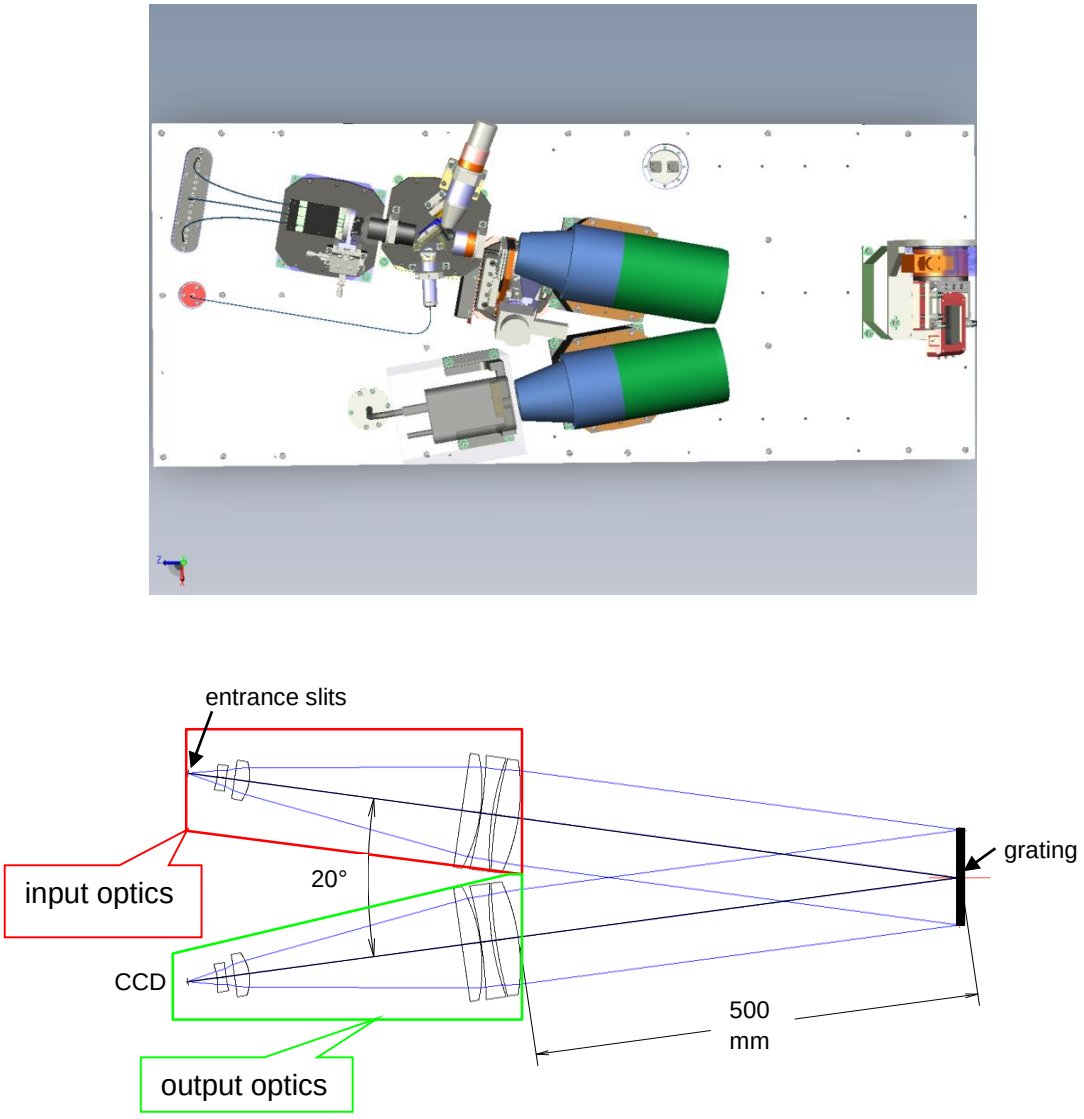

Figure 3.33. *Spectrometer design concept showing the injector, spectrometer, optical groups and CCD camera and schematic view of the two main lens groups and the grating.*

The light is then transmitted to a CCD camera through a high throughput spectrometer (F=328 mm, f/2.8) with dioptric optics, a symmetrical optical configuration, a standard holographic plane grating (135×110×25mm) used in Littrow configuration (improving the transmission). The input and output lens groups consist of one doublet and one triplet lens each, the total optical aberration contribution accounting for much less than 1 pixel.

The optical system is optimized for a working wavelength range extending from 5100 to 5500 Å. The dispersion is non-linear and depends on the grating tilt angle. Nevertheless, with the actual CCD camera described below and in the case where the observed wavelength 529 nm is centred on the optical axis, the dispersion can be considered as constant in the field of the imaging area, d_0 = 0.2658 Å/p.

The reference wavelength is from a λ-stabilized laser (532.043 nm), coupled to the injector by a fibre. In order to avoid Speckle noise effects and minimize uncertainties on the reference wavelength position, a simple vibration pump is used. Such a wavelength reference system is critical when using Doppler shifts of spectral lines to measure accurate plasma rotation velocity, and guaranties the wavelength reference to be calculated at each acquisition time.
In order to minimize parasitic light reflection effects, the whole system (injector, spectrometer optical groups, CCD camera) is covered by a cowl. In fact, each sub-system is separately housed, the cowl surfaces being black anodised and glass bead blasted as shown in Figure 3.34.

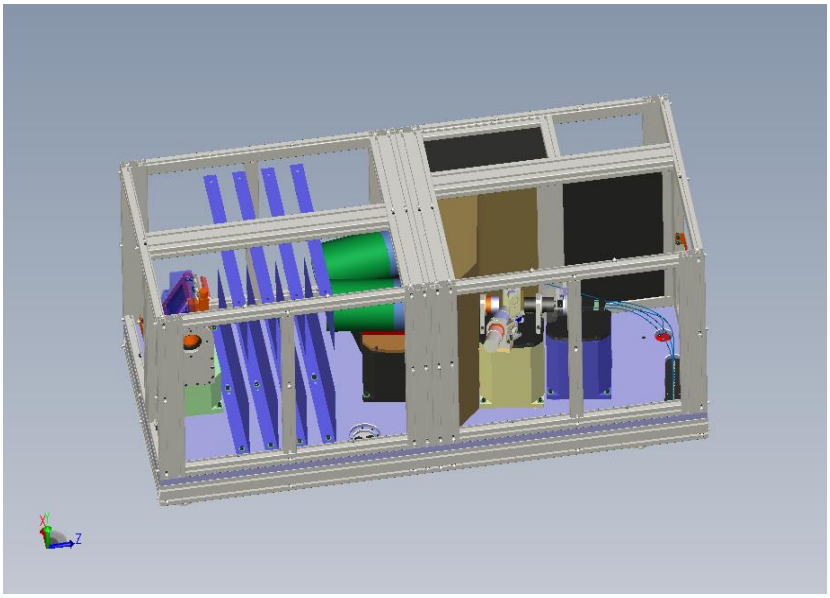

Figure 3.34. *Design concept view of the injector, spectrometer, optical groups and CCD camera covered by a cowl. Each sub-system is separately housed.*

The CCD camera which is being installed, with a thin back-illuminated sensor (e2V), 13.3 × 13.3 mm imaging area, 1024×1024 imaging pixels, 13×13μm pixels, and quantum efficiency ~ 90% at 500 nm. With on chip binning, the minimum exposure time during plasma operation will be 10 ms.

Wavelength calibration

The output spectra from the camera give the intensity per pixel, not per wavelength. To convert the pixels to wavelength a wavelength calibration is needed. To achieve this, we use a wavelength calibration lamp that emits a spectrum of which the wavelengths are well documented. This lamp is usually the Ne lamp where a quadruplet in the visible range

(λ=540.056-534.328-534.109-533.078 nm) is used for calibration and the dispersion calculation. The calibration is realised when the Tore Supra vessel is accessible, during the shutdowns. The calibration lamp is put close to the optical fibres to recover the calibration spectrum. Each pixel therefore corresponds to a certain wavelength.
For the intensity calibration (absolute) a black body containing a white integrating sphere (LabSphère) is used. The intensity of light emitted by the sphere is known. The optical fibres are backlighted, the intensity measured by the camera is then compared to the integrating sphere. The position of the grating is adjusted to the carbon VI λ=529.0 nm (slit 9) and argon XVIII λ=522.3 nm (slit 2). The sensitivity of the fibres is than deduced. Finally the noise due to the parasite light of each line of sight for different exposition times is calculated.

3.4.6. Spectral analysis software (CXSFIT)

To deal with the complex measured spectra, a multi-Gaussian fit software (CXSFIT) is used. The complete documentation can be found in (A.D. Whiteford et al., 2007). Each spectrum consists of passive and active component combination as shown in Figure 3.27. The former component is mainly due to low ionization stage radiation emission from a narrow plasma layer close to the plasma boundary. The active component is due to local emission from the so-called “active volume”, which is defined by the intersection of the neutral beam and the viewing-line path, hence allowing for spatially resolved measurements.

The method to subtract the passive emission is the modeling of this passive spectrum using the temperature and the intensity of the plasma edge. The laser line was also modelled in order to take it into account as a reference line.

The modulation method is also used in order to compare the results. The results given by the two methods are coherent in terms of amplitude and direction.
For the measurements to be discussed here, statistical errors of less than 1.5 km/s for V_φ and less than 50 eV for T_i were obtained.

Co- and Counter- direction conventions in Tore Supra:

The convention for radial, poloidal and toroidal orientation in Tore Supra is presented in Figure 3.35. The configuration of the toroidal magnetic field and plasma current are also shown. The definition of co-current and counter-current rotation orientations are indicated.

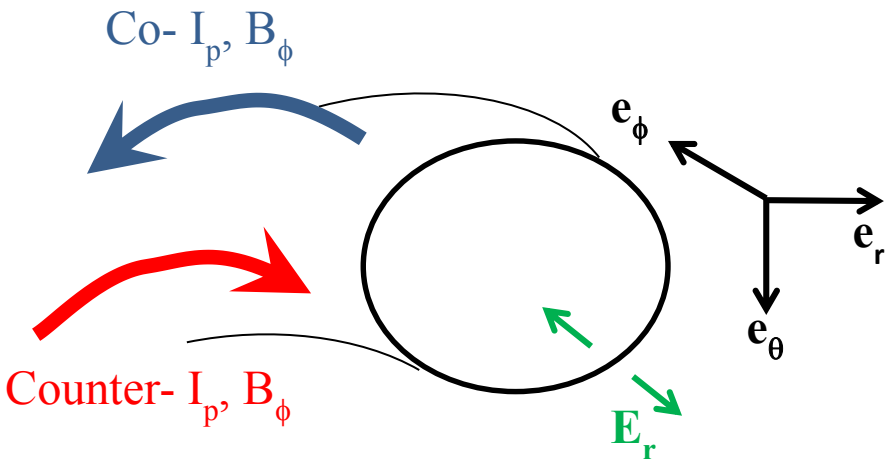

Figure 3.35. *Convention for radial, poloidal and toroidal orientations in Tore Supra. The configuration of the toroidal magnetic field, plasma current are illustrated. One can also see the definition of the co-rotation (positive) and counter-rotation (negative).*

3.5. Summary

In this chapter, a concise description of the Tore Supra tokamak has been presented. The additional heating systems available in Tore Supra and the main diagnostics used to measure the plasma parameters have also been introduced. Due to the importance of the charge exchange recombination spectroscopy, a detailed description has been done. The main conclusions concerning this diagnostic are summarized below:

- The light emitted by the fully stripped impurities when receiving an electron from a neutral particle e.g. the charge exchange reaction is analysed by this technique.
- The charge exchange spectrum consists of an active CX component, due to the neutral beam, passive CX emission and impurity emission from the edge. The pertinent component is the active one. To analyse the active spectrum, we have to filter the passive and the impurity contributions to the spectrum. This can be done by the beam modulation technique or modelling the passive and the impurity emissions.
- Zeeman splitting and l-state mixing are causes of non-thermal broadening of the CX spectrum. To surmount this, the ideal CX spectrum has to be convoluted with a Gaussian of which the width is determined by the Zeeman splitting and l-state mixing.
- The impurity emission located in the same wavelength range of the CX emission but not at the same wavelength position, can be used as a reference line for the wavelength calibration.

- The continuum radiation in the plasma is Bremsstrahlung. For large machines with high density like ITER, the Bremsstrahlung is very high. Hence, a high enough active CX signal is necessary to analyse the spectrum.
- The CXRS installed in Tore Supra is capable of measuring the ion temperature and the toroidal rotation. It uses a diagnostic neutral beam DNBI, for the neutral particle source, with low energy. The spectrometer consists of fifteen viewing lines sweeping all the minor radius of the plasma. The time resolution of the system is between 10 ms and 30 ms. To get very accurate measurements, the system uses a laser as a reference line for the Doppler shift. The inaccuracies of the system give rise to systematic errors and therefore do not influence the gradients and the time evolutions of the measurements.

Although not detailed here, it is worth mentioning that other techniques exist for toroidal rotation measurements:

- X-ray imaging crystal spectroscopy, which is a passive technique based on X-ray emission analysis of heavy ions. This system is foreseen for WEST (C. Fenzi et al., 2013).
- MHD fluctuation measurements: using the relation between the plasma velocity and the MHD frequency, the measurement of the frequency of these MHD fluctuations (density and temperature) with reflectometry or ECE can be converted to the plasma velocity.

IV

Measurement of plasma toroidal rotation during LH and ICRF heating

L'esprit scientifique nous interdit d'avoir une opinion sur des questions que nous ne comprenons pas, sur des questions que nous ne savons pas formuler clairement. Avant tout il faut savoir poser des problèmes.

Gaston Bachelard : La Formation de l'esprit scientifique (1938).

Experimental observations realized on different machines such as JET, C-Mod, EAST and Tore Supra show that plasmas heated with radio frequency waves experience a significant change in terms of intrinsic toroidal rotation, although launched radio frequency waves into the plasma are not expected to drive any significant momentum nor having any effect on the plasma rotation. The differences between those machines are the size, the configuration limiter or divertor, the ripple amplitude and the collisionality regime. JET, C-Mod and EAST are diverted machines while Tore Supra is in the limiter configuration. Unlike the previous machines, the limiter configuration in Tore Supra doesn't allow access to the H-mode. In addition, Tore Supra has an intermediate size between JET and EAST (or C-Mod). C-Mod

operates at high density of the order of $10^{20}/m^3$, while Tore Supra, JET and EAST are less collisional machines. Finally, Tore Supra presents the highest ripple amplitude, around 5% at the plasma boundary. However, despite those differences between these machines, similarities in toroidal rotation behaviour will be identified in the experimental observations.

The main goals of this chapter are, first, to analyse the intrinsic toroidal rotation behaviour during RF heating in Tore Supra, in particular during the LHCD (section 4.1) and ICRH (section 4.2) schemes. A discussion of the results will be led at the end of each section. Secondly, compare the results with those of other machines. Finally, a summary of intrinsic plasma rotation evolution and conclusions is given in section 4.3.

4.1. Toroidal plasma rotation observations during LHCD

The steady-state operation of tokamak fusion reactor requires non-inductive current drive (CD) methods to sustain the toroidal plasma current, in addition to the self-generated bootstrap current. Consequently, extensive work has been carried out to understand the physical mechanisms at play in order to perform predictive simulations of LHCD scenarios. In this context, understanding rotation with LHCD is of prime interest. LHCD-driven rotation has been reported so far in C-Mod (Y.A Podpaly et al., 2011; J. Rice et al., 2009; J.E. Rice et al., 2013), EAST (Y.Shi et al., 2011), JET (L-G. Eriksson et al., 2009), JT60U (Y.Sakamoto et al., 2006) and Tore Supra (P.Platz et al., 1995; C. Fenzi et al., 2011). Co-current (i.e. in the parallel direction to the plasma current, $\Delta V_\varphi > 0$) increments of toroidal rotation have been observed in most of those devices. However in C-Mod, both co- and counter-current (i.e. in the direction anti-parallel to the plasma current, $\Delta V_\varphi < 0$) rotation increments have been reported. Interestingly, counter-current rotation increments have been found to occur in the high plasma current configuration only, above a plasma current threshold $I_{p,threshold}$ = 0.4-0.6 MA depending on the magnetic configuration (lower single null versus upper single null) (Y.A Podpaly et al., 2011). In this section, we analyse dedicated experiments performed in Tore Supra, aiming at clarifying intrinsic rotation behaviour at low I_p (Tore Supra operates at low plasma current ~0.7MA during LHCD in standard configuration. Dedicated experiments are therefore realised in order to explore the rotation evolution at high plasma current. This explains partly the fact that the LHCD effect on plasma rotation was not yet observed in Tore Supra), explore the rotation behaviour at high plasma current and better understand the various mechanisms at play. Tore Supra is a well suited device to address those issues, with a LHRF power capability up to 6 MW and no significant external momentum input from DNBI (section 3.4).

More than 50 plasma discharges have been analysed, with lower hybrid power P_{LH} up to 4.8MW, plasma current I_p up to 1.4MA, line integrated density n_l up to 6×10^{19} m^{-2}, and a significant ripple amplitude (up to 5% at the plasma boundary) which makes ripple-induced momentum non-negligible as discussed in section 5.1.C. The parameters of the main analysed LHCD discharges in Tore Supra are presented in Table 4.3.

#	I_p (MA)	P_{LH} (MW)	n_l ($10^{19}m^{-2}$)	B_T (T)
43181	0.5	0	2.4	2.2
43187	0.5	3	2.4	2.2
43192	0.52	2.1	2.4	2.1
43194	0.55	1.6	2.4	2.22
43195	0.55	2.65	2.4	2.24
43196	0.55	1.6	2.4	2.24
43329	0.65	0.6	3.5	3.7
43334	0.6	0	3.5	3.7
45320	1	0	5.1	3.8
46954	1	1	3.8	3.8
46955	1	1.8	4	3.7
47170	1	0	2.4	3.8
47175	1.2	0	4.9	3.78
47176	1.3	0	5.9	3.8
47181	1.2	0	3.5	2.2
47295	0.71	3.9	4.1	3.8
47296	0.71	3	4.4	3.8
47299	0.71	3	4.2	3.8
47300	0.71	3.25	4.35	3.8
47309	71	4	4.35	3.8
47311	0.71	5	4.45	3.8
47312	0.71	0	2.6	3.8
47313	0.71	0	<3.3>	3.8
47323	1	1	5.4	3.78
47324	1	1.55	5.4	3.78
47325	1	1.8	5.4	3.78
47327	1	1.8	5.4	3.78
47328	1	1.8	5.4	3.78
47540	0.45-0.65	0	<3>	3.8
47544	0.5	0	3.6	3.6
47599	0.7	1.9	3.6	3.8
47610	0.71	4.65	4.3	3.8
47649	0.61	0	2.8	3.81
47654	0.91	4.8	4	3.81
47655	0.61-0.82	4.8	4	3.81
47656	1-1.2	4.8	5.1	3.81
47657	1.5	1	5.86	3.81
47663	1.21	4.6	5.5	3.81
47664	1.21	4.5	5.5	3.81
47665	1.2	2-4.6	5.5	3.81
47666	1.3-1.5	4.8	5.6	3.81
47667	0.78	1.0-2	3.8	3.81
47668	0.78	0-0.35-1	3.8	3.81
48094	1.4	0	3.4	3.7

48102	1	0	1-3.7	3.6
48241	0.55	0	6	3.8

Table 4.3. *Parameters of the main Ohmic and LHCD discharges analyzed in Tore Supra.*

The distributions of the discharges as a function of different plasma parameters: plasma current, line averaged electron density, lower hybrid power and toroidal magnetic field are shown in Figure 4.36. The figure shows that the parameters present a large variation on a large interval. It is worth noting that the discharges are selected from different experimental campaigns. Therefore, a representative database for our analysis in Tore Supra is constituted.

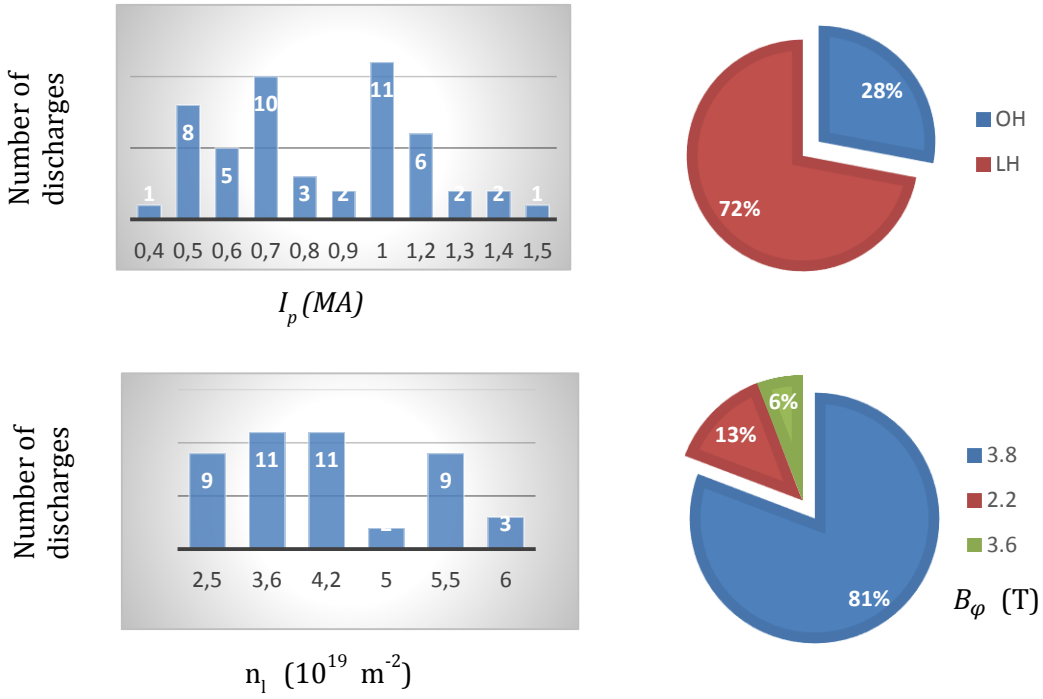

Figure 4.36. *Distribution of the analysed discharges as a fuction of plasma parameters: plasma current (top left), lower hybrid power (top right), line averaged electron density (left) and toroidal magnetic field (right)*

4.1.1. LHCD effect on plasma rotation: parametric analysis

Parametric analyses of plasma rotation as a function of plasma current I_p, LH power amplitude P_{LH} and ripple amplitude δ_a have been carried out in Tore Supra.
Two different effects of LHCD on core plasma rotation were observed. A co-current trend is observed at low I_p and an opposite trend with counter-current change at high I_p. In the following, the two trends are investigated.

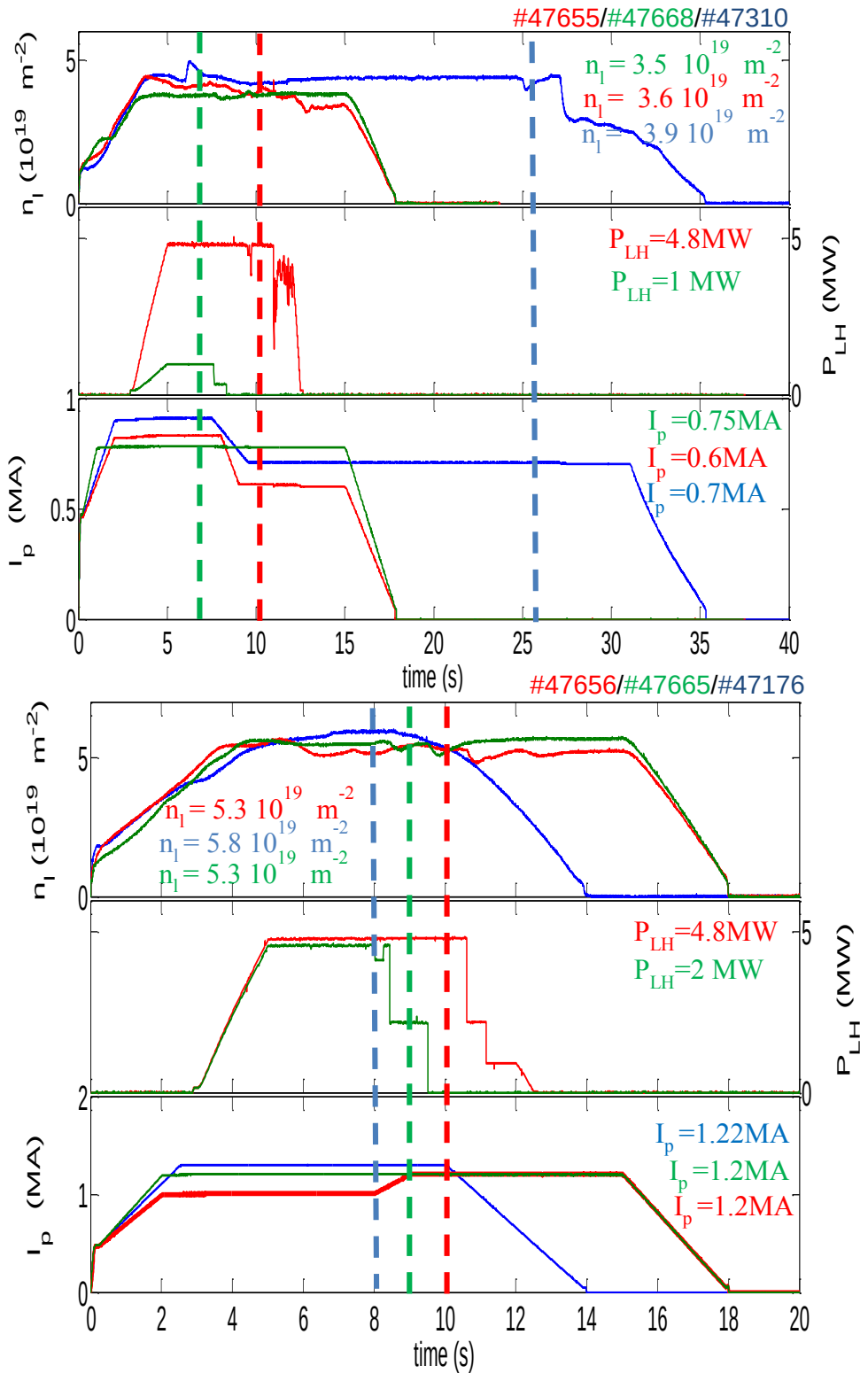

Figure 4.37. *Plasma scenarios for two sets of discharges at low (0.6-0.75 MA) and high (1.2 MA) I_P. The line averaged electron density (top), lower hybrid injected power (middle) and plasma current amplitude (bottom) time-evolution are illustrated for three discharges (one OH and two LHCD) for each figure. The dashed lines represent the times when the rotation profiles are measured.*

According to the Figure 4.40, the plasma rotation behaviour is investigated in two sets of lower hybrid current drive plasma discharges, at high (**>** $I_{p,\ threshold}$) *resp*. low (**<** $I_{p,\ threshold}$) plasma currents, n_l = 5.3-5.8 × 10^{19} m^{-2} *resp*. n_l = 3.5 - 3.9 × 10^{19} m^{-2}, P_{LH} = 1 - 4.8 MW, $n_{//} \sim 1.8$ (maximum $n_{//}$ of the primary lobe in the parallel refractive index spectrum). Ohmic (OH) plasmas with similar plasma parameters are also considered and used as reference plasmas. The scenarios of the two sets of discharges are illustrated in Figure 4.37, showing the time-evolution of the main parameters as line averaged electron density, plasma current and the injected LH power. The plasma current amplitude is fixed to 1.2 MA for the high plasma current set of plasmas and between 0.6 MA and 0.75 MA for the low plasma current set of plasmas. We note that the line averaged plasma density presents a slight difference between the discharges. To overcome this difference the corresponding torques are calculated and this point will be discussed below.

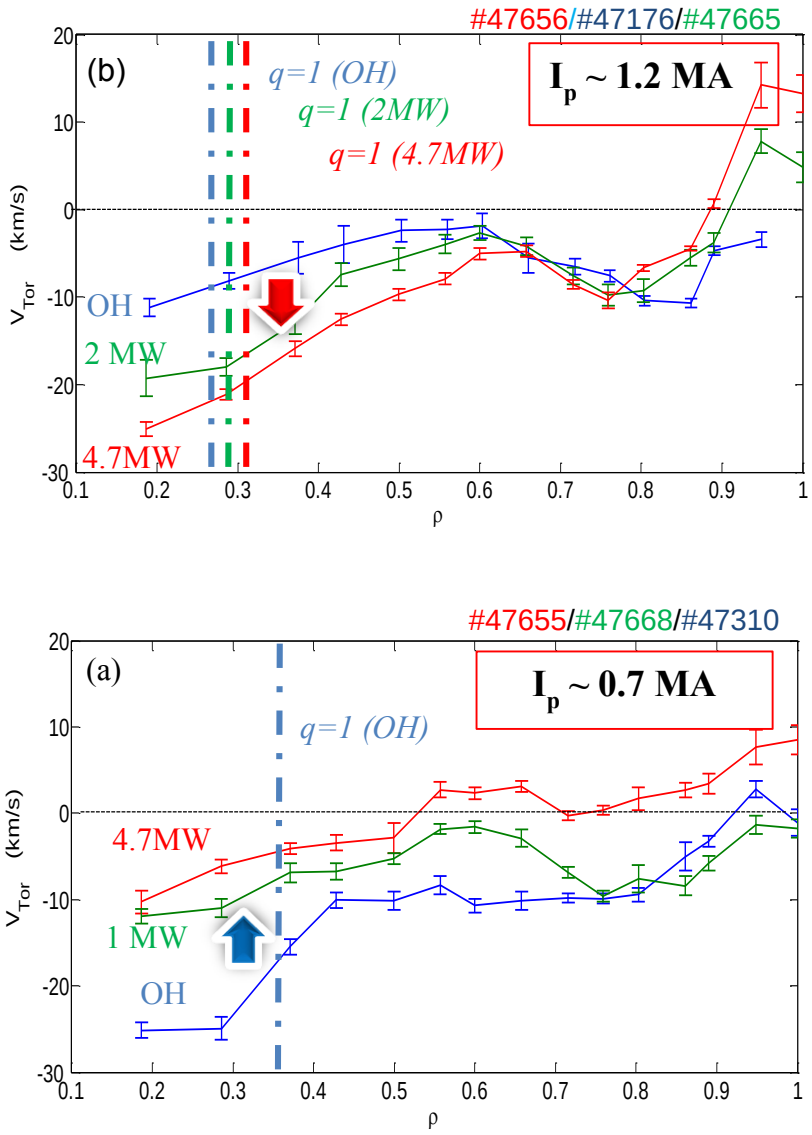

Figure 4.38. *Toroidal rotation profile modifications between ohmic and LHCD plasmas, at low $I_p \sim 0.7$ MA (a) and high plasma current I_p=1.2 MA (b). The q=1 surface locations are also indicated. Co- or counter- current increments are observed depending on the plasma current amplitude. The impact on the plasma rotation increases with the P_{LH} amplitude.*

The measured velocity profiles for these sets of plasmas are reported in Figure 4.38. In LHCD plasmas, significant increments of plasma toroidal rotation are observed in the co- or counter-current directions, depending on the plasma current amplitude.

At low plasma current (0.6-0.75 MA), Figure 4.38a, the velocity profiles are non-monotonic and mainly in counter-current direction. A co-current increment is observed for the LHCD plasmas. This increment increases with the injected LH power amplitude. Also, it is worth mentioning that the effect is visible across the whole plasma minor radius, with a maximum increment of about +15 km/s in the core plasma region (r/a < 0.35). One can also notice, that the plasma core velocity remains in the counter-current direction, while the edge plasma rotation (*r/a* > 0.8) becomes co-current in the highest power case. There is no sawtooth activity in this set of LHCD plasma discharges (according to ECE measurements), and the location of the *q*=1 surface for the OH plasma is also illustrated. The *q* profiles are slightly reversed in the plasma core with q_0 above 1, according to CRONOS (J-F. Artaud et al., 2010) simulations obtained by resolving the current diffusion equation including the current sources and the resistivity (Figure 4.39).

EFIT *q*-profiles (constrained by IR-polarimetry), illustrated in Figure 4.39, are consistent with CRONOS simulations except for the low plasma current case where the reversal was not reproduced (integrated measurements). Note, however that for the ohmic plasma used as reference, sawtooth activity is observed with a sawtooth period of about 30ms and the surface *q*=1 being located at *R* ~ 2.6m (*r/a*~ 0.25-0.3).

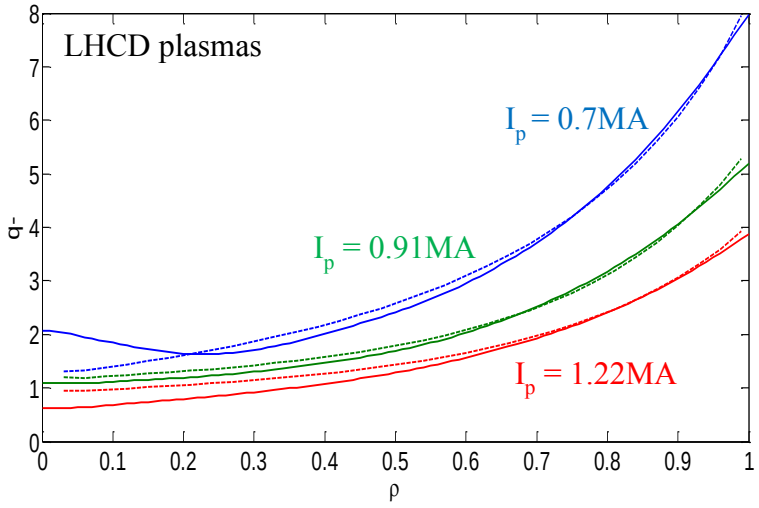

Figure 4.39. *q-profiles from CRONOS current diffusion simulations (solid curves) and EFIT (dashes curves) for high, intermediate and low plasma current discharges during the LHCD phase.*

At high plasma current (~1.2 MA), as illustrated in Figure 4.38b, the velocity profiles are also non-monotonic and in the counter-current direction. An opposite trend is observed with a core plasma rotation increment in the counter-current direction and with a maximum effect of about -15 km/s in the highest LH power plasma. It is worth pointing out in this case that the profile remains unaffected for 0.6 < *r/a* < 0.9. However at the very plasma edge (*r/a* > 0.9), the

velocity increases in the co-current direction with the LH power (similar trend observed in the low plasma current case). This observation could be consistent with the existence of a secondary lobe (in the opposite direction comparing to the primary lobe) in the parallel refractive index spectrum, which would directly transfer momentum to electrons at the plasma edge and could induce co-current rotation as indicated by LUKE simulations (E. Nilsson et al., 2013).
Finally, sawteeth are observed with a period of 50 ms in this set of high plasma current discharges (transition phase in the highest LH power plasma), and the locations of the q=1 surfaces are indicated in the Figure 4.38b. We can see that the LHCD effect on rotation profiles extends far beyond the q=1 surface. The related q profiles (EFIT and CRONOS) are monotonic with q_0 slightly below 1 (Figure 4.39).

Figure 4.40 shows the change in the core toroidal rotation ΔV_φ (the velocity difference between the LHCD and OH plasmas) as a function of I_p, for plasma discharges with B_T = 3.8 T, n_l ~ 3.8 × 10^{19} m^{-2} and P_{LH} = 4.3 MW (for LHCD plasmas). In order to investigate the core plasma rotation (r/a < 0.35) behaviour, discharges with same parameters but with different plasma currents from 0.6 MA to 1.2 MA, during LHCD are analysed. A zero crossing point in rotation velocity is observed (referred to a stagnation point in (J.E. Rice et al., 2013)), the rotation increment ΔV_φ switching from the co- to counter-current direction when the plasma current increases. The observed zero crossing point (i.e. where the core rotation is not affected by LH injection, so that the velocity change is nearly zero) corresponds to I_p ~ 0.95 MA for the presently discussed range of plasma parameters. We can see also that before the plasma current threshold (I_p ~ 0.95 MA), the induced increment decreases when the plasma current increases, while after the I_p threshold the induced increment increases with the plasma current amplitude.

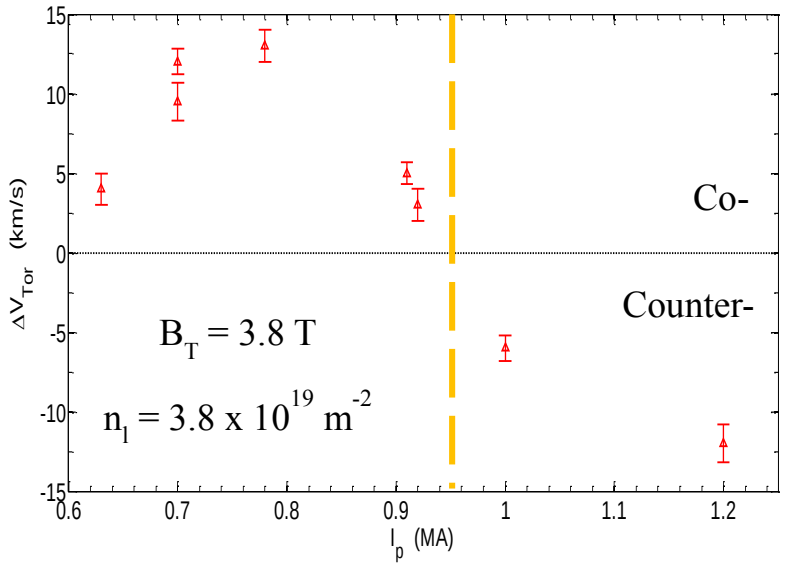

Figure 4.40. *Evolution of the core rotation (0.25<r/a<0.3) change due to LHCD with plasma current amplitude. All data are at fixed density (n_l = 3.8 x 10^{19} m^{-2}) and P_{LH}= 4.3 MW. The vertical line indicates the zero crossing point, for which the plasma current is I_p ~ 0.95 MA. Two different trends can be extracted, co-current effect of LHCD at low I_p and counter-current effect of LHCD at high I_p.*

According to ECE measurements, the sawtooth period is of about 30 ms at low I_p (0.6-0.7MA) and 50 ms at higher I_p for OH plasmas. For the LHCD plasmas, the sawteeth are present only at high plasma current with a period between 30 ms and 60 ms.

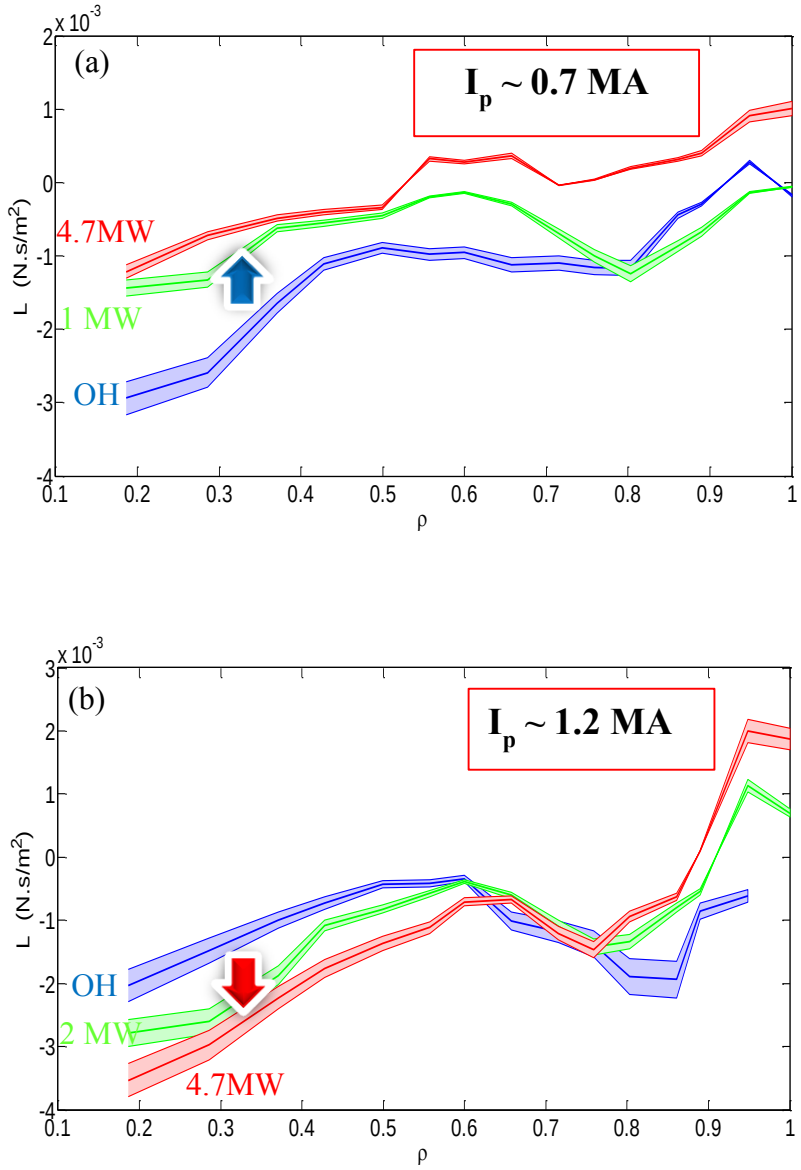

Figure 4.41. *Toroidal angular momentum profile modifications between ohmic and LHCD plasmas, at low Ip~0.7 MA (a) and high plasma current Ip~1.2 MA (b). Similar trends are observed when comparing to the rotation profiles.*

As mentioned above, there is however a slight difference in n_l for the analysed discharges that must be discussed. The density effect on plasma rotation was already reported in C-Mod (J.E. Rice et al., 2011) and TCV (B.P. Duval et al., 2008) where a reversal in toroidal rotation has been observed. This rotation reversal has been linked to the transition from the Linear Ohmic Confinement (LOC) regime to the Saturated Ohmic Confinement (SOC) regime. However, in Tore Supra, the analysis of the density regimes shows that for the densities considered in our analyses, the plasmas are all in the SOC regime (J. Bernardo et al., 2013).
Despite the slight differences in line averaged electron density between the analysed plasmas, the LHCD effects are confirmed and remain strong when considering the total angular momentum *L* evolution with P_{LH}, reading as $L \sim m_i n_i < R^2 > V_\varphi / R$ (where m_i is the main impurity mass, *R* is the plasma major radius and brackets indicate flux average) and the mass effect on toroidal rotation is negligible.
The Figure 4.41 shows the angular momentum profiles for OH and LHCD plasmas at low (Figure 4.41a) and high (Figure 4.41b) plasma current. The precedent approximation of the total angular momentum *L* derives from $L = m_i n_i < R V_\varphi^q >$. Assuming that $V_\varphi^q = \omega_\varphi R + u_\theta F / R$ where ω_φ is the toroidal angular frequency, u_θ the poloidal velocity, *F* is the diamagnetic function and *q* refers to the flux surface, neglecting the poloidal velocity and taking $\omega_\varphi = V_\varphi / R$, one can obtain that $L \sim m_i n_i < R^2 > V_\varphi / R$ (P. Helander and D.J. Sigmar, 2002). We can then, state that the observed effect on plasma rotation is due to the LHCD and not to the plasma density differences (mass effect).

Further information on plasma rotation behaviour can also be obtained comparing plasma rotation profiles ($V_\varphi\ (\rho)$) of an additional set of plasma discharges in the LHCD scenario with similar LH power and n_l, but different I_p amplitudes. The Figure 4.42 represents the plasma scenarios of the set of the discharges at different plasma current amplitudes. We note also a slight difference in line averaged electron density for one discharge, nevertheless, the analysis of the total angular momentum *L* for each discharge, will allow us to overcome this difference. The Figure 4.43 shows the LHCD rotation profiles at different plasma current amplitudes from 0.6MA to 1.2MA. This analysis is different from that in Figure 4.40 which shows the rotation increments (ΔV_φ) as a function of plasma current.
The measured rotation profiles are in the counter-current direction over the whole plasma radius. The rotation ($|V_\varphi|$) increases with I_p in the bulk plasma region up to $r/a < 0.8$, with a maximum increment of about -15 km/s in the core. The impact of the plasma current amplitude is corroborated when considering the total angular momentum *L* evolution with the plasma current effect, as illustrated in Figure 4.44 which represents the angular momentum profiles at different plasma current amplitudes. We can state also here that the observed change in LHCD rotation profiles is due to the change of plasma current amplitude.

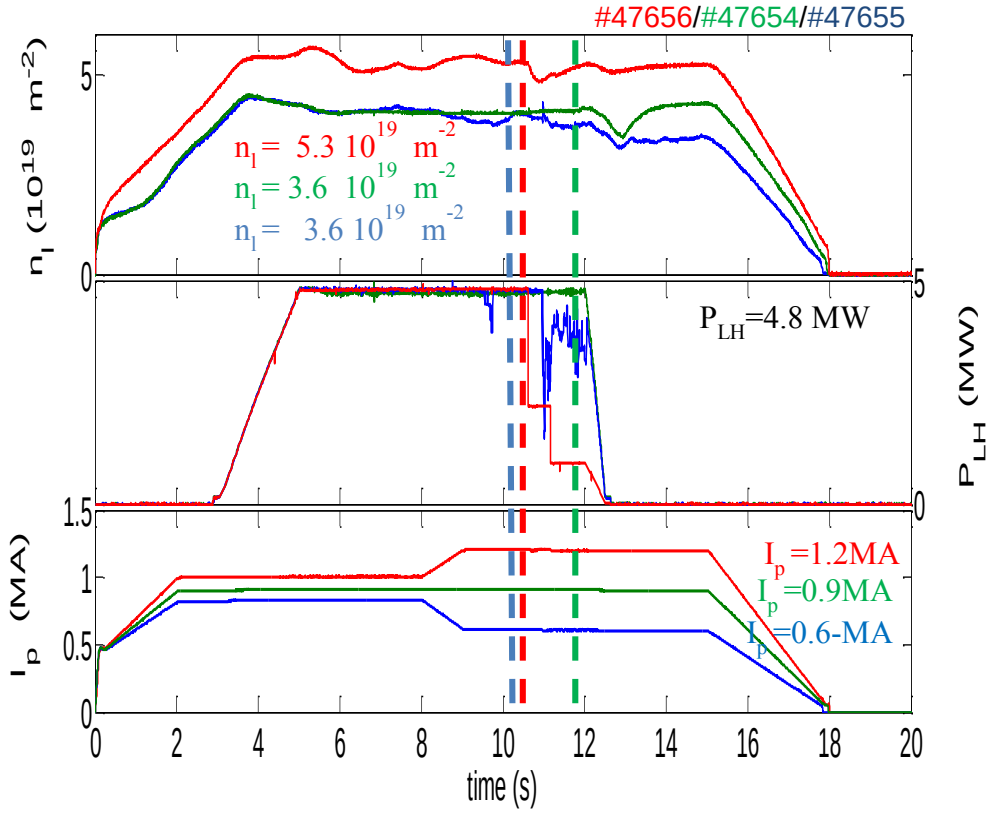

Figure 4.42. *Plasma scenarios for three LHCD discharges at low (0.6 MA), intermediate (0.9 MA) and high (1.2 MA) I_P. The line averaged electron density (top), lower hybrid injected power (middle) and plasma current amplitude (bottom) evolution are exhibited. The dashed line represents the time when the rotation profiles are calculated.*

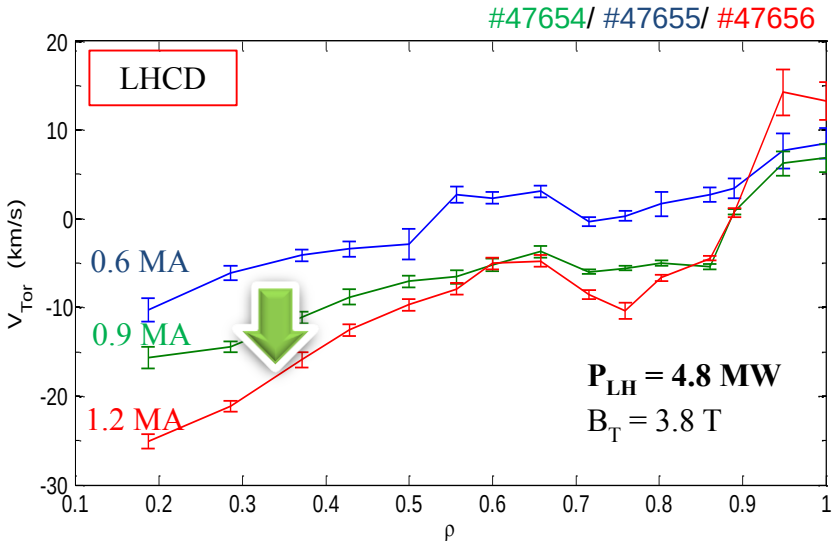

Figure 4.43. *Toroidal rotation profile modifications with I_p for LHCD plasma at P_{LH}=4.8, B_T=3.8 and n_l = 4-5 x 10^{19} m^{-2}. Counter-current increment is observed when I_p increases.*

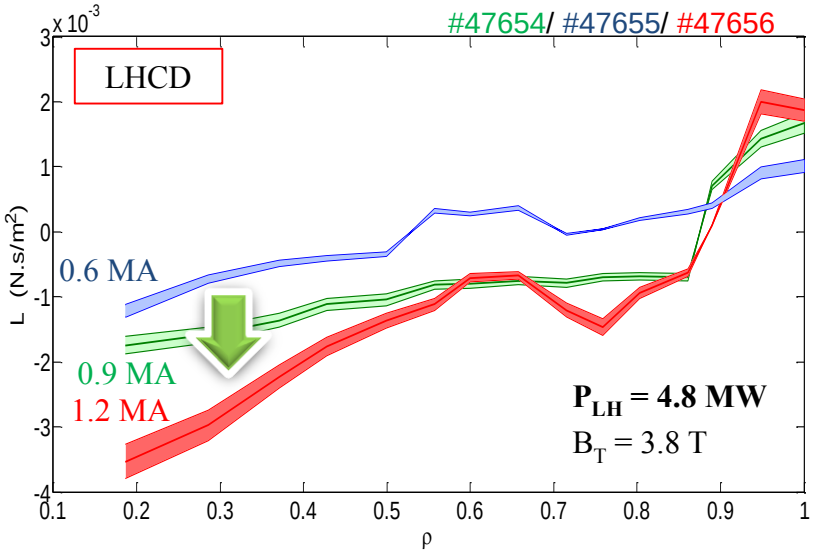

Figure 4.44. *Angular momentum profile evolution with Ip (b) for LHCD plasmas. The observed trend confirms the impact of the plasma current on the LHCD toroidal rotation.*

The ripple strength effect on plasma rotation cannot be ruled out for our analysis, because of the high ripple amplitude in Tore Supra (>5% at the plasma boundary). Hence, it is interesting to study the toroidal rotation evolution at different ripple amplitudes by changing the minor radius of the plasma. To investigate this effect, we focus on toroidal rotation profiles during LHCD with different ripple amplitudes. We know that during the LHCD, fast electrons are generated, and adding to the fact that the locally trapped particle mechanism is dominant for the energetic particles, we can state that the ripple effect during LHCD is due to the fast electron ripple losses.

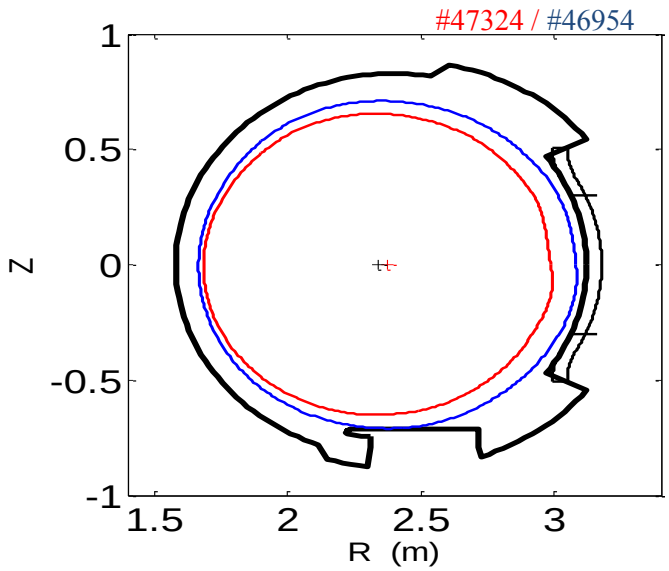

Figure 4.45. *Poloidal cross section showing the plasma boundary for typical plasma discharge (red) and small plasma (blue).*

Shown in Figure 4.45, is the poloidal cross section of two LHCD discharges with different boundary conditions. The discharges present different minor radius a =0.72 m vs a =0.65 m and have different ripple amplitude at the plasma edge δ =5.5% vs δ =3%. The ripple amplitude profiles of the two discharges are shown in Figure 4.46.

The Figure 4.47 shows the plasma rotation profiles of the two LHCD plasmas at fixed line average electron density n_l =5.4 × 10^{19} m^{-2}, I_p =1 MA and P_{LH} =1.8 MW but different ripple amplitudes. The rotation profiles are non-monotonic and in the counter-current direction ($\boldsymbol{V_\varphi} < \mathbf{0}$). A deceleration ($\Delta\boldsymbol{V_\varphi} > \mathbf{0}$) of the core plasma rotation is observed for normalized radius 0.35 < r/a < 0.7 with maximum of ~8 km/s at r/a ~0.55. In the central plasma region, the CXRS lines of sight were not available or not exploitable for the standard plasma (a =0.72 m) discharge.

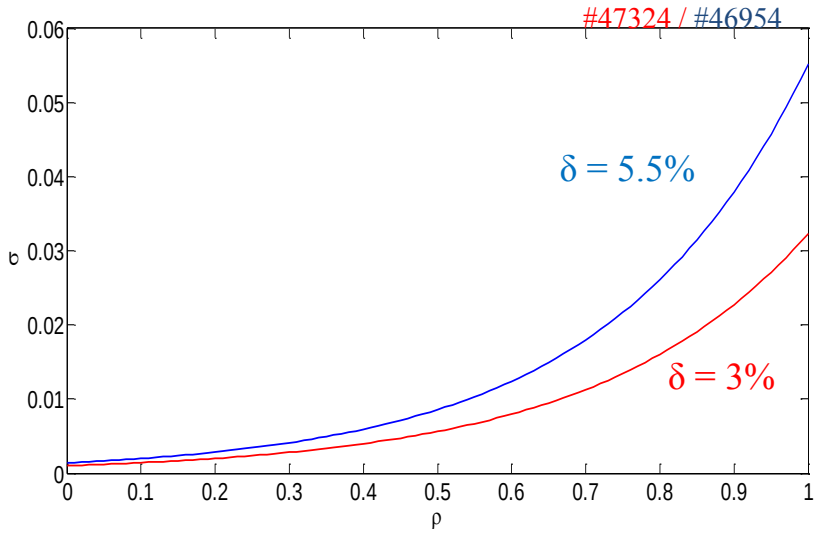

Figure 4.46. *Ripple amplitude profiles in Tore Supra for two plasmas with different boundary conditions. The minor radius for the two plasmas are respectively a=0.65m and a=0.72m.*

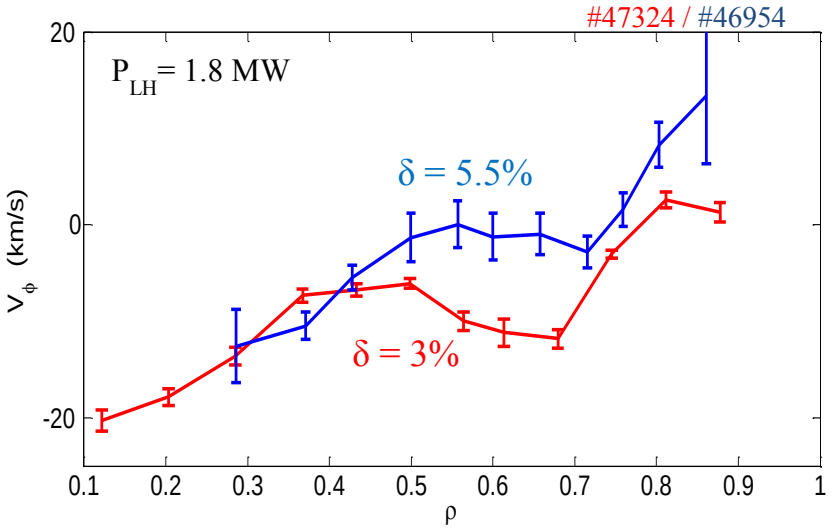

Figure 4.47. *Toroidal plasma rotation from CXRS measurements for typical Tore Supra discharge (δ=5%) and small plasma discharge a=0.65m (δ=2%). Co-current increment is observed due to the ripple strength.*

In this experiment the fast electron ripple effect is highlighted and a clear co-current rotation increment due to the increase of fast electron losses is observed.

4.1.2. Summary

In this first section, a parametric analysis of plasma current, LH injected power and ripple amplitude effects is completed and the experimental results can be summarized as follows:

- The impact of the LHCD on the plasma rotation is strongly dependent on the plasma current amplitude, with co-current increment at low I_p and counter-change at high I_p. To explain these observations the complex interaction of the different mechanisms contributing to the momentum balance equation were investigated and will be presented in the next chapter.
- The increments switch from co- to counter-current at I_p threshold of ~ 0.95 MA.
- The effect of the LHCD on plasma rotation is linearly dependent on injected LH power amplitude.
- The ripple amplitude during the LHCD has a co-current effect on the toroidal plasma rotation.
- The parametric analysis of plasma rotation as a function of electron density during the LHCD was not investigated, and dedicated experiments are necessary, since the data were not available. Nevertheless, the electron density regime effect is investigated for ohmic plasmas in Tore Supra and a rotation reversal which occurs at the transition from LOC to SOC regime was reported in (J. Bernardo et al., 2013).

4.1.3. *Dynamics and time characteristics of toroidal rotation during LHCD*

In order to identify the time characteristics of the rotation changes during the LHCD phase and have indications about the characteristics of the mechanisms behind it, the dynamics of toroidal rotation is analysed. The Figure 4.48 shows the time histories of several parameters of interest for a 3.8 T, 0.7 MA deuterium discharge where 4.8 MW of LH power was injected into the plasma between 3 and 27.7 s. The line averaged density held constant at n_l = 4.8 × 10^{19} m^{-2}. The change in toroidal rotation is analysed during the ramp down phase of the injected LH power (i.e. final phase of the LHCD scenario), which corresponds to the period when DNBI is applied.

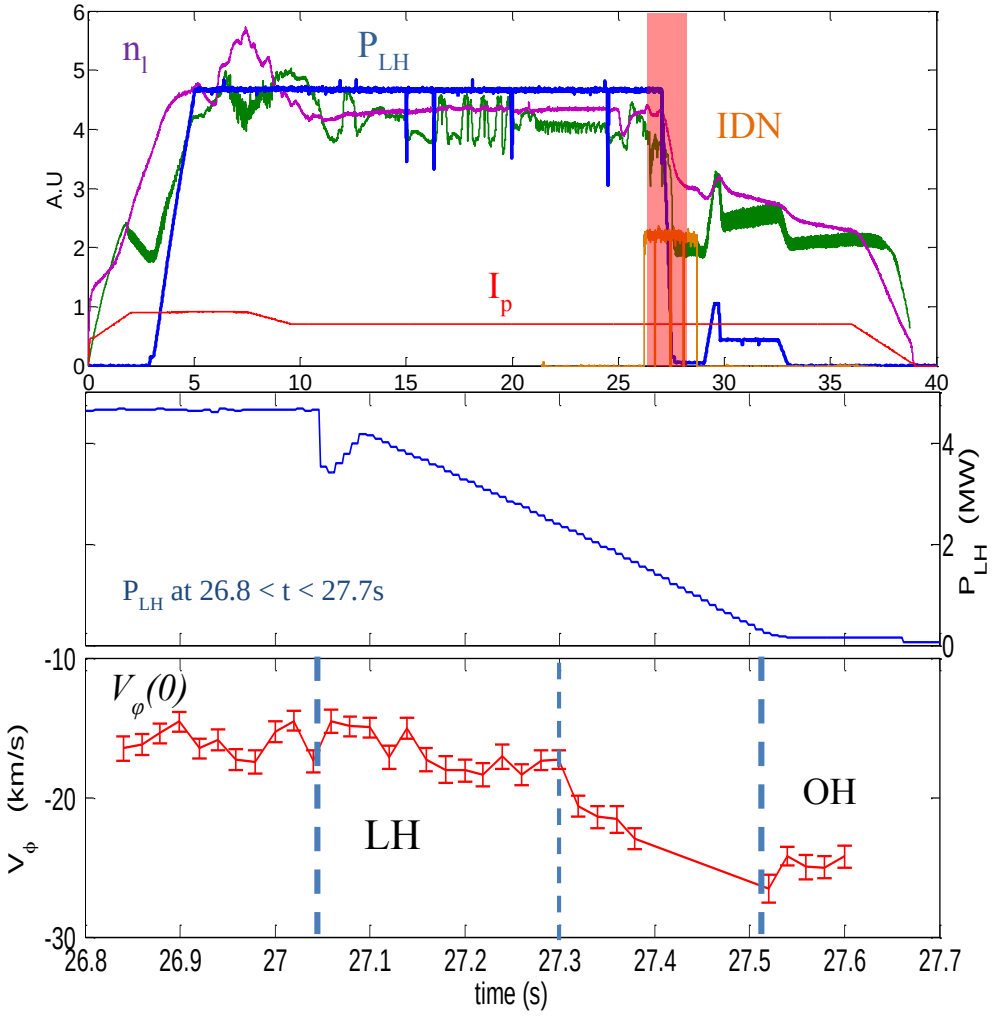

Figure 4.48. *Time histories of the line averaged electron density, LH power (MW), plasma current (MA), DNBI (a.u), electron temperature (keV) and core toroidal rotation velocity (km/s) focused on the LH rump down during the DNBI. The toroidal rotation change is in co-current direction going from ohmic to LH phase. The dashed lines represent the steps of the change in rotation during the LH power switch off.*

There is a simultaneous change in the core toroidal rotation velocity, incrementing in the counter-current direction from -16 km/s to -27 km/s during the transition from LHCD to OH phase, which confirms the co-current trend observed at low plasma current (when we go from OH to LHCD phase). The time scales of the rotation variations are of the order of few hundreds of milliseconds. The plasma response to the LH power switch off with significant change of toroidal rotation (27.3 s) is of the order of ~200 *ms*. The first preliminary conclusion is that the toroidal rotation evolves in time scales longer than the energy and momentum confinement times (~ few tens of milliseconds). This time scale is of the order of magnitude of the current diffusion time which consolidates the role of the current profile and the *q*-profile. Those observations need to be confirmed with high resolution (<10 *ms*) CXRS toroidal velocity measurements during the ramp up phase of the LH power injection scenario. Unfortunately, these data were not available in Tore Supra and would be investigated during the next campaigns.

4.1.4. Sawtooth effect on plasma rotation

As illustrated in Figure 4.38, the analysed discharges present a sawtooth activity with an average period of 50 ms and of *q*=1 surface located in the plasma core around *r/a*=0.3. Therefore, the possible effect of sawtooth activity on toroidal rotation cannot be ruled out for the trends described above. Indeed, the evolution of these sawtooth parameters during LHCD is not significant and the effect remains localised to the core while the rotation change is seen far beyond the *q*=1 surface.

Co-current accelerations of plasma rotation of about +6 km/s have been already reported during sawtooth crashes on TCV (B P. Duval et al.) inside the *q*=1 surface and an opposite effect outside and recently, new results on TCV show a larger increment in toroidal rotation of about 20 km/s (C. Marini et al., 2014) beyond the plasma mixing effect. In the present analysis, the CXRS measurements have been performed with time resolution set between 10 and 20 *ms*, for an ohmic plasma. This allows us to resolve changes in the toroidal rotation across a canonical sawtooth, as shown in Figure 4.49. The rotation behaviour trend seems to be similar to TCV: a co-current acceleration *resp*. counter-current acceleration of core rotation velocity V_φ *(~0)* of about +/-7 km/s is observed at the sawtooth crash inside *resp*. outside (up to *r/a*=0.4) the *q*=1 surface, followed by a velocity relaxation within a time scale lower than 10 *ms* until the next sawtooth event (we can note however that the behaviour is not clear at time 5.68 s). The core ion temperature experiences changes after the sawtooth crash as shown in Figure 4.50 and these modifications are clearly visible at time 5.73 s.

As stated in (R-J. Hastie et al., 1998; Ya. Kolesnichenko et al., 2000), this sawtooth effect can be due to momentum mixing and particle redistribution during the magnetic reconnections after the sawtooth crash (plasma mixing). Indeed, after the sawtooth crash a flattening of the rotation profile is observed (similar to the effect on the electron temperature profile according to Kadomtsev model). For a counter-current rotation profile, this flattening effect likely corresponds to a counter-current increment outside the q=1 surface and a co-current increment inside, which is consistent with our observations of the sawtooth effect. Notice however, that this effect is rather weak in the present experimental measurements and is therefore not clearly visible after all sawteeth (cf. time=5.68s on Figure 4.49). Another signature of the impact of the sawtooth crash could be given by a sharp increase of the toroidal electric

field E_φ. However, this effect is expected to be very localized in time (μs) and in space (around the q=1 surface), which makes it hard to capture experimentally. A similar behaviour can be expected when considering LHCD plasmas case. In our experiments, the q=1 surface is slightly shifted outwards (from r/a~0.25 to r/a~0.3) with LH heating and Ip increase (see Figure 4.38), hence remaining localized in the plasma core region. Also, Figure 4.38 and Figure 4.49 shows that the time-average impact of the sawtooth activity on core plasma rotation profile appears to be rather weak, and localized to the q=1 surface. Hence any attempts to correlate the LH heating effects on rotation profiles with the change of sawtooth characteristics in the LHCD phase or their suppression don't yield any tangible results, as also reported in JET (L-G. Eriksson et al., 2009; Ya. Kolesnichenko et al., 2000).

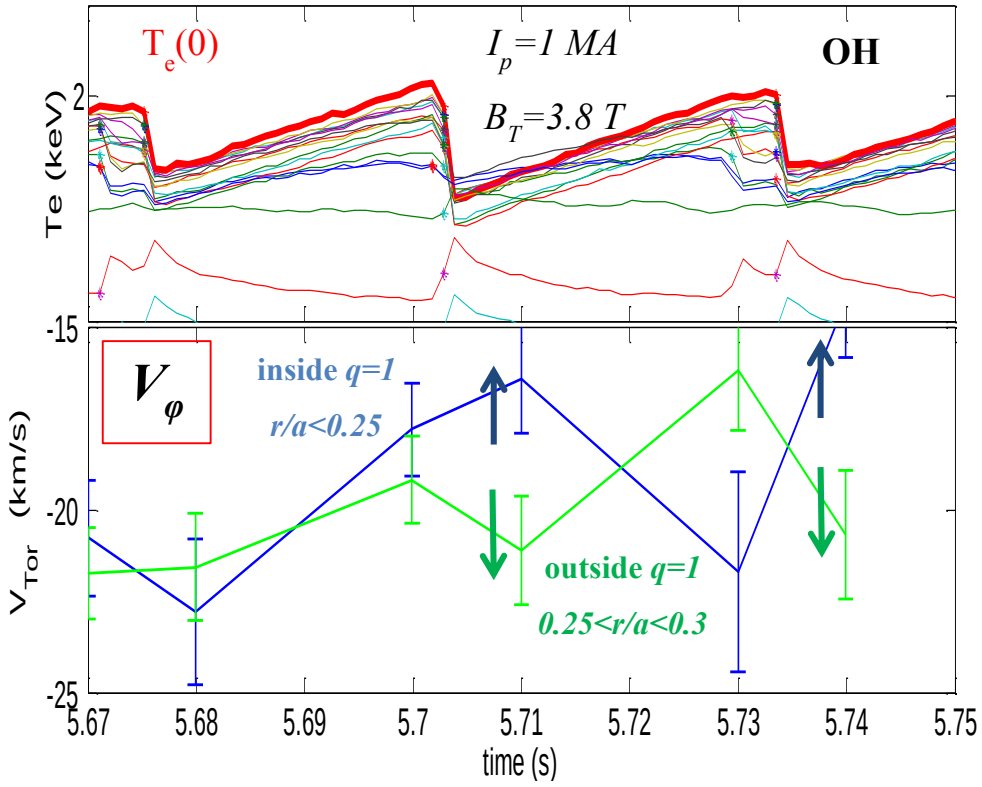

Figure 4.49. *Time evolution of the electron temperature (top) and of the toroidal core plasma rotation velocity (bottom) for 3.8T, 1MA ohmic discharge. The sharp drops of the central temperature are triggered by sawteeth.*

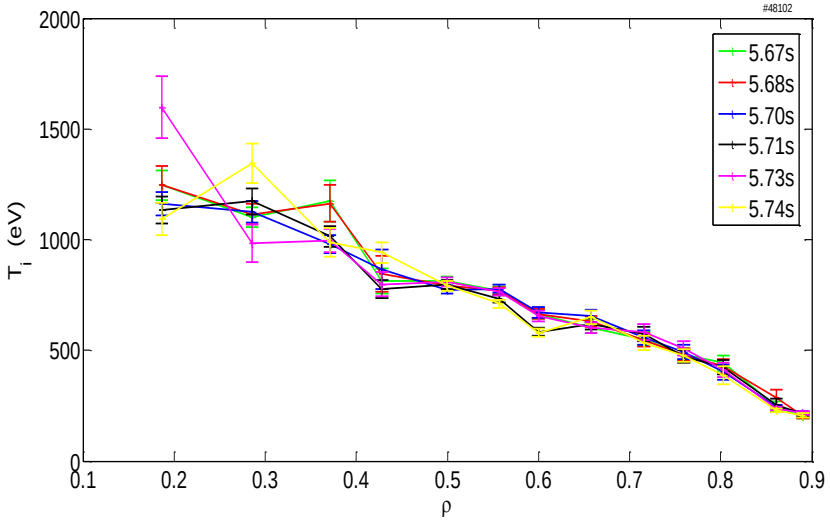

Figure 4.50. *Ion temperature profiles during the sawtooth events. The profile modifications (~100eV) observed in the core plasma are due to the plasma mixing after the sawtooth crash*

4.2. Toroidal plasma rotation observations during ICRF heating

In the previous section, we observed that the lower hybrid current drive has a significant impact on the toroidal plasma rotation. In this section, the evolution of the plasma rotation profile during ion cyclotron resonance heating is analysed.

Rotation with ICRH has already been observed in several machines such as JET, C-Mod and Tore Supra where the core averaged toroidal rotation was measured by the X-ray Bragg crystal spectrometer (P. Platz et al., 1999). Co-current toroidal rotation is observed in JET (L-G. Eriksson et al., 2009) and C-Mod (J.E. Rice et al.), while in Tore Supra both co- and counter-current rotation increments have been reported (L-G. Eriksson et al., 2001).

In this section, the database of ICRH discharges will be revisited and ICRH rotation profiles will be analysed using charge exchange recombination spectroscopy (CXRS) spatially resolved measurements. Rotation profiles are therefore investigated to improve understanding of the mechanisms involved during the ICRF heating. This analysis also aims to confirm or not the previous results of the core averaged rotation measurements performed in Tore Supra with ICRH.

The parameter details of the analysed Tore Supra discharges are summarised in the Table 4.4.

#	I_p (MA)	P_{ICRH} (MW)	n_l ($10^{19}m^{-2}$)	B_T (T)
45445	1.4	4.4	8.3	3.8
45446	1.2	4.6	7.8	3.8
45449	1.2	4.8	7.8	3.8
45450	1.2	4.8	7.8	3.8

47300	0.72	3	4.4	3.8
47344	1	3.8	8.5	3.8
47399	1	5.8	5	3.8
47491	0.75	2.5	6.2	3.8
47496	0.75	4.3	5.8	3.8
47499	1.2	1.9	6.75	3.8
47500	1.2	2	7	3.8
47505	0.72	2	5.8	3.8
48195	1.2	4	6	3.8

Table 4.4. *Parameters of the main ICRH discharges analyzed in Tore Supra.*

4.2.1. Change in toroidal rotation during ICRH

In Tore Supra, ICRF heated plasma discharges with symmetric antenna spectra have in the past few years been observed to accelerate the plasma toroidally, both in the co- and counter-current directions. In particular, there was evidence that co-current acceleration of plasma core rotation occurred during hydrogen minority heating n_H/n_D, with a fairly high concentration of minority ions and during the ^{3}He minority heating. In lower minority concentration discharges, counter-current acceleration was observed. Different mechanisms affected by the minority concentration have been suggested, in particular the transferred fraction of the ICRH power to the plasma bulk and the level of supra-thermic ripple ion losses (L-G. Eriksson et al., 2001; S. Assas et al., 2003).

In order to better understand the previous observations, further investigate the mechanisms at play and improve our approach of ICRH induced rotation in Tore Supra, ICRH toroidal rotation is explored for different minority heating concentrations, with charge exchange recombination spectroscopy.

Two sets of ICRF heated plasmas, at high (7%) *resp*. low (3%) minority concentration n_H/n_D, n_l = 5.8 - 6 × 10^{19} m^{-2} *resp*. n_l = 3.5 - 3.9 × 10^{19} m^{-2}, P_{ICRH} = 1 - 4.3 MW and plasma current I_p ~ 1.2 MA are investigated. Ohmic plasma rotation profiles from the OH phase of the highest P_{ICRH} discharges are considered and used as reference plasmas. The minority concentrations are measured with the fast neutral analyser diagnostic.

The Figure 4.51 shows a set of ICRH low minority concentration (3%) discharges at 1.2 MA, B_T=3.8T and n_l = 5.8 - 6 × 10^{19} m^{-2}. A small difference in electron density is observed when the rotation profiles are calculated. The ohmic and 4.3 MW ICRH rotation profiles are measured from the same discharge.

The Figure 4.52 shows a significant increment of plasma toroidal rotation in the counter-current direction.

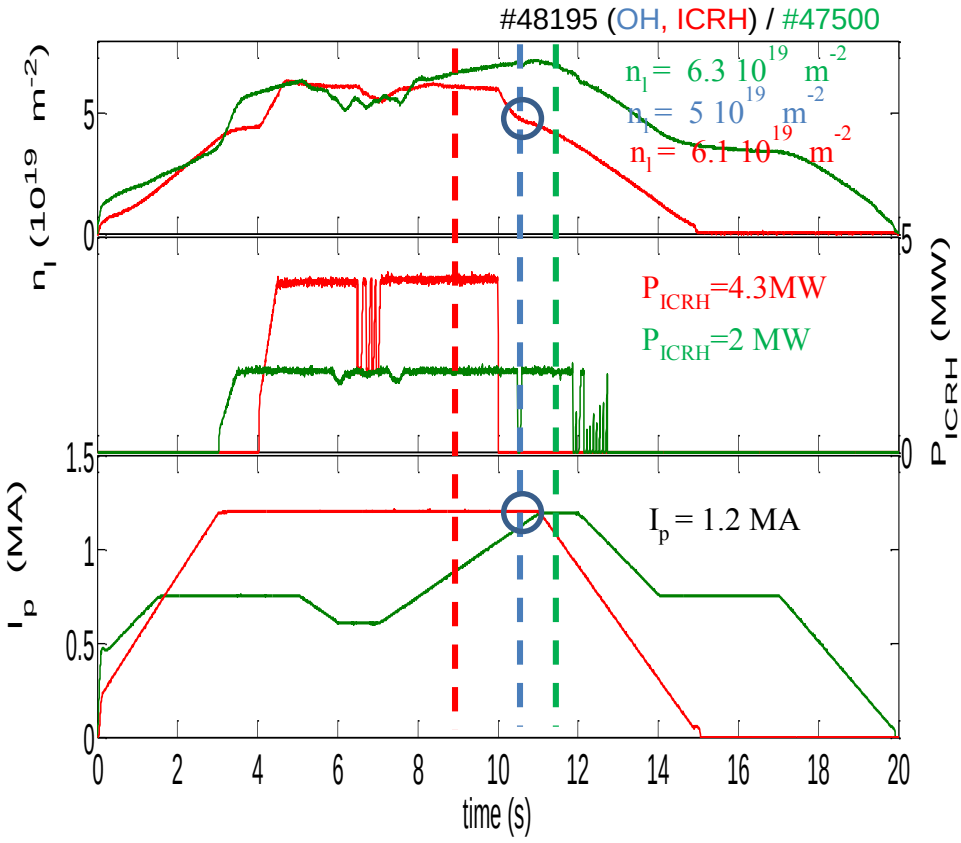

Figure 4.51. *Plasma scenario for a set of discharges at low* n_H/n_D *and at 1.2 MA. The line averaged electron density (top), ICRH power (middle) and plasma current amplitude (bottom) evolution are illustrated for three discharges (one OH and two ICRH). The ohmic and high* P_{ICRH} *cases rotation profiles are measured from the same discharge. The dashed lines represent the times when the rotation profiles are calculated.*

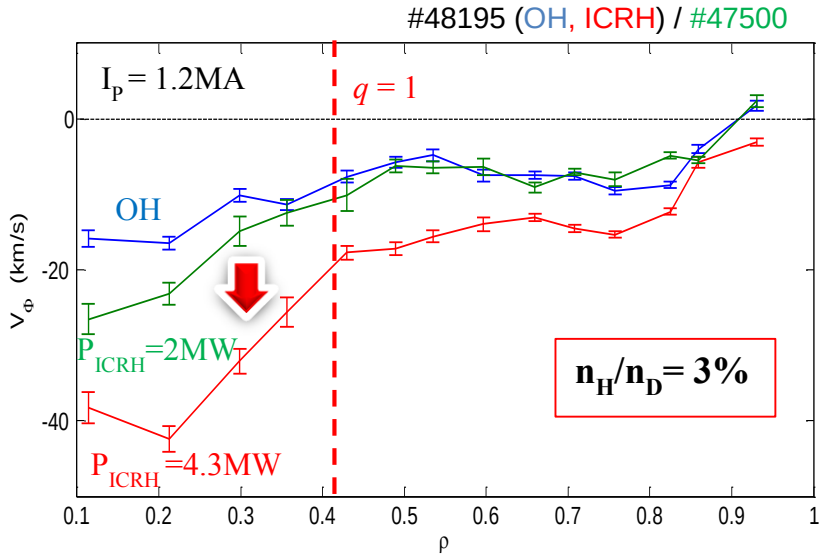

Figure 4.52. *Toroidal rotation profile modifications at low minority heating between ohmic and ICRH plasmas, at* I_p*=1.2 MA. The dashed line represents the q=1 surface which is approximately the same for the two discharges.*

The ohmic profile is relatively flat and in the counter-current direction ($V_\varphi < 0$). During ICRH, the core plasma rotation increments in the counter-current direction with a maximum of about -25 km/s for the highest power case. It is worth pointing out in this case that the profile remains almost unaffected for 0.7 < *r/a* < 0.9. The edge plasma rotation (*r/a* ~ 0.9) is close to zero for the all discharges. Finally, sawteeth are observed in this sets of plasma discharges, and the *q=1* surface location is illustrated in the Figure 4.52. The related *q* profiles (EFIT constrained by polarimetry) calculated for a similar discharge (the profile was not available for the analysed discharges) are presented in Figure 4.53. The profiles are monotonic with q_0 slightly below 1 for the OH and ICRH phases. The sawtooth period is about 60 ms and the surface *q*=1 being located between *r/a*~0.4 and 0.45.

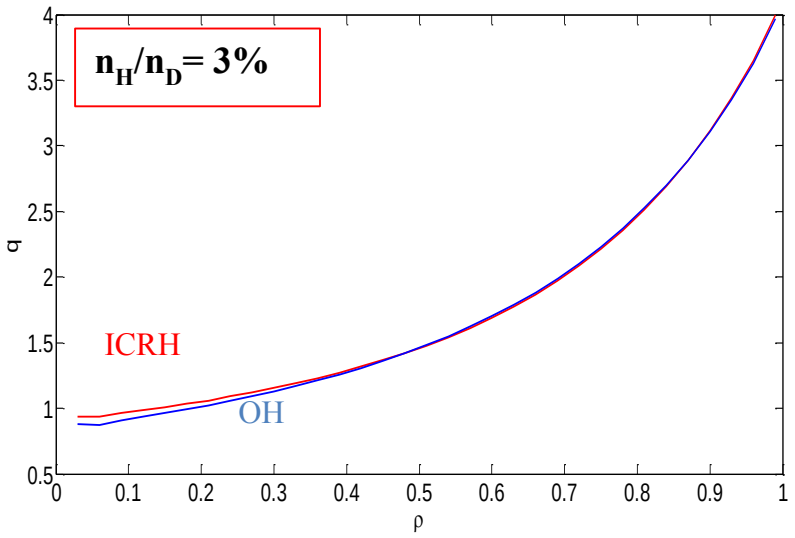

Figure 4.53. *q-profiles from EFIT during the OH and ICRH phases and at low minority concentration. The profiles are monotonic with q_0 slightly below 1in the all cases.*

Figure 4.54 shows the scenarios of two plasmas where we can see the electron temperature, the line averaged electron density, the injected ICRH power and the plasma current. The ICRH plasma was heated with high minority concentration (7%). The line averaged electron density and the plasma current amplitude are a bit different between the two discharges. For the average line density, the estimation of the corresponding angular momenta shows the same trend with a clear co-current effect. The ICRH plasma presents giant sawteeth with period of 350 ms interposed by 100 ms period sawteeth.

An opposite trend compared to the low minority concentration case is observed with co-current rotation increment as illustrated in Figure 4.55. The effect is observed over the whole profile with a maximum of about 10 km/s in the core plasma. The ICRH rotation profile is flat and remains in the counter-current direction.

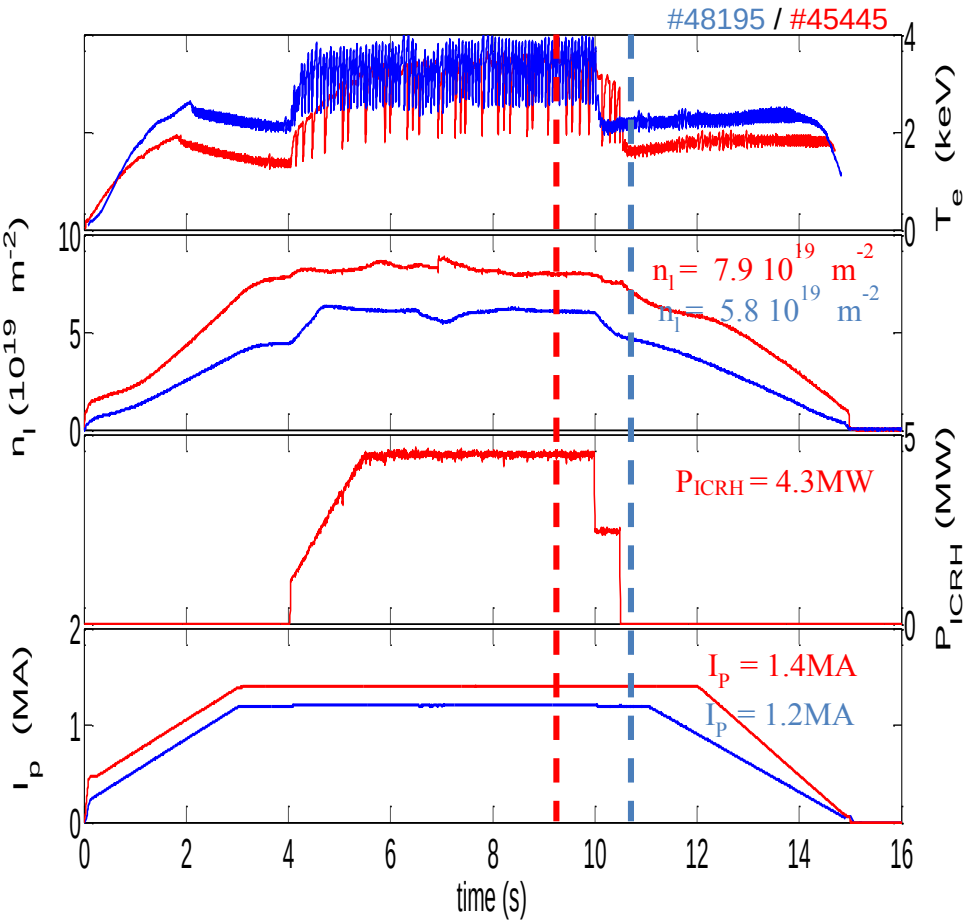

Figure 4.54. *Plasma scenarios for two discharges at high* n_H/n_D. *The core electron temperature and the line averaged electron density (top), ICRH power (middle) and plasma current amplitude (bottom) evolution are exhibited for the two plasmas. The dashed lines represent the times when the rotation profiles are calculated.*

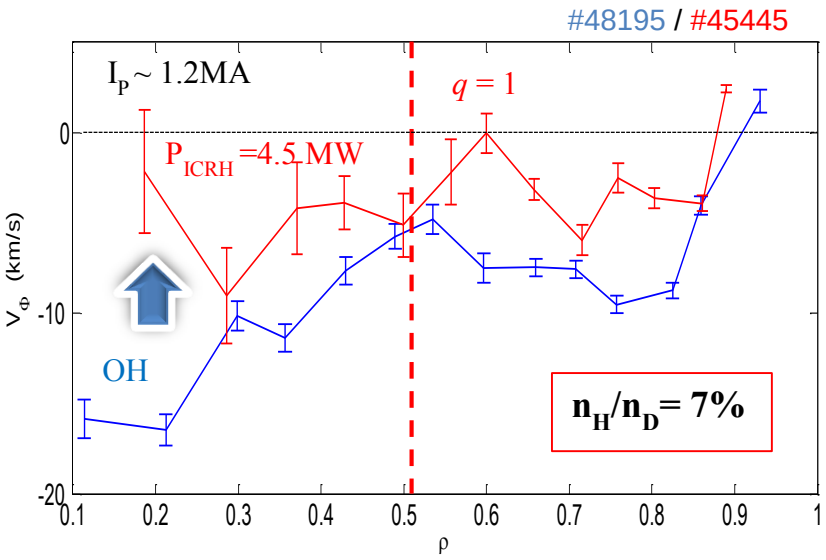

Figure 4.55. *Toroidal rotation profile modifications between ohmic and ICRH plasma, at high plasma minority concentration. A co-current increment is observed over the whole profile. The dashed line represents the q=1 surface.*

The rotation dynamic during the monster sawteeth is analysed, but any clear or tangible trend cannot be extracted. Unfortunately, we didn't dispose of a rich database to achieve statistical analyses of sawteeth or monster sawteeth during ICRH. High resolution measurements are also necessary for this analysis. However, previous analysis shows that the monster sawtooth has a significant effect on toroidal plasma rotation with increments of about 20 km/s (C. Fenzi et al., 2011). This study has to be confirmed.

An interesting observation of the minority concentration amplitude effect on the plasma rotation is shown in Figure 4.56. The figure shows the ICRH rotation profiles with low and high minority concentration. A strong co-current change over the all profile in toroidal rotation with a maximum of about 40 km/s is seen when we go from low minority concentration (3%) to high minority concentration (7%). This observation is consistent with the previous experimental observations, since a counter-current change at low n_H/n_D and a co-current change at high n_H/n_D were observed. Another interesting remark is related to the q = 1 surface shift. Indeed, an outwards shift in the q = 1 surface is noted when the minority concentration amplitude increases. Unfortunately, the q profile of the high minority concentration ICRH plasma was not available for analysis. Also the monster sawteeth are only present at high minority concentration. Dedicated experiments are needed to provide more information on those observations.

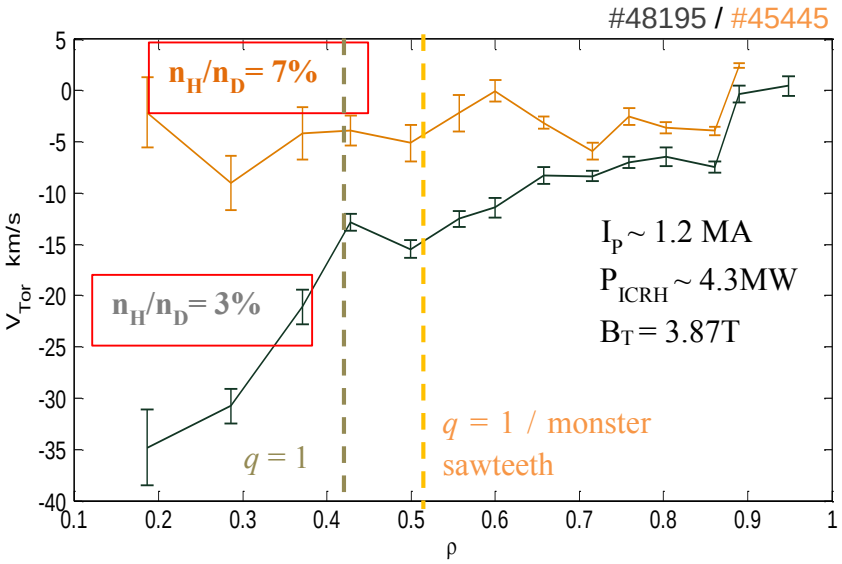

Figure 4.56. *Toroidal rotation profile modifications between low and high minority concentration ICRH plasmas. A co-current increment is observed over the whole profile when* n_H/n_D *increases.*

4.2.2. Summary

In this second section, the toroidal rotation evolution during ICRH was investigated with charge exchange recombination spectroscopy measurements. ICRH plasma rotation profiles with low and high minority concentration were analysed. The main results are summarised as follows:

- The toroidal plasma rotation is observed to change both in the co- and counter-current directions during ICRH.
- Co-current acceleration occurs during hydrogen minority heating, with fairly high concentration of minority ions. In lower minority concentration discharges, counter-current acceleration is observed
- Those results comfort previous observations and provide additional information on rotation profile behaviour (not only central averaged measurements), showing as well that the rotation remains counter-current.

4.2.3. *Dynamics and time characteristics of toroidal rotation during ICRH*

The toroidal rotation evolution is also analysed over an ICRH pulse (when the power is switched off) in order to identify the time characteristics of the rotation changes during the ICRH phase and develop intuition about the involved mechanisms. The Figure 4.57 shows the time histories of several parameters of interest for 3.8 T, 0.7 MA deuterium discharge with low minority heating concentration where 4.3 MW of ICRF power were injected into the plasma between 3 and 13.1 s. The line averaged density held constant at n_l = 5.4 × 10^{19} m^{-2}. The discharge presents sawtooth activity with a period of about of 60 ms. It is important to note that the discharge is at low plasma current.
The change in toroidal rotation is analysed during the ramp down phase of the injected ICRH power (i.e. final phase of the ICRH pulse), which corresponds to the period when the CXRS measurements are available (DNBI pulse).

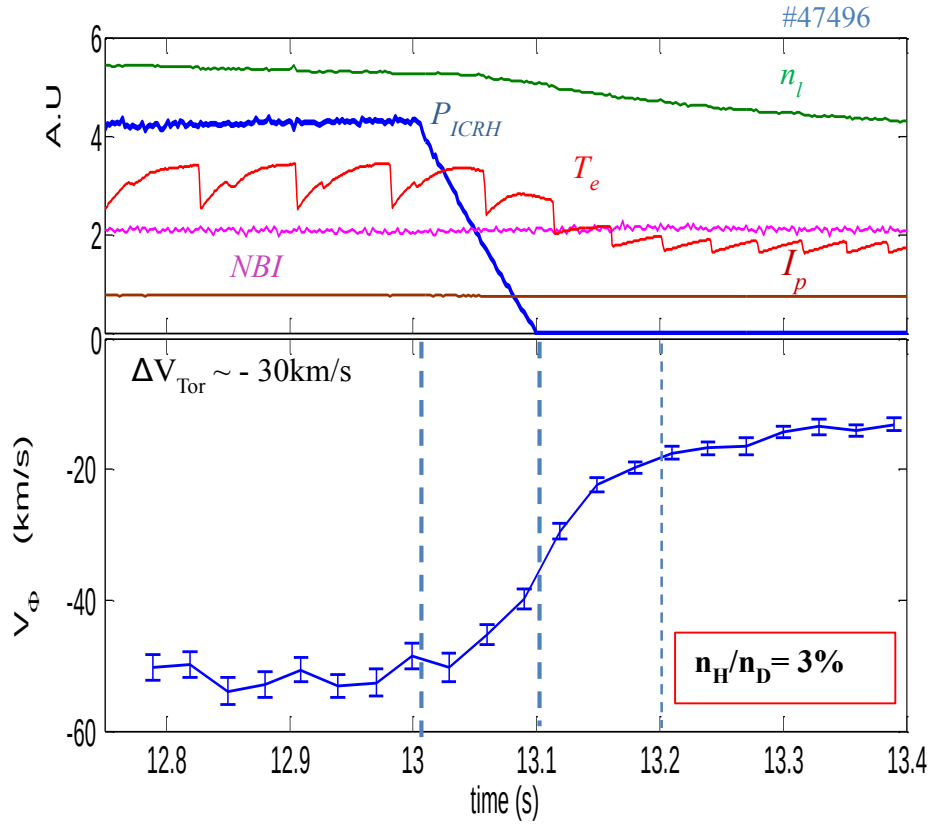

Figure 4.57. *Time histories of the line averaged electron density (*10^{19} m^{-2}*), ICRH power (MW), plasma current (MA), NBI (a.u), electron temperature (keV) and core toroidal rotation velocity (km/s) focused on the ICRH ramp down during the D-NBI scenario. The toroidal rotation change is in the counter current direction when the power is applied.*

The toroidal rotation change is instantaneous and concomitant to the ICRH ramp down with a co-current rotation increment when ICRH is switched off. In the OH phase when the ICRH is totally switched off, the rotation continues to evolve in the co-current direction for a time of about of 100 ms. Hence, the time characteristic of the plasma rotation evolution during ICRH is very fast, of the order of few tens of milliseconds in the first phase and then, the ICRH effect remains present in the plasma for a longer time (hundreds of milliseconds). The conclusion is that at the beginning, the rotation evolution time during ICRH is similar to the momentum confinement time and then become slower in the final phase.
The response of the plasma to the ICRH power injection in terms of rotation is complex and this rotation evolves with different time characteristics. The dynamic is consistent with the counter-current trend observed at low minority heating despite the lower plasma current amplitude. Fast CXRS measurements (< 10ms) and more discharges with ICRH with dedicated experiments in the next campaigns are needed to better investigate this dynamic.

4.3. Conclusions

In summary, we have carried out several experiments in an effort to elucidate the toroidal rotation evolution during the LHCD and ICRH scenarios.

- First, we found that the plasma toroidal rotation profiles (*r/a* up 0.8) of all the analysed discharges are non-monotonic and in the counter-current direction certainly due to the neoclassical friction in the presence of ripple (will be discussed in the next chapter). The edge plasma rotation (*r/a* > 0.8) is in the co-current direction in most of the discharges.
- In the lower hybrid current drive case, we observed a significant change in toroidal rotation compared to the ohmic target plasmas. The change in rotation during the LHCD is strongly dependent on the plasma current amplitude. At low plasma current, a co-current rotation increment is measured over the whole profile with a maximum of +15 km/s in the core plasma. An opposite trend is noted at high I_p in the inner part of the plasma *r/a* up to 0.6 with a maximum counter-current effect of about -15 km/s. The plasma current value where the trend switches from co- to counter-current increment is identified at 0.95 MA for the analysed plasma parameters. An interesting behaviour of counter-current rotation change of LHCD plasmas with plasma current amplitude is also reported.
- The dynamics studies of plasma rotation during LHCD show that the time characteristics of the rotation evolution are of the order of few hundreds of milliseconds which are longer than the momentum confinement time.
- Those new results of toroidal rotation with LHCD are consistent with C-Mod. For JET and EAST, only the co-current trend has been reported.
- Previous core toroidal rotation measurements with an X-ray crystal spectroscopy (heavy impurities in the plasma) (P.Platz et al., 1995) show a similar behaviour of toroidal rotation during LHCD, but this effect was not explored. The Figure 4.58 represents the rotation increments of core toroidal rotation during LHCD at low and high plasma current. In both cases, co-current acceleration is observed in the plasma core. Nevertheless, at high I_p the co-current increment tends to zero and becomes

slightly counter-current in one discharge. This seems to be consistent with our observations.

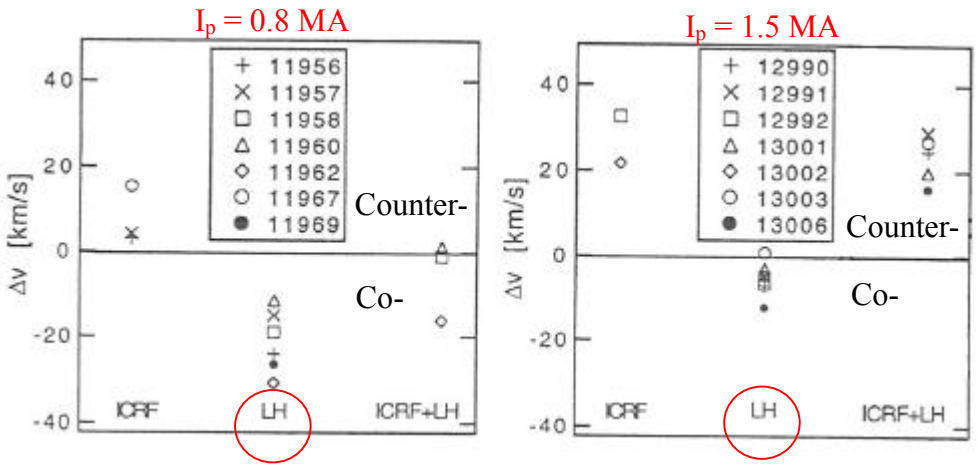

Figure 4.58. *Change in core toroidal plasma rotation due to the LHCD measured by the X-ray crystal spectrometer at low and high plasma current. In this configuration, ΔV>0 resp. ΔV<0 means in the counter- current resp. co-current direction. Large co-current effect during LHCD is observed at low plasma current only* **(P.Platz et al., 1995)**.

- For the ion cyclotron resonance heating scenario, a clear change in toroidal rotation is observed as well. In this case, the key parameter is the minority heating concentration amplitude. At low minority concentration (3%), a counter-current rotation increment is seen over the whole profile with a maximum effect of about ~25 km/s, while at high minority concentration (7%) a co-current increment of about 10 km/s is observed for the whole profile as well. The analysis of the rotation evolution allows us only to state that the time characteristics of the plasma rotation during ICRH are complex and characterized by different phases. Our studies of ICRH rotation is consistent with the first experimental results, already obtained for the core averaged toroidal rotation, but also complete those analyses with new results which provided us a better understanding of rotation with ICRH in Tore Supra. Nevertheless, the observed rotation changes at low and high minority heating is different in terms of amplitudes from the previous analysis (S.Assas, 2004; L-G. Eriksson et al., 2001). In our study increments of 25 km/s resp. 10 km/s at low and high minority concentration are observed while in (S.Assas, 2004; L-G. Eriksson et al., 2001) opposite amplitudes with 10 km/s resp. 25 km/s at low and high minority concentration have been reported. It is important to point out that the rotation measurement techniques and the measured impurities are different between the two studies.
- In other machines like C-Mod or JET, only co-current rotation profiles have been reported with ICRH.

The analysed database regroups the experimental campaigns of 2008, 2009, 2010 and 2011. In the next chapter, the theoretical mechanisms behind these experimental observations will be investigated.

Theoretical models for toroidal plasma rotation with LHCD and ICRH

The object of research is no longer the nature itself, but the nature left to human inquiry, and to that extent, man here relates only himself.

Werner Heisenberg

In the previous chapter, experimental observations of toroidal intrinsic rotation with RF heating and current drive were reported in Tore Supra. In particular, two effects on plasma rotation are observed, with co- or counter-current changes depending on key plasma parameters. In LHCD scenarios (section 4.1), the effect on plasma rotation is strongly related to the plasma current amplitude while in the ICRH plasmas (section 4.2), the impact is related to the minority concentration n_H/n_D used for the fundamental minority heating. The plasma current amplitude plays a role in particle and energy confinement and the minority concentration n_H/n_D is known to impact the ICRF heating efficiency and its potential for providing ion heating in the plasma.

In the last few years, intriguing observations of plasmas rotation in both the direction of the plasma current (co-current) and in the opposite direction (counter-current) have been made in radio frequency (RF) heated plasmas with little or no external momentum injection (L-G. Eriksson et al., 1992; A. Scarabosio et al., 2006); this phenomenon is often referred to 'intrinsic' or 'spontaneous' rotation. Intrinsic plasma rotation can be understood as resulting from the competition between several effects: MHD effects (E. Lazzaro et al., 2002), turbulent transport processes (Y. Camenen et al., 2009), fast particle effects (L-G. Eriksson et al., 2001) and 3D effects such as those induced by resonant magnetic field perturbations or ripple (T.E. Stringer et al., 1972; J.D. Callen, 2011). The latter arises from the variation in toroidal magnetic field (TF) magnitude due to the finite number of TF coils. Hence, it is present in all tokamak devices. Most observations in H-mode plasmas have been in the co-current direction, while the trend in L-mode plasmas is still less clear.

The origins of the spontaneous rotation are unfortunately not really understood and it is at present, difficult to predict and develop models of plasma rotation. Different models were already proposed, in order to explain the mechanisms which give rise to intrinsic rotation.

Theories related to the fast accelerated particles (electrons and ions) have been proposed. Counter-current resp. co-current rotation could be due to the loss of fast trapped ions resp. electrons. The finite orbit width effects (F.W. Perkins et al., 2001) and the spatial transport of the resonating ions induce a radial transport of the toroidal angular momentum (the integral of the angular momentum over the plasma is null). The mechanism predicts co- resp. counter-current rotation if the inner lobe of the dipolar torque is in the co-(low field side) resp. counter-current (high field side) direction. This change has not been supported by experimental results (L-G. Eriksson and F. Porcelli, 2002). Another possibility investigated in (L-G. Eriksson and F. Porcelli, 2002) is the wave particle momentum transfer due to the differential absorption of launched power by resonating particles (difference between the positive and the negative toroidal mode numbers). The experimental evidence for ICRH rotation drive where the phasing of the antennas was varied from launching waves propagating predominantly in the direction of the plasma current to counter-current propagating ones show that this effect does not induce a significant change in toroidal rotation (L-G. Eriksson et al., 2004). For LHCD discharges, this wave momentum can be estimated by simulations of the electron distribution function evolution.

Investigations of rotation of bulk plasma and in the ohmic phase are important, since the effects directly related to the heating mechanisms and fast particles do not explain the observed rotation. The neoclassical theory predicts counter-current rotation in the core plasma (M.N. Rosenbluth et al., 1971). For the edge rotation, a co-current rotation is predicted by neoclassical theory in the Pfirsch-Schlüter regime while in the banana regime a counter-current rotation is predicted (A.L. Rogister et al., 2002). Neoclassical effects due to the symmetry breaking with the magnetic field ripple can also influence the plasma rotation. The thermal friction force due to the radial flux generated by banana particles whose banana tips are perturbed by the ripple modulation and also due to the collisions of banana particles with passing ones, is also identified to influence the plasma rotation. Hence, these effects related to ripple are expected to be significant in Tore Supra.

Other mechanisms are offered by the turbulent or anomalous transport which can drive rotation in the plasma. An example is given by the so called accretion theory where the preferential direction of the turbulent modes in the edge of the plasma is invoked to provide a torque on the plasma. It suggests a co-current rotation in H-mode (B. Coppi et al., 2002). Another theory is related to the flow driven in the scrape off layer by ballooning type transport. The effect of this theory on the plasma rotation is dependent of the grad-*B* drift (B. LaBombard et al., 2004).

The $E \times B$ shear in the plasma leads to different pinch terms in the transport equation for the angular momentum (O.D. Gurcan et al., 2007). This pinch term can explain the co-current accelerations observed at the transitions to H-mode. A Coriolis drift effect has also been discussed in (A.G. Peeters, 2007). It acts as a pinch term in toroidal rotation.

In this chapter, a new theoretical approach developed in the framework of this thesis to explain the LHCD induced rotation (section 5.1) is performed. A preliminary theoretical approach of ICRH induced rotation in Tore Supra is also discussed (section 5.2).

5.1. Theoretical models for toroidal rotation during LHCD

For intrinsic toroidal rotation during LHCD, there are few theories or mechanisms invoked to explain the experimental observations, principally in C-Mod, JET and Tore Supra. In C-Mod, the Lorentz force on the bulk electrons which is the plasma response to the resonant electron flows (X. Guan et al., 2013) and the Ware pinch of trapped electrons (Z. Gao and N. J. Fisch, 2011), both induced by lower hybrid waves, are put forward to describe the rotation evolution as a function of plasma current during the LHCD phase. In JET, the momentum absorbed from the directed lower hybrid waves by the resonant electrons, resulting in a torque on the bulk plasma, induces a non-negligible change in toroidal rotation in the counter-current direction (L-G. Eriksson et al., 2009). Finally, in Tore Supra, the change observed in the core rotation in LHCD plasmas with an X-ray crystal spectrometer was believed to be mainly linked to fast electron ripple loss mechanisms (P.Platz et al., 1995; C. Fenzi et al., 2011)**,** because of the presence of a strong ripple (> 5%). However, there is no conclusive and complete theoretical explanation for toroidal rotation during LHCD in those devices taken as a whole. In the following paragraph, the different possible mechanisms of intrinsic rotation will be investigated during LHCD for Tore Supra.

5.1.1. Identification of possible mechanisms contributing to plasma rotation during LHCD

In this section, we present a complete and comprehensive approach to understand intrinsic rotation in the presence of LHCD in Tore Supra, with the identification of the different possible mechanisms at play (neoclassical, turbulent) and the estimation of their impacts on plasma rotation.

The main idea of our approach is as follows: when considering intrinsic rotation, all terms of the momentum balance equation (eq. 2.35) should be analysed in order to predict the toroidal rotation evolution. This equation is rewritten below:

$$n_i m_i \nabla.\left(-\chi_{v\varphi}\nabla_r V_\varphi + v_\varphi V_\varphi + \pi_{RS}\right) = e_i n_i E_\varphi + j_r \times B_\theta - n_i m_i \nu_{neo}\left(V_{i\varphi} - V_T^*\right) + S_{LH} \qquad (5.1)$$

It represents the toroidal momentum balance equation for the main ions, in steady state, during LHCD. It describes the evolution and the distribution of the toroidal plasma rotation. The right hand side contains the different mechanisms which count for the momentum sources with the

Coulomb force $e_i n_i E_\varphi$, the Laplace force $j_r \times B_\theta$, the ripple induced thermal neoclassical friction $-n_i m_i \nu_{neo}\left(V_{i\varphi} - V_T^*\right)$ and the source term S_{LH} due to the electron-LH wave interaction. on the left hand side, the angular momentum transport term with the Reynolds stress is reported.

Intrinsic toroidal velocity results from a competition between turbulent transport processes, magnetic stress due to MHD modes, loss of fast particles and neoclassical ripple viscosity damping. The experimental toroidal rotation observed in Tore Supra (chapter 4) is always in the counter-current direction ($V_\varphi < 0$) which suggests that the plasma rotation could be constrained by the neoclassical toroidal diamagnetic velocity which is negative ($V_{dia} < 0$). The ripple induced neoclassical thermal friction generates a counter-current change in toroidal rotation during LHCD with increments depending on the plasma current. Turbulent momentum transport (Reynolds stress) acts as a decelerating force, where the amplitude of this force depends on the plasma current amplitude and on the heating regime (OH, LHCD). The wave-particle interaction due to the injected LH waves in LHCD regimes acts as a localised source term and accelerates the plasma in the counter-current direction. The examination of the subtle interaction of all the above cited terms and their dependencies on plasma parameters like I_p or heating scheme, is the global method that allowed prediction the intrinsic rotation evolutions during LHCD. The results are then compared with experimental observations of Tore Supra, and put in perspective with other machines**.**

In the following subsections, each mechanism in the toroidal momentum balance equation (eq. 5.1) and their dependencies on plasma parameters will be investigated and estimations of their absolute contributions to the plasma rotation will be calculated.

A. Wave momentum source contribution S_{LH}

In LHCD discharges, where waves at the lower hybrid frequency are launched into the plasma in order to generate toroidal current and control the *q*-profile, a wave-electron interaction takes place and toroidal momentum is transferred to the bulk plasma. The LH waves are directed when penetrating the plasma and therefore drive a finite momentum. The current is carried by electrons and the momentum by ions. Here we show that a substantial momentum is transferred from the accelerated electrons by LH waves to the ions through collisions. The process is similar to the mechanism of the current generation with the only difference that the generated current is destroyed by collisions while the momentum is conserved in the plasma. Also, the impact of this source term (the wave momentum) on the rotation depending on the plasma current is examined. The energy transport of the fast electrons is out of the scope of this paragraph. The momentum in the plasma due to wave-electron interaction was approximately estimated for the first time in JET using an empirical formula (L-G. Eriksson et al., 2009). In Tore Supra numerical simulations performed with LUKE (Y. Peysson and J. Decker, 2014; Y. Peysson et al., 2000) provide the radial profiles of the LH power deposition and the momentum profile absorbed from the LH waves. LUKE is a Fokker Planck solver allowing the resolution of the evolution of the electron distribution function which permits the calculation of the momentum transferred from waves to the plasma.

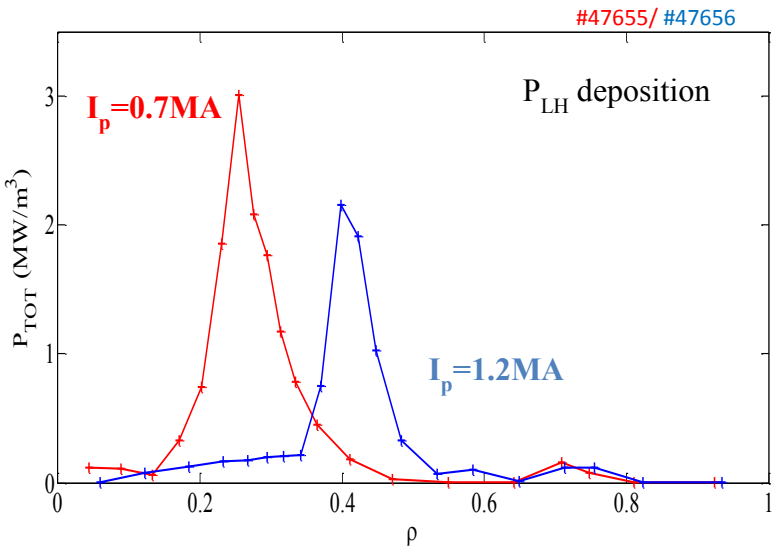

Figure 5.59. *LHCD deposition power profiles calculated by LUKE for two discharges at P_{LH}=4.8MW and Ip=0.7MA (red), Ip=1.2MA (blue). For higher I_p the profile deposition is shifted outwards.*

Shown in Figure 5.59 are the LH power deposition profiles for low (0.7MA) and high (1.2MA) I_p. The maximum deposition location is shifted outwards when the plasma current increases, as usually observed in Tore Supra (Y. Peysson et al., 2000; F. Imbeaux et Y. Peysson et al., 2005).

The corresponding transferred wave-momentum profiles S_{LH} inferred from LUKE simulations are displayed in Figure 5.60. The momentum profiles are off-axis in the counter-current direction, with a maximum transfer of wave momentum S_{LH} of 15 mN/m^3 at r/a ~ 0.3 for low I_p *resp.* 10 mN/m^3 at r/a ~ 0.4 for high I_p. This momentum source is therefore spatially localized in the core plasma region which corresponds to the LH wave deposition region. At the edge (r/a = 0.75) a non-negligible momentum source in the co-current direction is also observed. This is likely due to the existence of the secondary lobe (in the opposite direction compared to the primary lobe) in the parallel refractive index spectrum of the LH antenna (E. Nilsson et al., 2013). In the plasmas analyzed here, no plasma current dependence of the transferred momentum can be found because the higher momentum transfer observed at low I_p in Figure 5.60 is not reproducible. Nonetheless, it is rather strongly related to the LH wave deposition in the plasma which is consistent with Figure 5.59. The induced rotation increments are calculated using the formula of the total momentum stored inside the plasma $S_{LH} = 2V_\varphi m_i n_i / \tau_\phi$, where τ_ϕ (50-100 ms) is the momentum confinement time estimated by the CRONOS code. The expected absolute rotation increment due to this mechanism is about -5 km/s to -8 km/s which is locally significant, but appears to be rather weak when considering the whole rotation profile. In fact, the waves injected in the plasma can be considered as a local source term impacting the intrinsic rotation in the counter-current direction, and does not explain the observed increments over large minor radius.

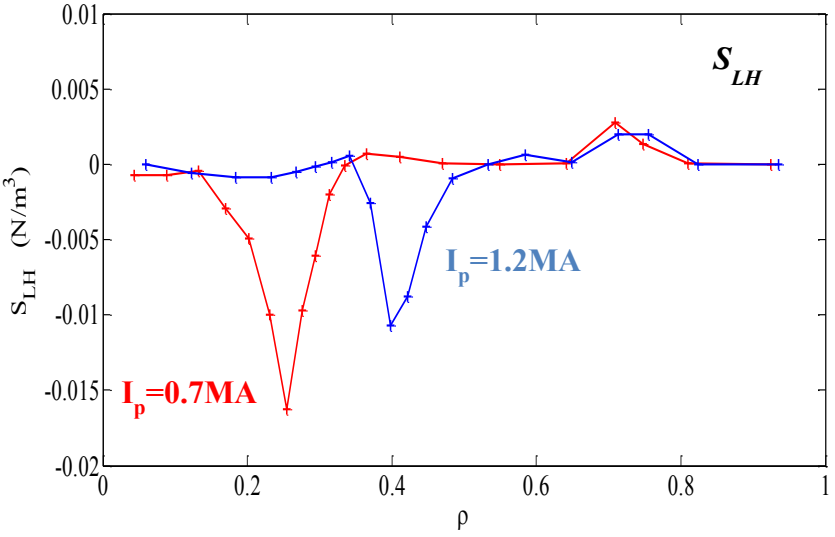

Figure 5.60. *LH wave momentum transferred to the plasma as calculated by LUKE at low (0.7 MA) and high (1.2 MA) plasma currents. It is consistent with the calculated power deposition profiles (see* Figure 5.59*).*

B. Turbulent momentum transport contribution $\pi_{i\varphi}$

The anomalous viscous tensor $\boldsymbol{\Pi}$ (eq. 2.25) derives from the anisotropic part of the pressure tensor and accounts for momentum transport in the plasma. The radial turbulent transport of angular momentum will contribute to the rotation profile. A finite $E \times B$ shear will results in a finite Reynolds stress. It is therefore important to estimate its role. The parallel component of this conserved quantity (momentum flux) is much larger than the perpendicular one; therefore the parallel momentum flux $\Pi_{\parallel}$ is a good approximation of the toroidal momentum flux Π_{φ} ($V_{\theta} \ll V_{\parallel}$).

The toroidal momentum flux consists of both a particle transport driven term and Reynolds stress (O.D. Gurcan et al., 2007). In the following and in absence of central particle sources ($\Gamma \approx 0$), only the Reynolds stress part is taken into account and the toroidal momentum flux can be formally written as:

$$\pi_{i\varphi} = -\chi_{v\varphi}\nabla_r V_{\varphi} + v_{\varphi}V_{\varphi} + \pi_{RS} \qquad (5.2)$$

where $\chi_{v\varphi}$ is the turbulent viscosity, v_{φ} the velocity pinch and π_{RS} is the residual stress. The analysis performed here will focus on the ion toroidal momentum flux since only the ion rotation is considered as a good approximation of the plasma rotation. The diffusive term $\chi_{v\varphi}$ is roughly comparable to the ion thermal diffusivity (P.H. Diamond et al., 2009). In general, the toroidal pinch may be decomposed into the turbulent equipartition (TEP) and thermoelectric (TH) parts. The TEP convection velocity is purely inward (corresponding to a pinch) and is robust and mode independent (P.H. Diamond et al., 2009). The residual stress part is independent of the

toroidal flow and constitutes a local momentum source, which means that this source may drive a flux in the absence of initial toroidal velocity (nevertheless, wave momentum could be required for such as a local source). This velocity-independent stress π_{RS} is often related to the pressure gradient contribution to the radial electric field (O.D. Gurcan et al., 2007). In ohmic plasmas, shear flow is small (X. Garbet et al., 2002) and the turbulence measurements show that the intensity gradient is large at the edge and small in the core (L. Vermare et et al., 2006). Therefore the residual stress is usually neglected for these ohmic plasmas.

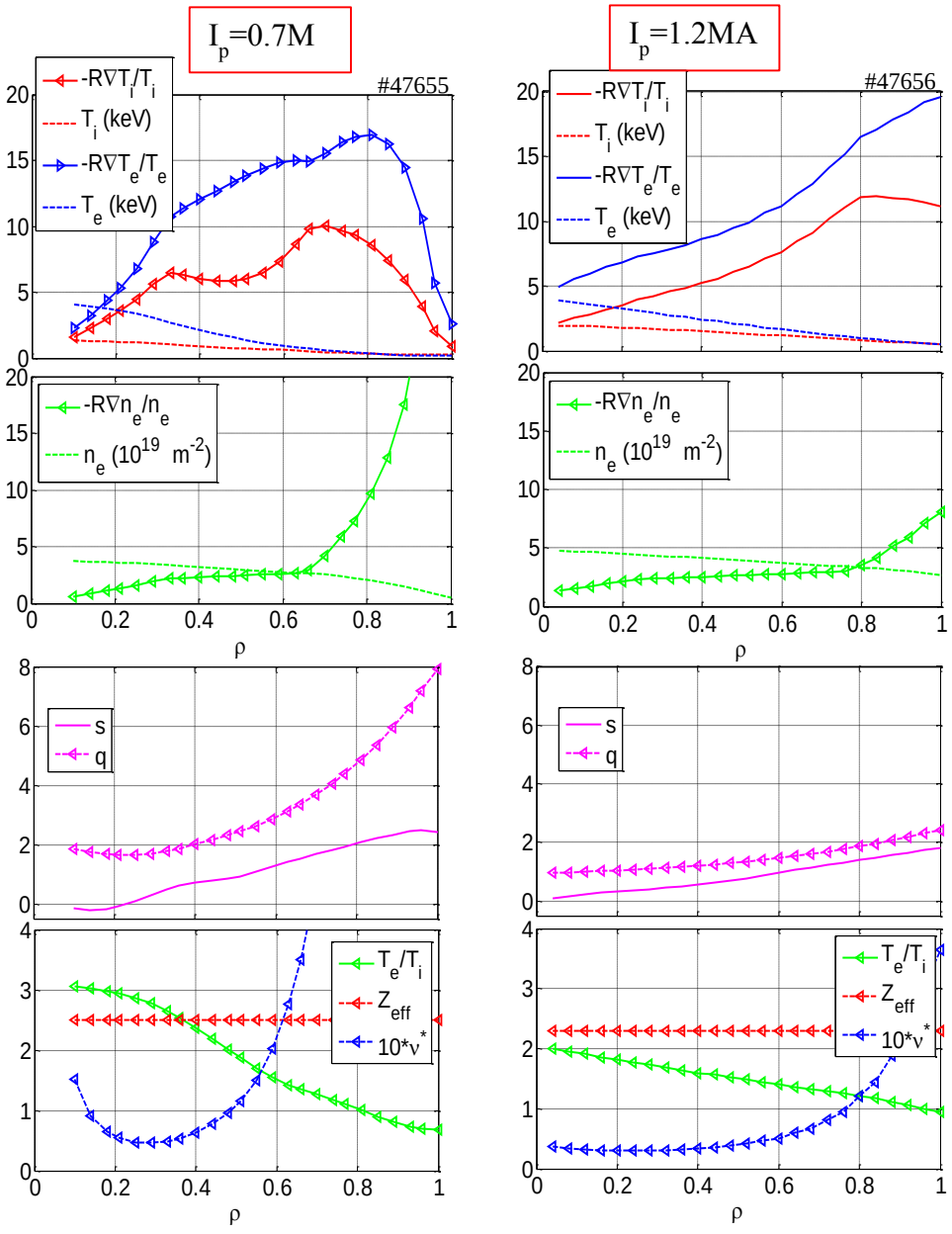

Figure 5.61. *Input parameters for QuaLiKiz and TGLF simulations of Tore Supra shots at low (left) and high (right) plasma current. All the input parameters were taken from CRONOS interpretative simulations. T_e, T_i and n_e gradients, q-, magnetic shear and collisionality profiles are calculated from the experimental profiles.*

To calculate the toroidal momentum flux, two modeling tools are available in Tore Supra: QuaLiKiz (C. Bourdelle et al., 2007) and TGLF for trapped gyro-Landau fluid (G M. Staebler et al., 2013). The latter one is a quasi-linear transport model of energy, particle and

momentum based on gyro-fluid flux equations. QuaLiKiz is also a quasi-linear transport model, based on a local gyro-kinetic eigenvalue solver and has been recently expanded to include momentum flux modeling in addition to heat and particle fluxes (P. Cottier et al., 2013).
The turbulence analysis is done for the same sets of previous discharges (section 4.1). The effect of the toroidal velocity on the turbulent modes is retained. It destabilizes the trapped electron modes (TEM) via the expansion of the trapped domain in the velocity space, but has an opposite impact on ion temperature gradient (ITG) modes by stabilizing them.
We propose here to investigate the impact of these instabilities in the LHCD plasma rotation at two different I_p. The input parameters for QuaLiKiz and TGLF simulations are plotted in Figure 5.61. The main parameters are taken from CRONOS (J-F. Artaud et al., 2010) used to perform interpretative simulations (where the experimental profiles of T_i, T_e, n_e were utilized and models for q-profile using current diffusion equation were performed. For the LH source the hard X-ray profiles were exploited). It shows that at low plasma current (I_p=0.7MA) the q-profile is slightly reversed in the plasma core with q_0 above 1, while at high plasma current (I_p=1.2 MA), the q-profile is hollow with q_0 slightly below 1. The corresponding magnetic shear $\hat{s}$ is ~0 at r/a = 0.3 (core plasma) for low I_p (becomes negative in the inner regions) and $\hat{s} \sim 0.5$ at high I_p. The change in q-profile is important because the structure of the residual stress (which is a source of an intrinsic torque through $\nabla.\pi_{RS}$) depends on the q-profile (Ö. D. Gürcan et al., 2010). The collisionality $\nu^* = \nu qR/\epsilon^{3/2}V_T$ is also illustrated for the two discharges and one can see that at low plasma current, the collisionality reads $\nu^* = 0.05$ in the core where it is lower at high plasma current and reads $\nu^* = 0.03$. According to Figure 5.61, the change in the amplitude of the q-profile has the dominant role in the change of the toroidal angular momentum flux. The modest change in $\hat{s}$ and ν^* seem to have a limited impact.

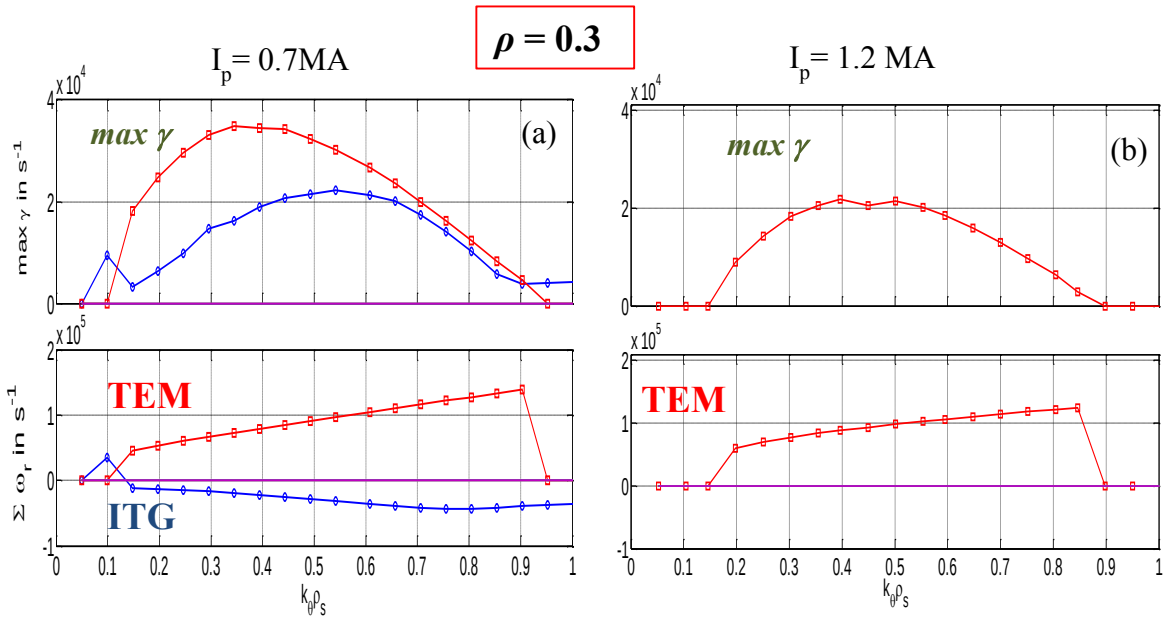

Figure 5.62. *Linear growth rate simulated by QuaLiKiz in the core plasma for low (a) and high plasma current (b) discharges at ρ =0.3. The turbulent modes (ITG, TEM) developed in the plasma are also indicated.*

Shown in Figure 5.62 is the linear growth rate of the micro instabilities inferred from QuaLiKiz simulations in the core plasma. In the core (r/a = 0.3), the TEMs are dominant in both cases (low and high I_p) as expected for the LH heated plasmas, since the central power deposition is mostly on electrons. One can see that the linear growth rate is two times larger at low plasma current than at high plasma current (Figure 5.62). Therefore, we can expect

higher turbulent transport in the low plasma current case. Another interesting observation is that the ITG modes persist only at low I_p. The dominant TEMs observed in the core reflect the high dependence of the turbulent transport on the electron temperature gradient. From the experimental results presented in chapter 4, the toroidal rotation amplitude in the core during LHCD is more counter-current at high I_p (-25 km/s) compared to the low I_p case (-10 km/s), which could be consistent with the obtained modes and partly explain the ITG modes stabilization at high I_p. In Figure 5.63, at the plasma edge (r/a = 0.7) the situation is different since dominant TEMs are observed in both cases but with linear growth rate larger at high plasma current. Thereafter, turbulent momentum fluxes at the edge plasma are expected to be higher in the high plasma current case.

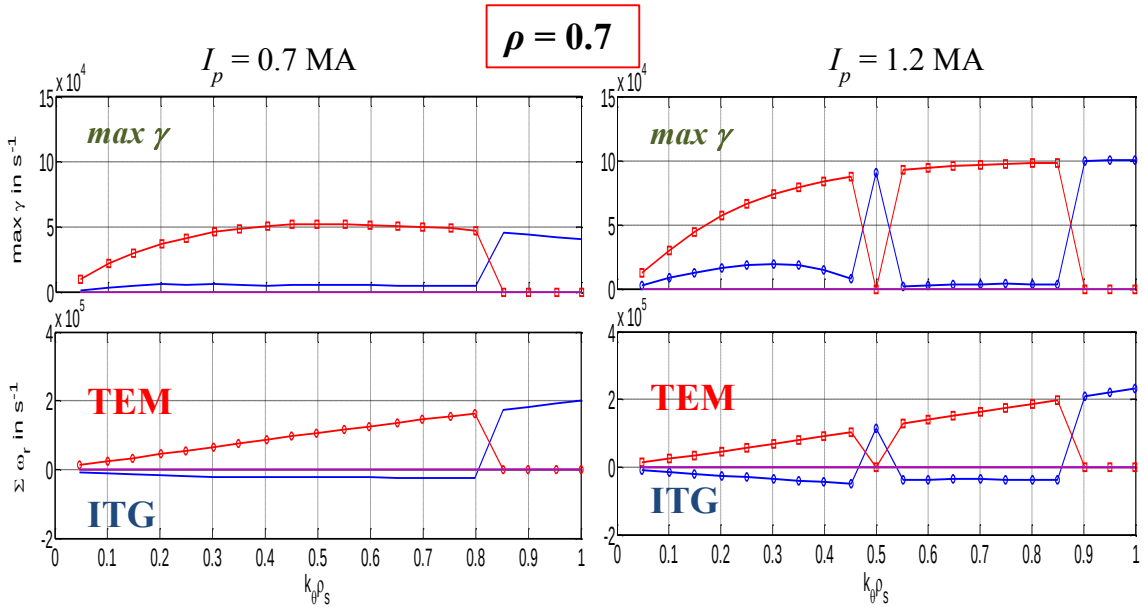

Figure 5.63. *Linear growth rate simulated by QuaLiKiz at the edge plasma for low (a) and high plasma current (b) discharges ρ =0.7. The turbulent modes (ITG, TEM) developed in the plasma are also shown.*

The simulated toroidal momentum fluxes with error bars due to the experimental toroidal rotation errors (highly dependent on toroidal rotation gradient) from TGLF are displayed in Figure 5.64. The momentum fluxes are negative, which means that the fluxes are inward in the radial direction ($V_\varphi < 0$). The momentum flux in the plasma core is notably larger at low plasma current (0.7 MA) compared to the high I_p case (15 mN/m^2 Vs 4 mN/m^2). This difference can be explained by the improvement of the energy and momentum confinement at high plasma current while at low I_p the turbulent momentum transport rises. This behavior of the momentum flux with the plasma current has also been observed for the energy flux (J. Citrin et al., 2012) which is larger at low plasma current. Simulation of momentum flux for the low plasma current discharge with the same parameters but using

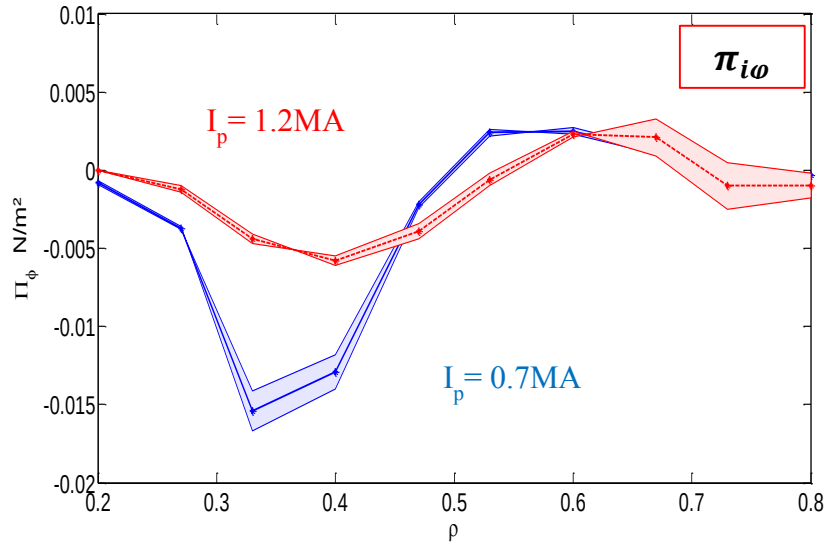

Figure 5.64. *Toroidal momentum fluxes at low and high plasma current from TGLF with the associated errors.* A clear larger toroidal momentum flux at low plasma current is observed.

the *q*-profile of the high plasma current discharge, has also been done, and the results are plotted in Figure 5.65. One can see that, the momentum flux decreases to reach the high I_p toroidal momentum flux case. Hence, the *q*-value (due to the change of the plasma current amplitude) represents the key parameter to explain the differences between the low and high plasma current fluxes.

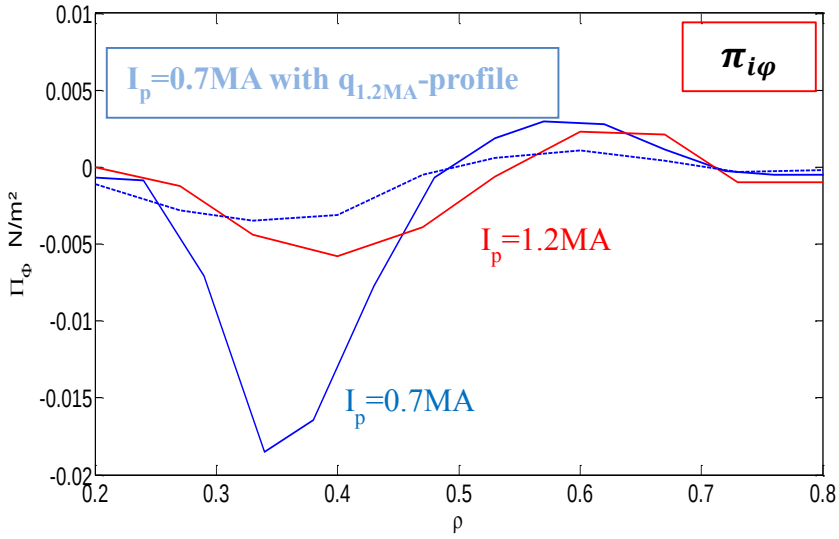

Figure 5.65. *Toroidal momentum fluxes at low I_p, high I_p and low I_p discharge with q-profile of the high plasma current discharge. The momentum flux of the low I_p discharge with changed q- profile decrease strongly. Hence, the key parameter seems to be the q-profile characteristics.*

Finally, the contributions of the different terms constituting the Reynolds stress are evaluated by the 3-point method (P. Cottier et al., 2013) and are presented in Figure 5.66. The three-point method consists of evaluating the three unknown terms by running three different simulations. The three contributions are separated by linear regression. Three independent

simulations are performed. The first one is a test simulation. The second simulation is performed with the toroidal velocity modified by 20%. Both the toroidal velocity gradient and the *E* × *B* shearing are affected by the modification of the toroidal velocity. The last one is performed with the toroidal velocity incremented by 0.05 V_{Ti}. In this case, the toroidal velocity gradient is not affected by the modification.

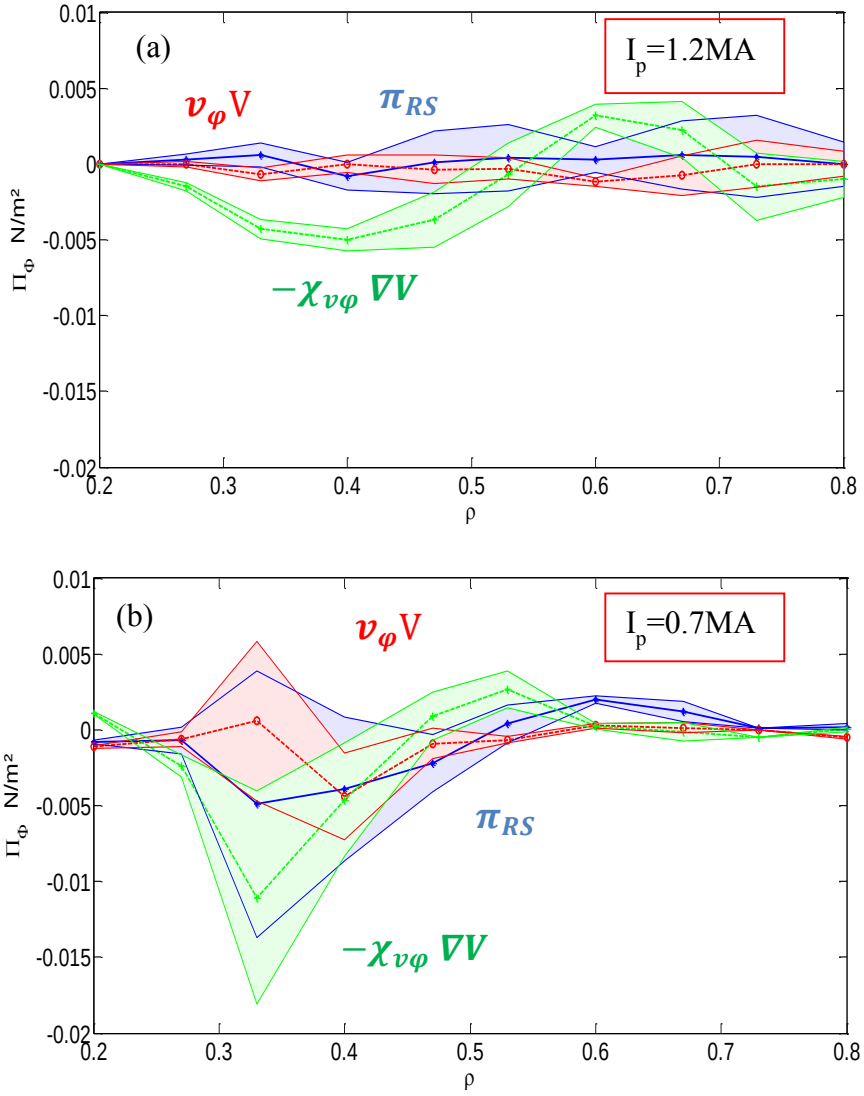

Figure 5.66. *The diferent contributions to the Reynolds stress at low (a) and high (b) plasma current. At high plasma current the momentum flux is purelly diffusive, while at low plasma current the pinch term and the residual stress rise.*

Considering that each modification has a linear effect on the momentum flux, a linear regression is pertinent to estimate the diffusivity, the pinch term and the residual stress. This 3-points method is tested by changing the increment rate by 30% per example and the toroidal rotation change by 0.1 V_{Ti} per example. The obtained flux contributions are consistent with the previous ones (with the same order of magnitude). The estimations of the errors due to this method are also plotted.

In the high I_p case, the momentum flux is principally due to the diffusive term $-\chi_{v\varphi}\nabla_r V_\varphi$. The pinch term and the residual stress contributions are negligible (Figure 5.66.a). At low I_p, the diffusive and the pinch terms develop strongly in the plasma core contrasted to the high plasma current case. The residual stress (source term) is also growing (Figure 5.66.b) and this growth can be related to the *q*-profile amplitude change which is largely above one in the plasma core (J. Rice et al., 2013).

As a summary, one can say that at low plasma current (0.7MA), the momentum turbulent transport develops significantly and a residual stress source $\nabla\pi_{RS}$ emerges to induce a deceleration of the toroidal plasma rotation. For counter-current rotation profiles, this implies an increment in the co-current direction ($\Delta V_\varphi > 0$). At high plasma current, the residual stress source doesn't develop (weak impact) and the counter-current increment due to the neoclassical friction remains strong.

C. Ripple induced force contributions

In this subsection, we investigate the forces induced by the high ripple strength (> 5%) in Tore Supra, namely the ripple induced neoclassical thermal friction and the Laplace force due to the fast particle ripple losses. Here we will focus on locally trapped particles in ripple wells (then, immediately lost to the wall) and banana trajectory particles. First, particles following banana orbits, whose banana tips can be perturbed when entering the ripple influence regions, experience a vertical drift. Collisional processes will allow them to be de-trapped eventually. In order to compensate the resulting thermal ion radial current (much larger than the thermal electron radial current) and to ensure the ambipolarity the radial electric field E_r evolves first and instantaneously, to adjusts itself. Another effect is due to the collisional friction of those banana particles on passing particles.

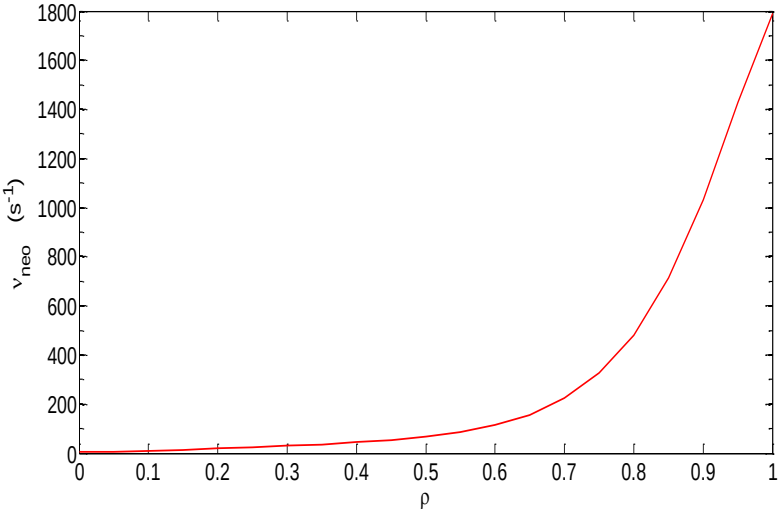

Figure 5.67. *Estimation of toroidal damping rate in Tore Supra* $\boldsymbol{\nu_{neo} = \sqrt{\frac{\pi}{2}}\, G_2(\alpha) N \delta^2 \frac{V_{Ti}}{R}}$ for standard ohmic discharge, *with* I_p *=0.7MA,* B_T*=3.8 and* $n_i = 4 \times 10^{19}\, m^{-2}$.

It is determined by the ripple-induced thermal neoclassical friction and appears to be the dominant mechanism (X. Garbet et al., 2010; P.N. Yushmanov, 1990) for thermal particles. The ripple-induced thermal neoclassical friction force of the plasma reads:

$$\boldsymbol{M_{neo} = -n_i m_i \nu_{neo}\left(V_{i\varphi} - k_T V_T^*\right)} \qquad (\mathbf{5.3})$$

where k_T is a constant related to the collisionality regime, $V_{i\varphi}$ the ion toroidal velocity, $V_T^* = \frac{\nabla_r T_i}{eB_\theta}$ the toroidal diamagnetic velocity (with T_i is the ion temperature, B_θ the poloidal magnetic field and e the proton charge) and ν_{neo} is the damping rate.

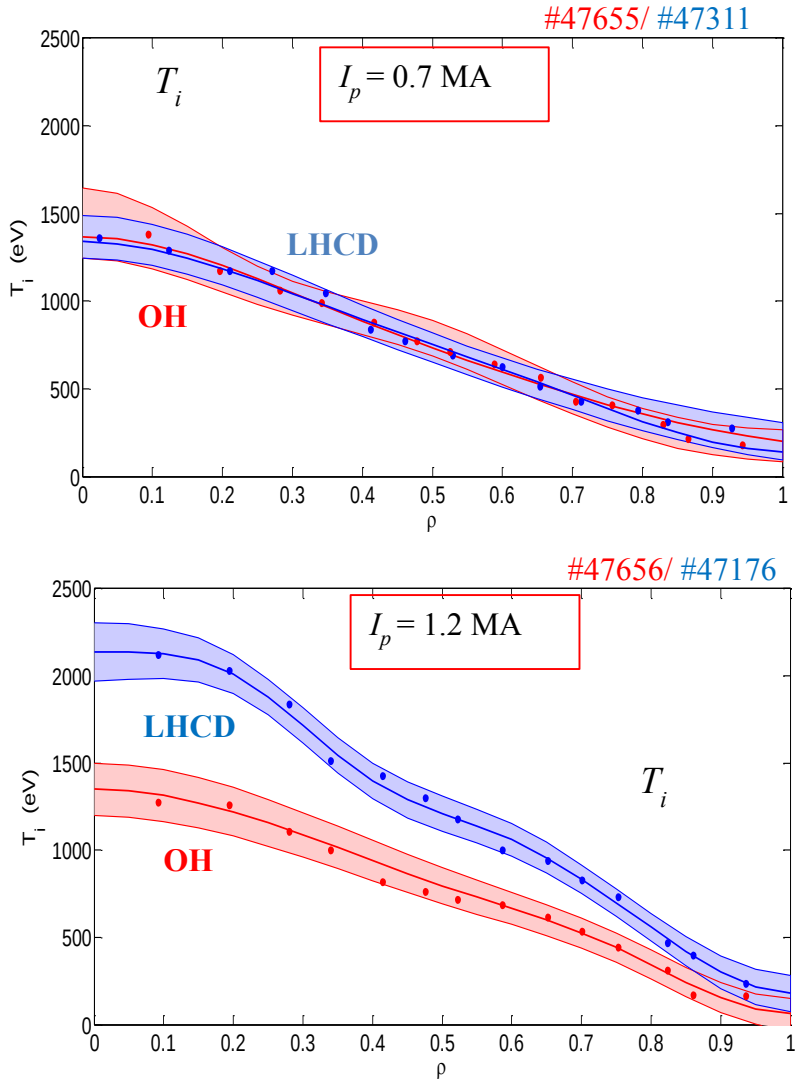

Figure 5.68. *Ti profiles from CXRS measurements (dot curves), together with the most probable T_i profiles and the confident interval at 95% as inferred from Bayesian analysis for the ohmic and LHCD plasmas discussed in chapter 4 at low (a) and high (b) plasma current discharges. A clear increase of core Ti observed at high plasma current.*

In the ripple plateau regime (observed regime in Tore Supra) an estimate of the damping rate is $\nu_{neo} = \sqrt{\frac{\pi}{2}} G_2(\alpha) N \delta^2 \frac{V_{Ti}}{R}$ and $k_T = 1.67$ (X. Garbet et al., 2010), where V_{Ti} is the thermal velocity, *R* the major radius. The function $G_2(\alpha)$ is the flux ripple average, which can be approximated by 1 (C. Fenzi et al., 2011). The calculated damping rate ν_{neo} for a standard Tore Supra discharge is shown in Figure 5.67.

The evolution of the neoclassical friction force with the plasma parameters is analyzed through the toroidal diamagnetic velocity calculations for two sets of OH and LHCD plasmas, at high (1.2 MA) *resp*. low (0.7 MA) plasma currents with $n_l = 5.9 \times 10^{19}$ m^{-2} *resp*. $n_l = 3.9 \times 10^{19}$ m^{-2} and fixed $P_{LH} = 4.8$ MW (section 4.1). It is worth pointing out the dependences of this force with the ripple amplitude and the ion temperature via the toroidal diamagnetic velocity and the ion thermal velocity. In Figure 5.68, the ion temperature profiles measured with CXRS for different plasma currents during OH and LHCD phases are displayed. We observe that the ion temperature, in the plasma core, increases (ΔT_i = 0.2 – 0.8 *keV*) with plasma current due to the energy confinement improvement at higher I_p, and increases during the LHCD through the collisional electron thermalisation on the bulk ions (the plasma density is higher at high I_p which can also explain the higher collisional thermalisation of electrons). This effect was also observed with the multi-crystal spectrometer (P.Platz et al., 1995). The change in core T_i induces a change of the gradient of T_i of about 0.2-0.8 *keV* / 0.74 *m*. For the measured ion temperature profiles, the most probable profiles inferred from Bayesian analysis are estimated with the associated confident interval including experimental errors (M. Irishkin et al., 2014). Bayesian analysis allows obtaining the probability distribution of the parameters of the splines defining the radial profiles, using constraints from the experimental measurements and taking into account their uncertainties.

The calculated toroidal diamagnetic velocity V_T^* profiles using T_i profiles displayed in Figure 5.68, are plotted in Figure 5.69. The velocity profiles are non-monotonic and in the counter-current direction, while the OH diamagnetic rotation profile is rather flat at high and low plasma current. At the core region, the velocities reach a maximum between -20 km/s and -30 km/s. It is worth noting here that these typical calculated profiles have the same behaviour and the same order of magnitude as the experimental rotation profiles (see section 4.1). It is therefore consistent with the neoclassical theory which predicts a counter-current rotation profiles ($V_\phi^{neo} = \frac{k_2}{eB_\theta}\frac{\partial T_i}{\partial r}$). The toroidal rotation profile is constrained and forced by the neoclassical friction in Tore Supra.
A clear increase of V_T^* in the counter-current direction of about -12 km/s in the core is observed in LHCD plasma at high I_p (Figure 5.69b) when compared to the OH profile. This change is linked to the change of the ion temperature gradient in the core plasma due to the LHCD and the high amplitude of the plasma current. In the low plasma current case, a slight and non-significant effect is noted in the core plasma (Figure 5.69a). Also this effect is linked to the feeble change of the ion temperature with the LHCD at low plasma current. As a preliminary result, the core toroidal plasma velocity is always in the counter-direction (except in the high turbulent plasma cases) in Tore Supra and is therefore, coherent and of the same order of magnitude than the diamagnetic toroidal velocity. This velocity evolves in the counter direction (acceleration) during the LH heating with a significant increment at high plasma current (I_p=1.2 MA) as observed for the toroidal diamagnetic velocity.

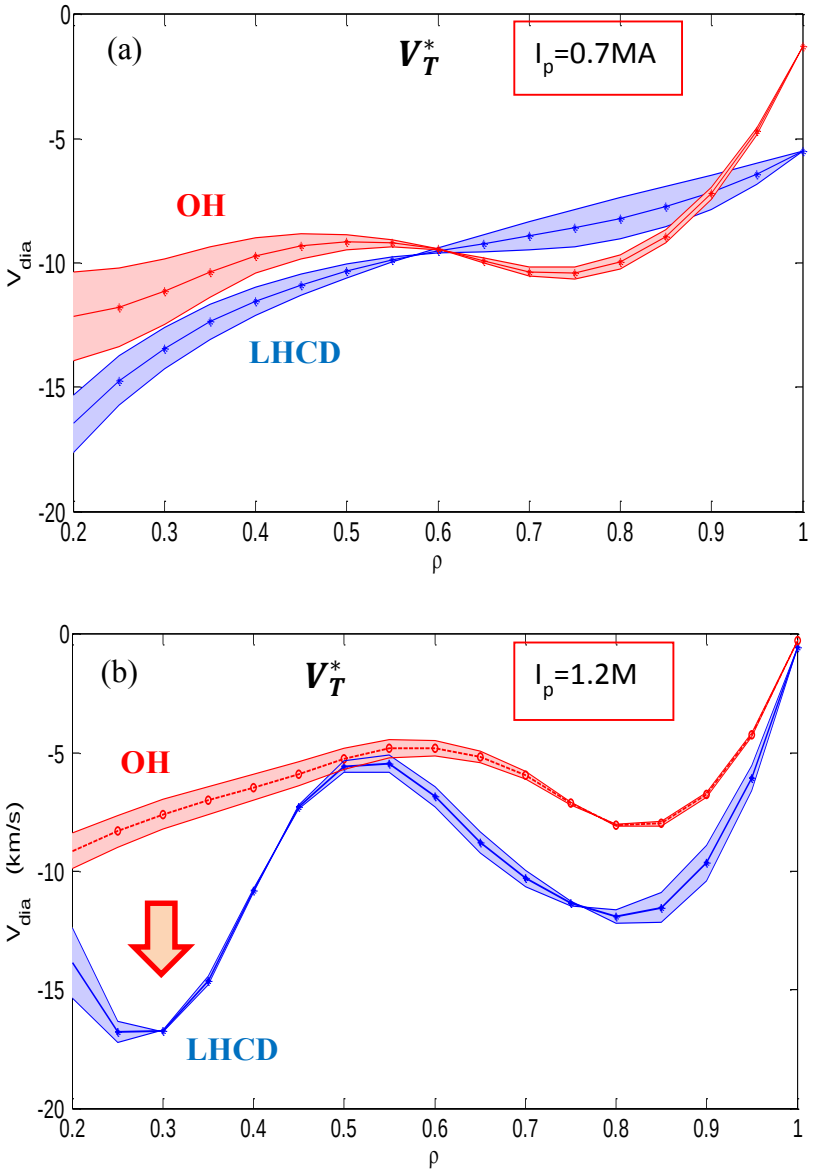

Figure 5.69. *Toroidal diamagnetic velocity* $\boldsymbol{V_T^* = \frac{\nabla_r T_i}{eB_\theta}}$ *for OH and LHCD discharges at low (a) and high* I_p *(b). A clear counter-current increment is observed at high plasma current. At low plasma current no clear trend can be observed.*

The calculated corresponding force densities M_{neo} which provoke a change on plasma rotation during the LHCD for the two cases are displayed in Figure 5.70, where a stronger neoclassical force is reported at high I_p. The forces are calculated for the toroidal diamagnetic rotation increments ΔV_T^*, using the formula of the total momentum stored inside the plasma $M_{neo} = 2V_\varphi m_i n_i / \tau_\phi$, where τ_ϕ (~50-100 ms) is the momentum confinement time.

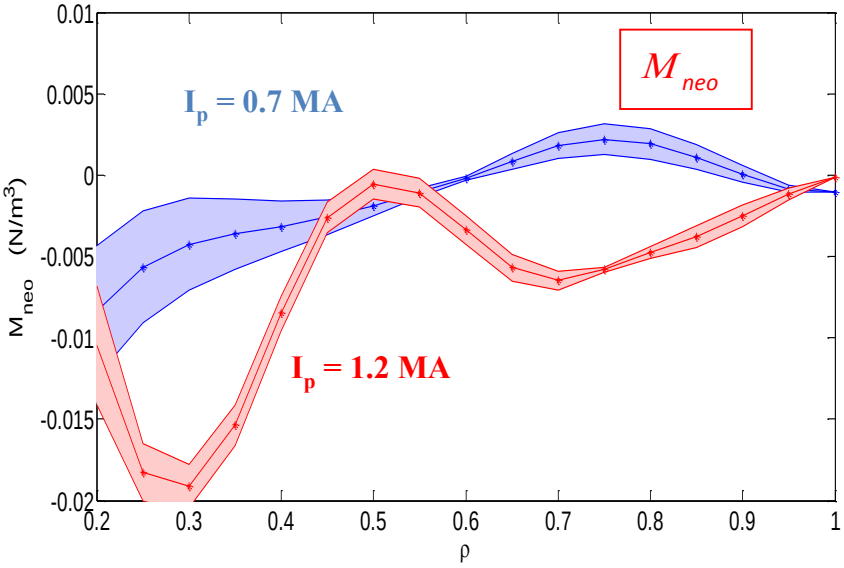

Figure 5.70. *Neoclassical force densities inducing counter-current change during the LHCD phase (calculated from the toroidal diamagnetic velocity) at low and high plasma current. Larger induced momentum is observed at high plasma current.*

The second mechanism induced by ripple is related to the locally trapped particles in magnetic ripple wells due to the dispersion of the pitch-angle. As mentioned in chapter 4, the locally trapped particle losses induce a return current which generate a $j_r \times B_\theta$ force carried by the thermal ions in the radial direction, to insure the ambipolarity condition. This mechanism appears to be dominant for fast particles (P.N. Yushmanov, 1990; L.M. Kovrizhnykh, 1999) because the trapping rate is higher and the locally trapped fast particles are immediately lost to the wall and not de-trapped by collisions eventually (because the supra-thermal particles have a low collisionality).

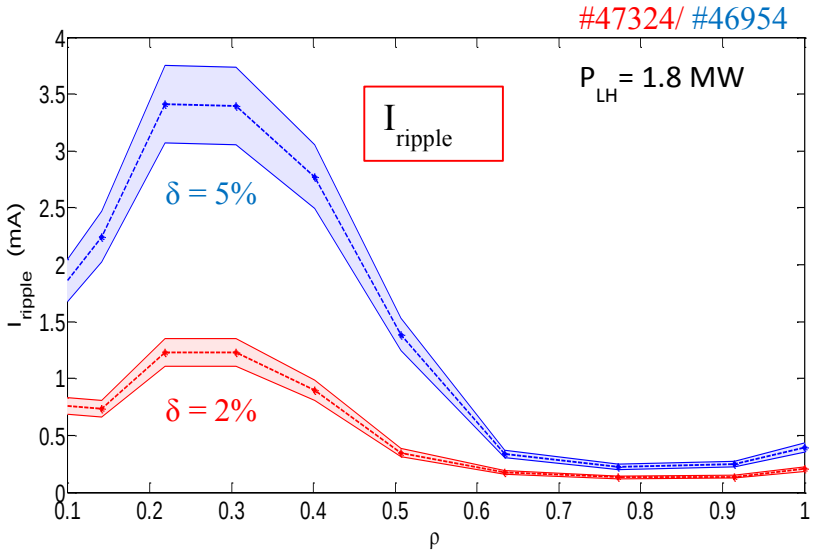

Figure 5.71. *Fast electron ripple loss profiles measured by the DRIPPLE diagnostics for two ripple amplitude δ. The fast electron ripple losses increase with the ripple amplitude δ.*

To investigate this effect, we focus on fast electron losses due to the ripple during LHCD scenarios. First, the impact of the fast electron ripple strength on toroidal plasma rotation is already investigated in section 4.1. A deceleration ($\Delta V_\varphi > 0$) of the core plasma rotation with maximum of ~8 km/s is observed when ripple strength increases. To analyze this ripple strength impact on plasma rotation, the fast electron ripple losses measured experimentally by the dedicated diagnostic DRIPPLE (V. Basiuk et al., 2001) are evaluated. The experimental observations in Tore Supra and the study made in (J.W. CONNOR et J. G. CORDEY, 1974) suggest that the ripple loss profile is peaked around R = 2.6 m (r/a = 0.3) with a width of about 20 cm. The fast electron losses collected at the top of the machine during the LHCD are off-axis, with a maximum losses at r/a ~ 0.35, then decreasing towards the edge with a minimum losses at r/a ~ 0.6, as illustrated in Figure 5.71. It shows the measured fast electron ripple losses for two plasmas with different ripple amplitudes δ at the plasma boundary. The measured error bars are due to the sawtooth events and noise.

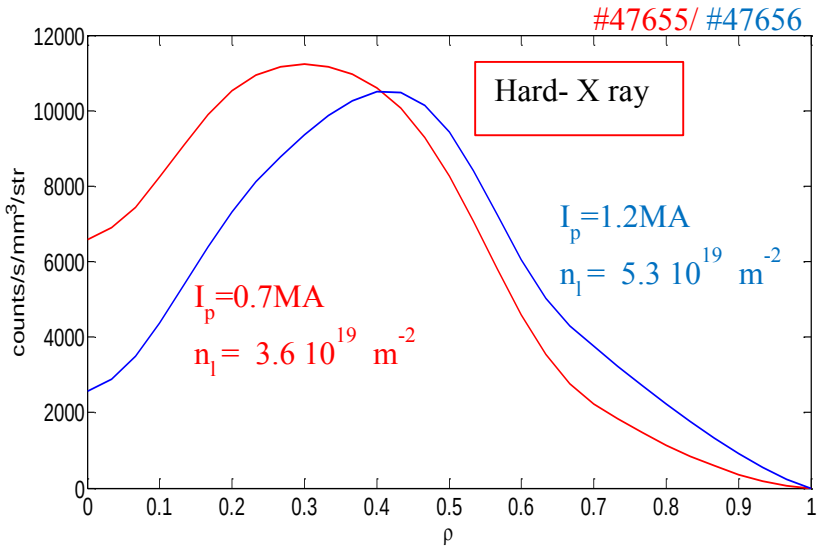

Figure 5.72. *Hard X-ray absorption profiles for two LHCD discharges at P_{LH}=4.8MW with different plasma current (0.7MA red and 1.2MA blue). For higher I_p the profile deposition is broader and outermost.*

These fast electron ripple loss profiles are consistent with the LH power deposition profiles where the wave-electron resonance occurs. It corresponds to the fast electron source location as shown in Figure 5.72, representing the hard X-ray absorption profiles (Y. Peysson, 1999) for two discharges, at low and high plasma current. It is also consistent with the limit of the good confinement domain (chapter 2) where ripple has no influence.

Figure 5.73 shows the evolution of the fast electron ripple losses (I_{ripple}) with plasma current. The ripple loss currents of two plasmas with the same parameters but at different plasma current I_p =0.7 MA and I_p =1.2 MA are measured. The losses increase with plasma current (~ +30%). They go from maximum ripple current I_{ripple} = 10 *mA* at I_p = 0.7 MA to I_{ripple} = 13 mA at I_p =1.2 MA. This trend (increase of the ripple losses with plasma current) is confirmed by the empirical scaling law relating the fast electron ripple loss current to the main plasma parameters such as electron density and plasma current, proposed for Tore Supra discharges (chapter 2):

$$I^{e}_{lost}[mA] = \frac{60\ P^{\alpha}_{LH}[MW]\ \ I^{\beta}_{p}[MA]\ \ B^{\gamma}_{tor}[T]}{n^{\delta}_{l}[10^{19}m^{-2}]} \qquad (5.4)$$

With $\alpha = 1.06 \pm 0.05$; $\beta = 0.76 \mp 0.06$; $\gamma = 0.28 \pm 0.06$; $\delta = 1.96 \pm 0.13$.

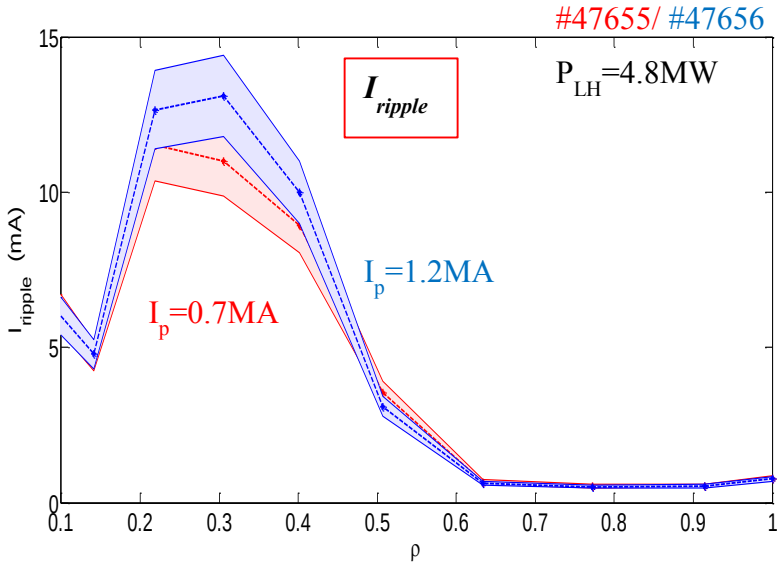

Figure 5.73. *Fast electron ripple loss currents for two different plasma current (I_p =0.7 MA and I_p =1.2MA) discharges. The ripple loss current profiles are consistent with the LH power deposition. The ripple losses increase with I_p.*

The ripple-induced fast electron losses yield a return current radially directed outwards and carried by ions (the electron flux is smaller than the ion flux by factor of $\sqrt{m_e/m_i} \ll 1$) in order to maintain the ambipolarity condition. This return current induces a $J_{ripple} \times B_\theta$ force (Laplace force) acting in the co-current direction ($\Delta V_\varphi > 0$). The corresponding momenta to the measured ripple loss currents at high and low plasma current are shown in Figure 5.74. To calculate the current density J_{ripple} the following formula is used:

$$j_{ripple}(r) = \frac{I_{ripple}}{2\pi^2 R r} \qquad (5.5)$$

As expected, the ripple induced momentum is larger at high plasma current, because the ripple losses are more important and also because the poloidal magnetic field increases with I_p ($B_\theta \propto I_p/a$). The maximum measured momentum is at r/a =0.35, with an amplitude of $M_{Jripple \times B} \approx 4.10^{-3} N/m^3$ at I_p =0.7 MA and $M_{Jripple \times B} \approx 8.10^{-3} N/m^3$at I_p =1.2 MA. An estimation of toroidal rotation which can be driven by this mechanism, balancing the ripple induced momentum by the total momentum stored inside the plasma $M_{jripple \times B} = 2V_\varphi m_i n_i / \tau_\phi$ gives positive rotation increments of about ΔV_φ = 4-7 km/s in the co-current direction ($\Delta V_\varphi > 0$ e.g.

deceleration). One can note that, these increments are consistent with the experimental observations.

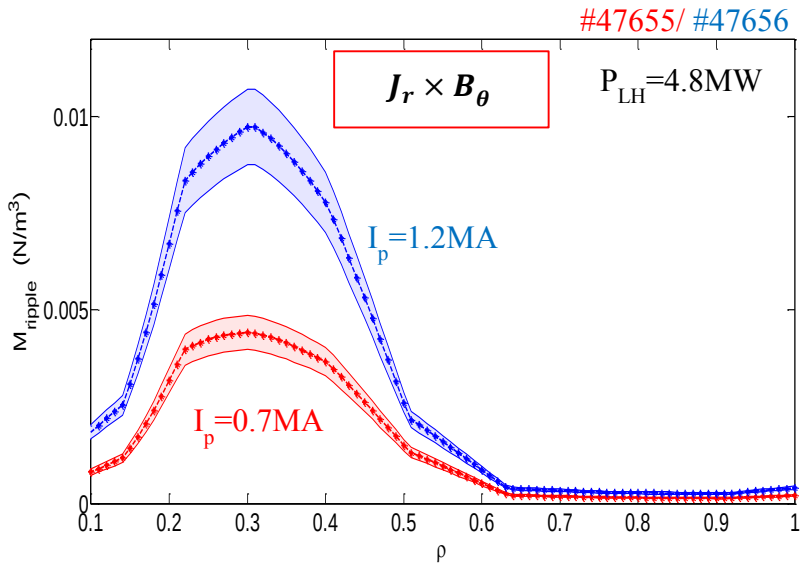

Figure 5.74. *Toroidal momentum due to the Laplace force at high and low plasma current discharges. As expected, the Laplace force is larger at high plasma current.*

D. MHD activity contribution

The plasma rotation and momentum transport are often observed to be impacted by the MHD activity such as sawteeth. Sawtooth activity is observed in some LHCD discharges analyzed in this thesis. The core rotation evolution during sawtooth events has been investigated in section 4.1, for an ohmic discharge. The observed rotation increments show a behavior comparable to the impact of sawteeth on the temperature profile according to the Kadomtsev (R-J. Hastie et al., 1998; B.B. Kadomtsev, 1975) model with a flattening of the profile around the surface q=1. This induces a particle, energy and momentum redistribution. Sawtooth crashes could also influence the rotation during the magnetic reconnections through the toroidal electric field E_φ with a sharp increase to reach a few kV. This effect on E_φ is fast, transient (μs) and much more localized in space (limited to the surface q=1) which makes it difficult to investigate.

During ICRH, with high minority concentration and at high plasma current, giant sawteeth were reported in Tore Supra (section 4.2). The crash of these giant sawteeth induce a plasma mixing where the fast ion population is expelled from the q=1 surface. The sawtooth crash also generates neoclassical tearing modes (NTM) on the q=3/2 (or q=4/3) surface which prevents the sawtooth re-building (P. Maget et al., 2005). The observed effect on toroidal rotation is a strong co-current increment that cannot be explained by the plasma mixing or flattening effect (C. Fenzi et al., 2011). In this thesis, the efforts aiming to understand this effect were not conclusive.

5.1.2. Momentum Balance

Starting from the momentum balance equation described earlier in this chapter and then analyzing the different terms of the equation during LHCD and for different plasma current amplitudes, now we propose to investigate the resulting effect from the competition of the all mechanisms taken as a whole. The momentum balance equation in the toroidal direction with the different contributions in steady state is reiterated below:

$$n_i m_i \nabla.\left(-\chi_{v\varphi}\nabla_r V_\varphi + v_\varphi V_\varphi\right) = e_i n_i E_\varphi + j_r \times B_\theta - n_i m_i \nu_{neo}\left(V_{i\varphi} - V_T^*\right) + S_{LH} - n_i m_i \nabla.\pi_{RS} \quad (5.6)$$

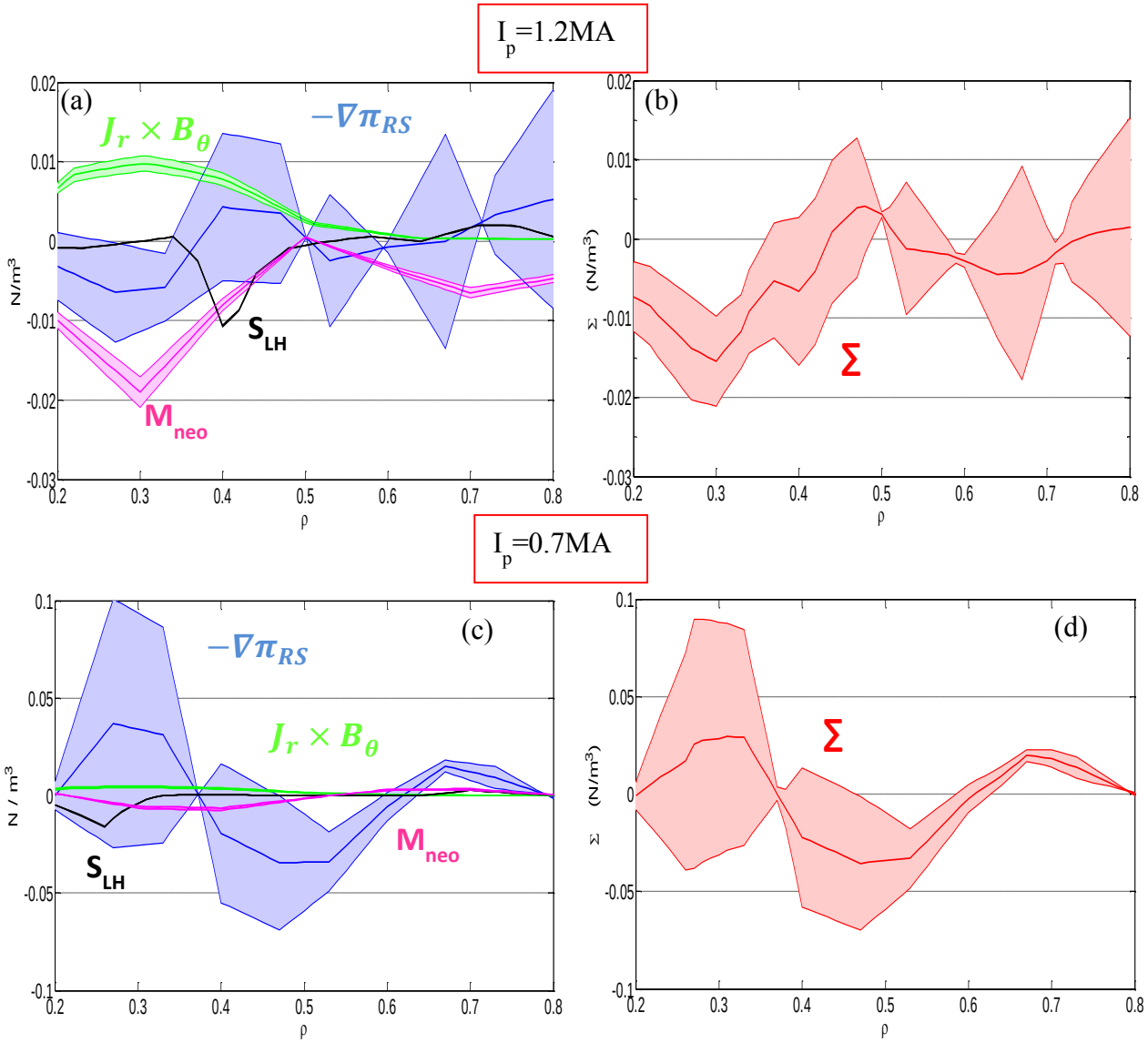

Figure 5.75. *The different sources (Laplace force, residual stress, neoclassical friction and LH wave source) contributing to the momentum balance equation during the LH-heating. The total source is also exhibited (red solid curve). We can see that at high plasma current the total source is close to the neoclassical force (a), while at low plasma current it is close to the residual stress (b). The two cases are plotted with different Y axis scales in order to highlight the trends.*

The right hand side with all sources, acting during the LH phase is plotted in Figure 5.75. All the sources and their resulting forces are represented. The residual stress part of the Reynolds stress is assimilated as a source which develops by itself in the plasma and therefore, is put on the right hand side of the equation. One can see that the neoclassical friction through the toroidal diamagnetic velocity is the dominant source at high plasma current (Figure 5.75.a). At low plasma current, the divergence of the residual stress represents the principal source of momentum in the plasma (Figure 5.75.b).
To analyze the impact of the left hand side which counts for momentum transport, CRONOS (J-F. Artaud et al., 2010) simulations using the deduced transport coefficients (diffusive and pinch) and the total momentum source (during LHCD) are performed for the two previous discharges. The results are displayed in Figure 5.76, which represents the rotation increment profiles due to the LHCD. The experimental rotation increments are also shown. The calculated rotation increments are in reasonable agreement with the experimental ones (within the error bars), especially in the core plasma region, since this analysis is focused on the dynamics of the core toroidal rotation. The edge flows and edge turbulent sources are not considered. Hence, the effects on the edge rotation are out of scope of our analysis.

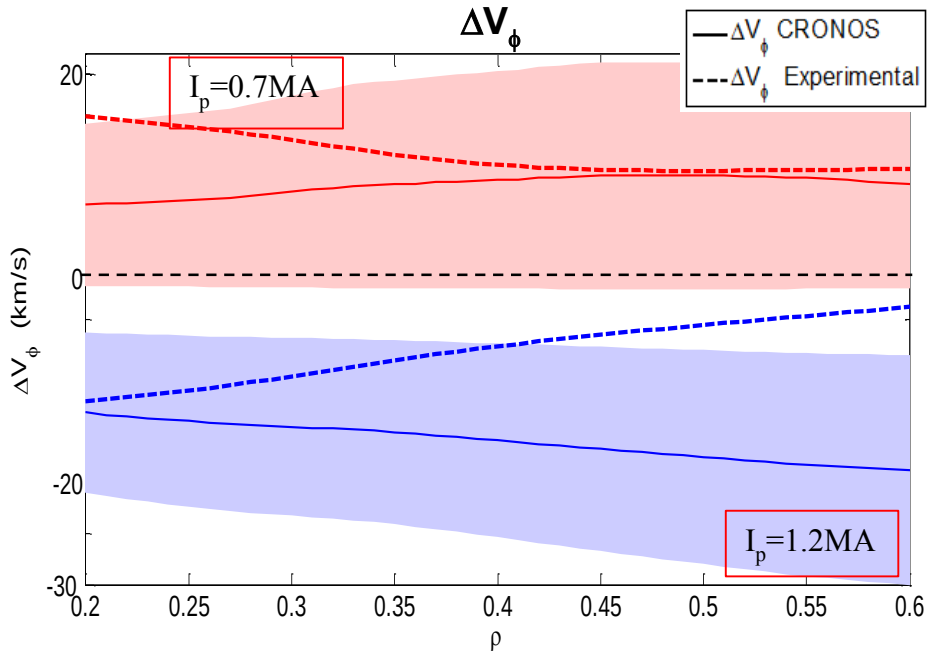

Figure 5.76. *Experimental and calculated (from CRONOS) induced rotation increment during the LH phase. In the core plasma region, the calculated increment is in good agreement (in term of direction and amplitude) with the experimental observations.*

As mentioned above, the toroidal momentum flux is approximated by the parallel momentum flux and consequently $V_\varphi \sim V_\parallel$. From the study of the different terms contributing to the toroidal momentum balance equation that governs the plasma rotation, in steady state, a clear approach of the LHCD impact on toroidal plasma rotation can be drawn:

The non-monotonic counter-current rotation profiles, observed experimentally, have the same behavior and amplitude as the diamagnetic toroidal velocity due to the neoclassical ripple-

induced friction. The neoclassical toroidal rotation is always in the counter-current direction and therefore, consistent with the experimental measurements of toroidal rotation.

To explain the rotation evolution during LHCD, it should be considered that the toroidal velocity evolution results from a competition between the neoclassical ripple-induced viscous damping, the fast electron ripple losses, the magneto-hydrodynamic modes and the turbulent transport processes (which is known to decelerate the plasma and might reverse the sign of the toroidal rotation and make it co-rotation) (J. E. Rice et al., 2004; L-G Eriksson et al., 1997). In LHCD plasmas, at high I_p (1.2 MA), the turbulent momentum transport is weak and the resulting momentum sources due to the locally trapping, the ripple-induced neoclassical friction and the wave momentum source is negative, dominated by the ripple-induced neoclassical friction. It induces an increment in the counter-current direction of the same order of the experimental observed change (section 4.1). At low plasma current (0.7 MA), the turbulent momentum transport develops strongly because of the confinement degradation, the residual stress grows to drive a resulting momentum source in the co-current direction with the good increment. In other words, this theoretical approach suggests that at high plasma current the toroidal plasma rotation is governed by the neoclassical effects, while at low plasma current the rotation is dominated by the turbulent momentum transport through the residual stress emergence. The arguments elaborated here are consistent with the experimental results of LHCD induced rotation in Tore Supra (section 4.1). The complex study achieved here reflects the complexity of the intrinsic toroidal rotation. Finally, it is worth mentioning that, the momentum flows from the plasma edge were not taken into account.

5.2. Models for the toroidal rotation with ICRH

Toroidal rotation with ion cyclotron resonance heating has been an active field of research for fifteen years. Experimental and intense theoretical efforts have been carried out in order to understand the intrinsic rotation evolution during ICRH.
In this section, we present the different models proposed to explain the toroidal rotation profiles and the rotation changes observed during ICRH in Tore Supra. In particular, we will discuss the role of the fast ions generated during ICRH (L-G. Eriksson et al., 1992), the neoclassical theory (A.L. Rogister et al., 2002) and the mechanisms related to the presence of ripple (P.N. Yushmanov, 1990; L.M. Kovrizhnykh, 1999).

5.2.1. Mechanism due to the fast ion generation

The locally trapped fast ions generated during ICRH which have banana orbits or non-standard trajectories, and will be treated in a similar way as the fast electrons generated during LHCD and lost in ripple wells. Those fast ions are less collisional, not affected by the radial electric field and are always lost to the wall. This fast ion loss current induces a return current carried by thermal ions in the radial direction which generates a Laplace force $J_{ripple,fast} \times B_\theta$.in the plasma. The estimations of this Laplace force at low and high minority heating concentrations are shown in Figure 5.77. As expected, the ripple induced Laplace force is larger at low minority concentration. The ripple losses are less important at high minority concentration, because the high energy tail of the resonating ions in distribution function is weak and limited (L-G Eriksson et al., 2001).

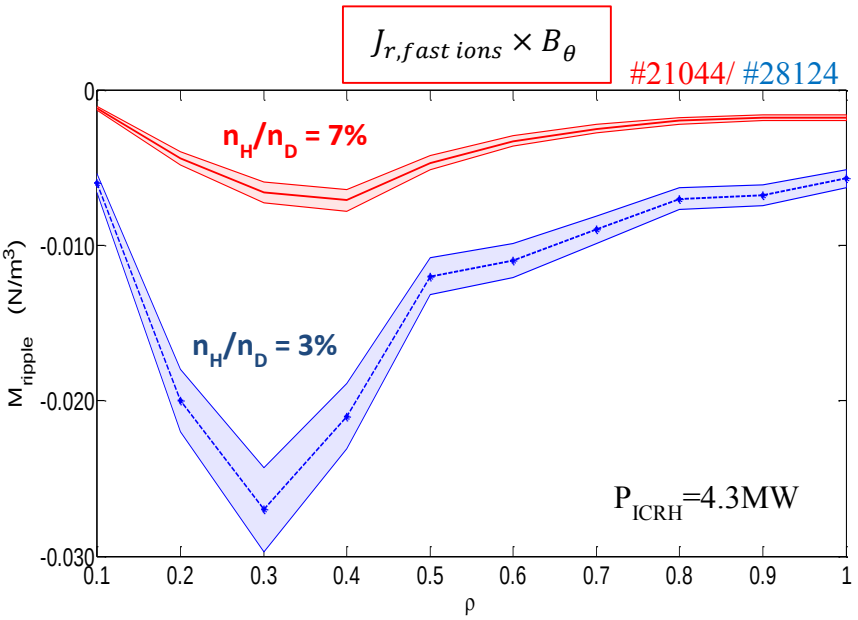

Figure 5.77. *Toroidal momentum due to the Laplace force at high and low minority heating concentration discharges. As expected, the Laplace force is larger at low* n_H/n_D.

The maximum measured force is at *r/a* =0.3, with an amplitude of $M_{Jripple\,,fast\times B} \approx -30.10^{-3} N/m^3$ at low n_H/n_D and $M_{Jripple,fast\times B} \approx -8.10^{-3} N/m^3$ at high n_H/n_D. An estimation of toroidal rotation which can be driven by this mechanism, balancing the ripple induced momentum by the total momentum stored inside the plasma $M_{ripple,,fast\times B} = 2V_\varphi m_i n_i / \tau_\phi$ gives negative rotation increments of about ΔV_φ = 7-25 km/s in the counter-current direction (an ion is travelling in the co-current direction on the outer leg of its orbit, and a loss of it, will therefore give a counter-current torque on the plasma).

5.2.2. Neoclassical theory

The mechanism related to the neoclassical friction which is dominant for banana particles as stated in section 5.1, influences the plasma rotation through the toroidal diamagnetic velocity, because of an increase in ion temperature gradient. During ICRH, a typical variation in the ion temperature in the plasma core is reported in Tore Supra and shown in Figure 5.78. The estimation of the rotation increment due to the increase of the T_i gradient of about ~1 keV/ 0.74 m gives $\Delta V_T \sim 20\ km/s$ in the counter-current direction. Therefore, this mechanism can explain partly the counter-current rotation increment observed at low minority concentration in Tore Supra.

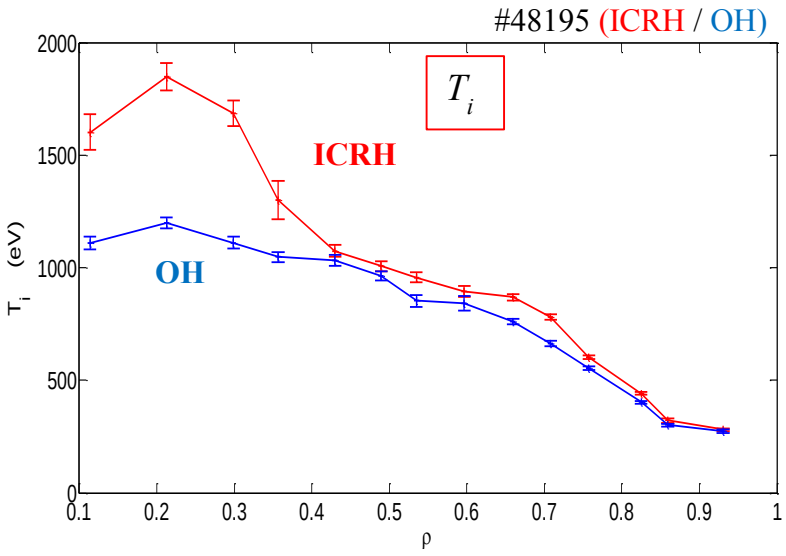

Figure 5.78. *Ti profiles from CXRS measurements for the ohmic and ICRH plasmas discussed in chapter 4 at low minority concentration. A clear increase of core Ti is observed which induces a counter-current increment in plasma rotation.*

5.2.3. Other mechanisms

A. Momentum transferred from ICRF waves

In Tore Supra, the phasing of the ICRH antenna is in the dipolar configuration (symmetric spectrum) which permits a better coupling of the power to the plasma. Owing to the fact that the wave-particle resonance takes place in different positions for co- and counter-current propagating waves because of the Doppler shift, the amount of power absorbed by the resonating ions is not equal for positive and negative toroidal mode numbers. This leads to a torque in the plasma which is absorbed by fast ions and then transferred to the bulk plasma. To experimentally observe this effect, a change in the antenna phasing for example with varying the phasing from a predominant propagation in the co-current direction to a counter-current propagating one is investigated. This ensures that the imbalance between power absorbed from waves with positive and negative toroidal mode numbers is strong. In JET, indeed a difference in the rotation when the phasing of the antennas was changed has been detected, which was consistent with the difference in the absorbed wave momentum. However, in all cases, i.e. irrespective of the phasing, the plasma was found to rotate in the co-current direction. Thus, it appeared to be a weak effect and not the dominant mechanism to explain the observed plasma rotation. It is worth mentioning that the finite orbit width effects also play a role in the process. In Tore Supra, we expect the same weak effect on the toroidal plasma rotation.

B. Accretion theory

The accretion theory is based on the existence of a kinetic toroidal momentum source due to the turbulence activity at the edge of the plasma (B. Coppi et al., 2002).
The particles will diffuse to the wall when resonating with the turbulent modes related to the temperature and density gradients and therefore, transfer their momentum in the direction of the modes. In order to insure the total momentum conservation, the momentum transport inside the plasma will be in the opposite direction. Due to the momentum transport from the edge, a change in the core plasma rotation is expected. A counter-current rotation in L-mode and co-current rotation in H-mode are expected, according to this theory, which is consistent with C-Mod observation in H-modes.
The scaling of the toroidal rotation with W_{dia} / I_p observed experimentally in C-Mod confirms the prediction of the theory. However, the co-current acceleration observed in L-mode Tore Supra plasmas cannot be explained by this model. It is also complicated to estimate the contribution of this mechanism to the toroidal plasma rotation since no toroidal rotation estimation has been made in (B. Coppi et al., 2002) for C-Mod.

C. Dipolar torque

To change the plasma rotation, no net torque on the plasma is needed. It is sufficient to have a dipolar torque (whose integral over the plasma is zero) and radial transport of the toroidal

momentum due to the collisional processes. Due to finite orbit width effects and spatial transport of the resonating ions, there is always such a dipolar torque present in ICRF heated plasmas. The effect of this mechanism on plasma rotation changes if the ICRF resonance layer is on the low or high field side of the magnetic axis. Thus, this particular theory would tend to predict co-current rotation for low field side resonances and counter-current rotation for high field side ones (L-G. Eriksson and F. Porcelli, 2002). This change in the rotation direction has not been supported by experimental observations.

5.2.4. Conclusions

Different mechanisms induced by ion cyclotron resonance heating aiming to explain the rotation increments induced at high and low minority concentration configurations were reported:

- The mechanisms related to the wave-momentum transfer during ICRH and dipolar torque due to finite orbit width effects and spatial transport of the resonating ions, may impact the plasma rotation but it appears to be weak and not the dominant mechanisms to explain the observed plasma rotation.

- The accretion theory proposed in (B. Coppi et al., 2002) could explain the co-current observed rotation in H-mode at C-Mod and could also explain the counter-current increment observed in L-mode, in Tore Supra, but no estimation of this mechanism has been provided in order to confirm it.

- The Laplace force generated by the fast ion ripple losses combined to the neoclassical friction give a consistent explanation of the counter-current rotation observed at low n_H/n_D in Tore Supra. Also, the estimation of the increments is in good agreement with the experimental results.

In this section, the co-current thermal force and the friction between the locally trapped thermal ions and the non-locally trapped thermal ions which are proportional to the ion temperature gradient, proposed by Mikhailovskii (A.B. Michailovskii et al., 1995) was not reviewed because it is a disputed mechanism. Indeed, this mechanism seems to be significant for the particles following the banana orbits (X. Garbet et al., 2010; L.M. Kovrizhnykh, 1999) but not for the locally trapped particles.

In our analysis, the co-current change observed at high n_H/n_D is still unsolved, but the turbulence investigations were not achieved for the rotation with ICRH and could explain the observed co-current increments in Tore Supra.

5.3. Summary

Different mechanisms behind the intrinsic toroidal rotation were investigated in order to predict its evolution during LHCD and ICRH in Tore Supra.

- The non-monotonic counter-current experimental rotation profiles are consistent in terms of direction and amplitude with the toroidal neoclassical velocity profiles which are proportional to the ion temperature gradient. During LHCD, neoclassical and turbulent effects on toroidal rotation are at play and in competition. It appears that the neoclassical friction governs the rotation change during LHCD at high plasma current amplitude while at low plasma current, turbulent effects seems to be the dominant source through the divergence of the residual stress.
  In C-Mod the turbulent momentum flux (Reynolds stress) through the divergence of the residual stress is believed to be the candidate to explain the rotation changes during LHCD (J. Rice et al., 2013). At JET the co-current rotation observed during LHCD at low plasma current is explained by the turbulence transport processes. Recent results where either co- or counter-current rotation increments were reported for discharges with the same parameters (Nave EPS-2014) but different q-profiles. These new observations are under investigation. At EAST, the thermo-electric pinch is proposed to explain the co-current increment observed during the LHCD (Y.Shi et al., 2011).

- During ICRH, the neoclassical friction combined with the Laplace force due to the fast ion ripple losses are the mechanisms capable to explain the counter-current increment observed at low minority concentration in Tore Supra. At high minority concentration, the fast ion ripple losses decrease because the ion heating is more efficient and therefore induce less counter-current increment on toroidal rotation. The turbulent momentum flux is strongly believed to explain the co-current change in toroidal rotation and turbulent momentum transport simulations are necessary to clarify this effect.
  At JET, several mechanisms have been proposed to explain the intrinsic rotation during ICRH, a review of these mechanisms is summarised in (L-G. Eriksson et al., 2009). Simulations were performed to calculate the torque generated during ICRH and then, a simple transport equation is used to compute the toroidal plasma rotation. It is found that the dominant contribution factor could be the torque exerted by the fast ICRH accelerated ions.

From the above study, different mechanisms are identified to have an impact on the toroidal plasma rotation. The competition between the different mechanisms and the resulting dominant effects are different between the machines, and the analyses have to be adapted depending on the machine characteristics. For example, in Tore Supra, the ripple effects are expected to be significant while at C-Mod the turbulence is the dominant mechanism and ripple effects are negligible.

VI

Conclusions

Fusion energy is a promising candidate for the future energy production. To reach the fusion reaction on the earth, high temperatures are necessary. The magnetically confined plasmas make these temperatures possible and then the fusion of nuclei present in the plasma. The most developed concept of magnetically confined plasmas is the tokamak. Despite the success of the tokamak concept, many challenges are still relevant and have to be solved. One of these challenges is the plasma stability and performance.

To ensure the plasma stability and increase the performance of tokamaks, it is necessary to know which mechanisms influence the stability and the performance of the plasma. It has been observed in several tokamaks that the plasma performance depends strongly on plasma rotation. Strong rotation has an effect on the turbulence with stabilization but also enhancement in some cases, represents an important factor for the transport barrier generation and stabilizes the MHD instabilities such as resistive wall modes (RWM). Hence understanding intrinsic plasma rotation has become a critical issue for future devices such as ITER, as external sources will play a minor role. Intrinsic toroidal rotation has been observed experimentally in present tokamaks, in the absence of external sources, but the physical mechanisms governing its generation are not entirely understood. Thus, reliable predictions for future experiments are lacking. In this thesis, we have investigated the toroidal plasma rotation in Tore Supra during radio frequency heating schemes.

Tore Supra is a very suited device to study the intrinsic plasma rotation during radio frequency heating. First, charge exchange recombination spectroscopy using perpendicular diagnostic neutral beam injection gives us a complete view of plasma rotation over the whole minor radius. A laser is used as a reference line for Doppler shift in order to get very accurate rotation measurements. Second, the high capability heating with 6 MW LHCD and 10 MW ICRH allows us to analyze the evolution of the plasma rotation during the RF heating and current drive.

A large database of LHCD plasma discharges has been explored. Observations of LHCD effects on toroidal rotation in L-mode plasmas have been analyzed.

- Core rotation is found to increment in the co- or counter-current direction depending on the plasma current (I_p). At low plasma current, the induced rotation is up to +15 km s^{-1} in the co-current direction, the rotation profile being affected over the whole plasma minor radius. At higher plasma current, an opposite trend is observed, the core plasma rotation incrementing up to −15 km s^{-1} in the counter-current direction, the profile being affected up to $r/a < 0.6$ only. At the zero crossing point, which is defined when the plasma rotation profile is not affected by LH injection is $I_p \sim 0.95$MA. In both low and high I_p cases, rotation increments are found to increase with the injected power.

Several mechanisms in competition which can induce co- or counter-current rotation in Tore Supra LHCD plasmas are investigated and typical order of magnitude are discussed. How those effects evolve with plasma parameters and how they compete are important issues addressed in this thesis.

- The neoclassical toroidal rotation is always in the counter-current direction. The neoclassical toroidal diamagnetic velocity is of the orders of the experimental toroidal velocity (~ -20 km s^{-1}). The co-current change in rotation is consistent with a fast electron ripple loss mechanism, while thermal ripple induced neoclassical friction and absorbed LH wave momentum from resonant electrons are expected to influence the rotation in the counter-current direction. Finally, the numerical simulations show that the radial turbulent momentum transport does impact the rotation behavior, inducing increments in the co-current direction. At high plasma current, the rotation evolution in the lower hybrid phase is controlled by the neoclassical friction force due to the trapped thermal ions in banana trajectories through the toroidal diamagnetic velocity. This force results in the counter-current increment as observed in the experimental measurement. At low plasma current the rotation is dominated by turbulent momentum transport. The Reynolds stress grows strongly compared to the high plasma current case and acts as a co-current force through its residual stress contribution. Momentum transport simulations are also performed with the CRONOS code using the calculated transport coefficients, in order to assess the rotation increments induced by LHCD. The results tend to confirm the estimations and then the resulting effect on plasma rotation.

For the ion cyclotron resonance heating scenarios, a clear change in toroidal rotation is as well observed. In this case, the key plasma parameter is the minority heating concentration amplitude.

- At low minority concentration (3%), a counter-current rotation increment is seen over the whole profile with a maximum effect of about ~ -30 km/s, while at high minority concentration (7%) a co-current increment of about +10 km/s is observed for the whole profile as well. Our studies of ICRH rotation confirms the first experimental results already obtained for the central toroidal rotation, but also complete those analyses with new results which provided a better understanding of rotation with ICRH in Tore Supra. Nevertheless, the observed rotation changes at low and high minority heating are different in terms of amplitudes from the previous analysis. In our study increments of -30 km/s resp. +10 km/s at low and high minority concentrations are observed while in (S.Assas, 2004) opposite amplitudes with -10 km/s resp. +25 km/s at low and high

minority concentrations were reported. It is important to point out that the rotation measurement technique is different between the two studies.

The preliminary analysis of the mechanisms behind these effects shows that:

- The counter current increments observed at low minority concentration are consistent with the fast ion ripple losses and the neoclassical friction in terms of direction and amplitude. The co-current trend at high minority concentration is believed to be consistent with the momentum turbulent transport. Numerical simulations are necessary to demonstrate this mechanism.

The obtained results can be compared to the experimental observations in other machines such as C-Mod and JET. At C-Mod the two trends at low and high plasma current were observed during LHCD with increments of about 30 km/s. The Reynolds stress through the residual stress contribution is expected to be the dominant mechanism to explain the experimental results. This can be confirmed using the same approach as developed in this thesis with numerical simulations of turbulent momentum flux. At JET, the intrinsic toroidal rotation analysis during LHCD shows co-current rotation profiles at low plasma current, while at high plasma current, the data are not available so far. For the ICRH scenarios co-current rotation profiles in the plasma core have been observed at JET and C-Mod. Co-current rotation increments were also reported in these two machines. This effect is likely related to the angular momentum transport which could be the dominant factor to explain the rotation profiles.

Perspectives for future work

According to the work achieved in this thesis, understanding the intrinsic rotation requires the identification of all elementary mechanisms at play, and the estimation of their impact on the intrinsic rotation. The subtle interaction of the different mechanisms in competition indicates the difficulties involved in estimating the resulting effect and extracting the dominant mechanisms. Nevertheless, the large variety of mechanisms inducing intrinsic rotation in the plasma supposes strong intrinsic rotation for future machines. To establish confident models and make predictions, a complete analysis of the intrinsic rotation mechanisms is necessary. It appears in this thesis that one of the main challenges is the angular momentum transport modelling. Hence, accurate momentum transport simulations with high calculation level over the whole plasma profile are primordial issues to resolve the rotation evolution in the plasma. To achieve that, both more extensive databases and theoretical developments are needed.

La science exige la sagesse car elle débouche sur la technique qui est un pouvoir d'agir. La science rend possible la sagesse en ouvrant idéalement sur la liberté. La science un plaisir gratuit et naturel à l'homme chez qui « la passion de connaître » est naturelle.

[...] de même que nous appelons libre celui qui est à lui-même sa fin et n'existe pas pour un autre, ainsi cette science [la connaissance pure] est aussi la seule de toutes les sciences qui soit une discipline libérale, puisque seule elle est à elle-même sa propre fin.

Aristote

Bibliography

A. Becoulet et al. [Revue]. - [s.l.] : Nucl. Fusion 53 104023 (17pp), 2013.

A. Ekedahl et al. Thermal and non-thermal particle interaction with the LHCD launchers in Tore Supra [Revue]. - [s.l.] : Journal of Nuclear Materials 363–365, 2007. - Vol. 1329–1333.

A. Fukuyama et al. Transport simulation on L-mode and improved confinement associated with current profile modification [Revue] // PPCF 37 611431. - 1995.

A. Grosman et al. [Revue]. - [s.l.] : Fusion Engineering and Design, http://dx.doi.org/10.1016/j.fusengdes.2013.02, 2013.

A. Kallenbach et al. Characterization of the angular momentum transport in ASDEX [Revue]. - [s.l.] : Plasma Physics and Controlled Fusion, vol. 33 (6) pp. 595–605, 1991.

A. Romannikov et al. Measurement of central toroidal rotation in ohmic Tore Supra plasmas [Revue]. - [s.l.] : Nuclear Fusion, Vol. 40, No. 3, 2000.

A. Scarabosio et al. [Revue]. - [s.l.] : Plasma Phys. Control. Fusion 48 663, 2006.

A.B. Michailovskii et al. [Revue]. - [s.l.] : plasma Physics Reports 21 529, 1995.

A.D. Whiteford et al. CXSFIT user manual [Revue]. - 2007.

A.G. Peeters [Revue]. - [s.l.] : Phys. Rev. Lett. 98 265003, 2007.

A.G. Peeters et al. [Revue] // Phys. Rev. Lett 98. - 2007. - 265003.

A.L. Rogister et al. [Revue]. - [s.l.] : Nucl. Fusion 42 1144, 2002.

A.M.Garofalo et al. [Revue] // Fusion 41 1171. - 2001.

A.V. GUREVICH and Ya. S. DIMANT KINETIC THEORY OF RUNAWAY PRODUCTION IN TOROIDAL MAGNETIC DEVICES [Revue] // NUCLEAR FUSION 18 5. - [s.l.] : Nuclear Fusion 18 5, 1978. - http://iopscience.iop.org/0029-5515/18/5/003/pdf/0029-5515_18_5_003.pdf.

B P. Duval et al. [Revue] // EXS/P4-01.

B. A. Grierson et al. Measurements of the deuterium ion toroidal rotation in the DIII-D tokamak and comparison to neoclassical theory [Revue] // PHYSICS OF PLASMAS 19, 056107. - 2012.

B. Chouli et al. [Revue] // PPCF. - [s.l.] : accepted in PPCF, 2014.

B. Coppi et al. [Revue]. - [s.l.] : Nucl. Fusion 42 1, 2002.

B. LaBombard et al. [Revue]. - [s.l.] : Nucl. Fusion 44 1047, 2004.

B.B. Kadomtsev [Revue]. - [s.l.] : Sov. J. Plasma Phys. 1 389, 1975.

B.P. Duval et al. [Revue]. - [s.l.] : Physics of Plasmas 15 056113, 2008.

B.P. Duval et al. IAEA [Revue]. - 2010.

C. Bourdelle et al. [Revue] // Phys. Plasmas, 14 112501. - 2007.

C. Fenzi et al. [Revue]. - [s.l.] : EPS conference, 2013.

C. Fenzi et al. [Revue] // EPS (Strasbourg). - 2011.

C. Fenzi et al. Improved charge exchange recombination spectroscopy measurements in Tore Supra [Revue] // Rev. Sci. Instrum. - 2011. - submitted.

C. Fenzi et al. Improved charge exchange recombination spectroscopy measurements in Tore Supra Rev. Sci. Instrum. [Revue] // Submitted. - 2014.

C. Fenzi et al. On plasma rotation with toroidal magnetic field ripple and no external momentum input [Revue] // Nucl. Fusion . - 2011. - 103038 : Vol. 51 .

C. Gil et al. TORE SUPRA DIAGNOSTIC SYSTEMS [Revue]. - [s.l.] : FUSION SCIENCE AND TECHNOLOGY VOL. 56 , 2009.

C. Marini et al. Impurity density and momentum transport during the sawtooth cycle [Revue]. - Berlin : 41st EPS conference on plasma physics (P5.023), 2014.

D. Guilhem et al. Passive active multi-junction 3.7 GHz launcher for Tore-Supra long pulse experiments: manufacturing process and tests Proc [Revue] // 18th Topical Conf. on Radio Frequency Power in Plasmas AIP Conf. Proc. 1187 435–8. - Gent, Belgium : [s.n.], 2009.

D. J. Tritton Physical Fluid Dynamics [Revue]. - [s.l.] : International Student Edition, 1977.

D. Testa et al. On the measurement of toroidal rotation for the impurity and the main ion species on the Joint European Torus [Revue] // PHYSICS OF PLASMAS vol 9. - 2002.

D. van Houtte et al. [Revue] // Nucl. Fusion 44 L11. - [s.l.] : Nucl. Fusion, 44, L11 , 2004.

David.JC. Mackay Sustainable energy without hot air [Rapport]. - [s.l.] : UIT Cambridge UK, ISBN 978-0-9544529-3-3, 2009.

deGrassie J. S. [et al.] [Revue] // Nucl. Fusion 49. - 2009. - 085020.

deGrassie J. S., Baker D. R. et K. H. Burrell et al. Toroidal rotation in neutral beam heated discharges in DIII-D [Revue]. - [s.l.] : Nuclear Fusion, vol. 43 pp. 142–156 , 2003.

DOI-EIA US department of energy International energy Annual 2010 [Rapport]. - 2010.

Dr. Pieter Tans [Rapport]. - [s.l.] : NOAA/ESRL.

E. Doyle et al. [Revue] // Nucl. Fusion 47 S18–S127. - 2007.

E. Lazzaro et al. Anomalous braking and shear modification of plasma rotation in a tokamak Proc [Revue] // 29th EPS Conf.. - 2002. - Vol. Vol 26B. - pp. P-5.079.

E. Nilsson et al. Comparative modelling of lower hybrid current drive with two launcher designs in the Tore Supra tokamak [Revue] // Nucl. Fusion 53 083018 (9pp). - 2013.

E. Viezzer et al. High-accuracy characterization of the edge radial electric field at ASDEX Upgrade [Revue] // Nucl. Fusion 053005 (13pp). - 2013. - p. 53.

Equipe Tore Supra [Revue]. - [s.l.] : Proc. 12th Int. conf. Nice. IAEA, Vienna (1989), 1998. - Vol. 1.

F. A. Karelse et al. Measurements of the current density profile with tangential Thomson scattering in RTP [Revue]. - [s.l.] : Plasma Physics and Controlled Fusion, vol. 43 pp. 443–468, 2001.

F. C. Schuller Profile consistency as a result of coupling between the radial profile functions of pressure and current density [Revue]. - [s.l.] : 18th EPS Conference on Controlled Fusion and Plasma Physics in ECA, 1991.

F. Clairet et al. [Revue] // Rev. Sci. Instrum. 81 10D903. - 2010.

F. F. Chen [Revue]. - [s.l.] : Plasma Physics and Controlled Fusion, vol. 1. Pl. Press N.Y., 1993.

F. Imbeaux et Y. Peysson et al. Ray-Tracing and Fokker-Planck modelling of the effect of plasma current on the absorption and propagation of Lower Hybrid waves [Revue] // Plasma Physics and Controlled Fusion 47 No 11 2041-2065. - 2005.

F. Joos The atmospheric Carbone Dioxide perturbation [Rapport]. - [s.l.] : Europhysics news 27 6 213-218, 1996.

F. L. Hinton and R.D. Hazeltine Theory of plasma transport in toroidal confinement systems [Revue]. - [s.l.] : Rev. Mod. Phys. 48 239-308, 1976.

F. Wagner etal. Regime of Improved Confinement and High Beta in Neutral-Beam-Heated Divertor Discharges of the ASDEX Tokamak [Revue]. - [s.l.] : Physical Review Letters, vol. 49 (19) pp. 1408–1412, 1982.

F.W. Perkins et al. [Revue]. - [s.l.] : Phys. Plasmas 8 2181, 2001.

F.W. Perkins ICRH Heating Theory [Revue]. - [s.l.] : IEEE Transactions on Plasma Science, 12,53-63, 1984.

G M. Staebler et al. [Revue] // Physical Review Letters. - 2013. - 110 ISSN 0031-9007.

H. A. Claassen et al. Neoclassical theory of rotation and electric field in high collisionality plasmas with steep gradients [Revue]. - [s.l.] : Physics of Plasmas,vol. 7 (9) pp. 3699–3706, 2000.

H. Biglari et al. Influence of sheared poloidal rotation on edge turbulence [Revue]. - [s.l.] : Physics of Fluids B, vol. 2 (1) pp. 1–4, 1990.

H. Kuus et al. The ICRH system for Tore Supra [Revue]. - [s.l.] : Proc. 15th SOFT, 1988.

I. Cook et al. Safety and Environmental impact of Fusion [Rapport]. - [s.l.] : CCE-FU/FTC 8/9 , 2001.

ITER Physics basis Chapter 2: Plasma confinement and transport [Revue]. - [s.l.] : Nuclear Fusion vol. 39 pp. 2175–2249, 1999.

J. Bernardo et al. Density impact on toroidal rotation in Tore Supra: Experimental observations and theoretical investigation [Revue] // Plasma Phys. Control. Fusion. - [s.l.] : Accepted from PPCF, 2013. - Submitted.

J. Bucalossi et al. [Revue]. - [s.l.] : Fusion Engineering and Design 86 684–688., 2011.

J. Citrin et al. Quasilinear transport modelling at low magnetic shear [Revue] // PHYSICS OF PLASMAS 19, 062305. - 2012.

J. Decker Y. Peysson A fast numerical solver for the 3D drift kinetic equation [Revue] // Report EUR-CEA-FC-1736 Euratom-CEA. - 2004.

J. E. Rice et al. Toroidal rotation and momentum transport in Alcator C-Mod plasmas with no momentum input [Revue] // Phys. Plasmas. - 2004. - 5 : Vol. 11.

J. Hedin et al. [Revue]. - [s.l.] : Nucl. Fusion 42 527, 2002.

J. JACQUOT Description non-linéaire auto-cohérente de la propagation d'ondes radiofréquences et de la périphérie d'un plasma magnétisé [Revue]. - [s.l.] : PhD thesis, 2013.

J. Rice et al. [Revue] // Nucl. Fusion 49 025004. - 2009.

J. Rice et al. Effects of Magnetic Shear on Toroidal Rotation in Tokamak Plasmas with Lower Hybrid Current Drive [Revue] // PRL 111,125003. - 2013.

J. Rice et al. Inter-machine comparison of intrinsic toroidal rotation in tokamaks [Revue] // Nucl. Fusion 47 1618–1624. - 2007.

J. Wesson Tokamaks [Revue]. - [s.l.] : Oxford University Press, Great Clarendon Street, Oxford OX2, 1997. - Vol. 6DP, 2nd edn.

J.D. Callen Effects of 3D magnetic perturbations on toridal plasmas [Revue]. - [s.l.] : Nucl. Fusion 51 094026 (13pp), 2011.

J.E. Rice et al. [Revue]. - [s.l.] : Nuc. Fusion 51 083005, 2011.

J.E. Rice et al. [Revue]. - [s.l.] : Nuclear Fusion, Vol. 39, No. 9 , 1999.

J.E. Rice et al. Central impurity toroidal rotation in ICRF heated Alcator C-Mod plasmas [Revue] // Nuclear Fusion. - No. 9 : Vol. Vol. 39.

J.E. Rice et al. Effects of LHRF on Toroidal Rotation in Alcator C-Mod Plasmas [Revue] // Nuclear Fusion 53 093015. - 2013.

J.L.Segui et al. [Revue] // Rev. Sci. Instrum., 76, 123501. - 2005.

J.M. Berger et al. Heating of a Confined Plasma by Oscillating Electromagnetic Fields [Revue]. - [s.l.] : Physics of Fluids, vol. 1 (4) pp. 301–307, 1958.

J.M. Kwon et al. [Revue] // Nucl.Fusion.. - [s.l.] : Nucl. Fusion 52 013004, 2012.

J.P.Holdren et al. Summary of the report of the senior committee on environmenta safety and economic aspects of magnetic fusion energy [Rapport]. - [s.l.] : Lawrence Livermore National Laboratory Report UCRL-53766 , 1987.

J.W. CONNOR et J. G. CORDEY [Revue]. - [s.l.] : NUCLEAR FUSION 14, 1974.

J.W.S. Blokland et al. MHD equilibrium reconstruction for TEXTOR: from static to stationary equilibria [Revue]. - [s.l.] : 32nd EPS Conference on Plasma Phys. Tarragona, ECA Vol.29C, P-4.070, 2005.

J-F. Artaud et al. [Revue] // Nucl. Fusion 50 043001. - 2010.

K.H. Burrell et al. [Revue] // Science 281 1816. - 1998.

L. Vermare et et al. [Revue]. - [s.l.] : Nucl. Fusion 46 S743–S759, 2006.

L.M. Kovrizhnykh Plasma rotation in rippled tokamaks and stellarators [Revue]. - [s.l.] : Plasma physics reports 25 10, 1999.

L.R. Baylor et al. Comparison of toroidal rotation velocities of different impurity ions in the DIII-D tokamak [Revue]. - [s.l.] : Physics of Plasmas, vol. 11 (6) pp. 3100–3105, 2004.

L.Wang and P.H.Diamond Gyrokinetic Theory of Turbulent Acceleration of Parallel Rotation in Tokamak Plasmas [Revue] // PRL 110, 265006. - 2013.

L-G Eriksson et al. [Revue] // Plasma Phys. Control. Fusion 43 . - 2001. - 1291–1302.

L-G Eriksson et al. Plasma Phys. Control. Fusion [Revue]. - 1997. - Vol. 39. - pp. 27–42.

L-G. Eriksson and F. Porcelli [Revue]. - [s.l.] : Nucl. Fusion 47 1618, 2002.

L-G. Eriksson et al. [Revue] // Plasma Phys. Control. Fusion 51 044008. - 2009.

L-G. Eriksson et al. [Revue]. - [s.l.] : Phys. Rev. Lett. 92 235001, 2004.

L-G. Eriksson et al. [Revue] // Nucl. Fusion 41 91. - 2001.

L-G. Eriksson et al. [Revue]. - [s.l.] : Plasma Phys. Control. Fusion 34 863, 1992.

M. Brambilla Kinetic theory of plasma wave [Revue]. - [s.l.] : Oxford science publications, 1998.

M. De Bock Understanding and controlling plasma rotation in tokamaks [Revue]. - [s.l.] : PhD thesis , 2006.

M. Greenwald et al. [Revue] // Phys. Rev. Lett. 53, 352–355. - 1984.

M. Irishkin et al. Automated comparison of experimental density profile reconstruction with models [Revue] // submitted to PPCF. - 2014.

M. Lipa et al. [Conférence]. - [s.l.] : Fusion Engineering (Proc. 17th Symp. San Diego, 1997), Vol. 1), 1997.

M. Schneider et al On alpha particle effects in tokamaks with a current hole [Revue]. - [s.l.] : Plasma Phys. Control. Fusion 47 2087, 2005.

M. Singer World Population Prospects : the 1994 Revision. United Nations [Revue]. - [s.l.] : La Recherche, 3 2 7 , 84-86, 2000.

M. von. Hellermann et al. Analytical approximation of cross section effects on charge exchange spectra observed in hot fusion plasmas [Revue]. - [s.l.] : Plasma Physics and Controlled Fusion, vol. 37 71–94, 1995.

M.G von Hellerman CXSFIT user manual [Rapport]. - 2007.

M.N. Rosenbluth et al. [Revue]. - [s.l.] : Plasma Physics and Nuclear Fusion Research vol 1 (IAEA Vienna) p 495, 1971.

N. Isei A. Isayama et al., 'Electron Cyclotron Emission Measurements in JT-60U' [Revue] // Fusion Eng. Design 213. - 2001.

N. Kluy et al. Linear gyrokinetic calculations of toroidal momentum transport in the presence of trapped electron modes in tokamak plasmas [Revue] // PHYSICS OF PLASMAS 16, 122302. - 2009.

N. Nakicenovic et al. Global Energy Perspectives [Revue]. - [s.l.] : IIASA and World Energy Council, Cambridge University Press 1998.

National Institute for Standards and Technology NIST Atomic Spectra Database [Revue].

Ö. D. Gürcan et al. [Revue]. - [s.l.] : PHYSICS OF PLASMAS 17, 112309, 2010.

O.D. Gurcan et al. [Revue] // Phys. Plasmas14. - [s.l.] : PHYSICS OF PLASMAS 14, 042306, 2007. - 042306.

P. Bayetti etal. [Revue]. - Utrecht, The Netherlands : Proc. 15th Symp. Fusion Technology (SOFT), 1988. - 604.

P. Cottier et al. Angular momentum transport modeling: achievements of a gyrokinetic quasi-linear approach [Revue] // PPCF submitted . - 2013.

P. Garin [Revue]. - [s.l.] : Fusion Engineering and Design 49–50 89–95, 2000.

P. Garin et al. CIEL, a New Breath for Tore Supra [Revue]. - [s.l.] : 20th SOFT, September 7–11, Marseille, France, 1998.

P. Helander and D.J. Sigmar collisional transport in magnetised plasmas (Cambridge University press) [Revue]. - 2002.

P. Hennequin et al. Fluctuation spectra and velocity profile from Doppler backscattering on Tore Supra [Revue]. - [s.l.] : Nucl. Fusion 46 S771–S779, 2006.

P. Maget et al. [Revue]. - [s.l.] : Plasma Phys. Control. Fusion 47 357–377, 2005.

P. Platz et al. [Revue]. - [s.l.] : RSI 701 308, 1999.

P.H. Diamond et al. [Revue] // PD/P8-19. - 2013.

P.H. Diamond et al. [Revue] // Nucl. Fusion 49. - [s.l.] : Nucl. Fusion 49 045002 (11pp), 2009. - 045002.

P.H. Diamond et al. [Revue]. - [s.l.] : Phys. Plasmas 2 3640, 1995.

P.J. Catto and A.N.Simakov [Revue]. - [s.l.] : Phys. Plasmas 11, 90, 2004.

P.N. Yushmanov [Revue] // Review of Plasma Physics. - New York: Consultants Bureau : [s.n.], 1990. - Vol. vol 16.

P.N. Yushmanov Diffusive transportprocesses caused by ripple in tokamaks [Revue].

P.Platz et al. [Revue] // 22nd European Physical Society Conference on Plasma Physics and Controlled Fusion, Bournemouth,Vol. 19C Part III-337.. - 1995.

R. C. Isler An overview of charge-exchange spectroscopy as a plasma diagnostic [Revue]. - [s.l.] : Plasma Physics and Controlled Fusion, vol. 36 171–208, 1994.

R. Cesario et al. [Revue] // Nature commun.1. - 2010. - 55.

R. D. Hazeltine Rotation of a toroidally confined, collisional plasma [Revue]. - [s.l.] : Physics of Fluids, vol. 17 (5) pp. 961–968 , 1974.

R.A. Cairns Radiofrequency heating of plasmas [Revue]. - Bristol : IOP Publishing, 1991.

R.E. Waltz et al. [Revue]. - [s.l.] : Phys. Plasmas 1 2229, 1994.

R.J. Goldston et al. [Revue]. - [s.l.] : Phys. Rev. Lett. 9 647, 1981. - Vol. 47.

R.J. Rutherford and P.H. Goldston Plasma Physics [Revue]. - 1995.

R.W.Conn et al. Economic, safety and environmental prospects of fusion reactors [Rapport]. - [s.l.] : Nucl. Fusion, 30 1919, 1990.

R-J. Hastie et al. [Revue] // Astrophysics and Space Science 256: 177–204. - 1998.

S. Assas et al. Toroidal plasma rotation in ICRF heated Tore Supra discharges [Revue]. - [s.l.] : EPS on plasma physics., 2003.

S. P. Hirshman and D. J. Sigmar [Revue]. - [s.l.] : Nuclear Fusion, vol. 21 pp. 1079–1230, 1981.

S.Assas Dynamique des ions suprathermiques et rotation toroidale des plasma de tokamak chauffés par des ondes FCI [Revue]. - [s.l.] : PhD Thesis P. 177, 2004.

S.I. Braginskii [Revue]. - [s.l.] : Reviews of Plasma Physics (Consultants Buraeu, New York), 1965.

T. H. Stix Decay of poloidal rotation in tokamak plasma [Revue]. - [s.l.] : Physics of Fluids, vol. 16 (3) pp. 1260–1267, 1973.

T.E. Stringer et al. [Revue] // Nucl. Fusion 12 689. - 1972.

T.S. Hahm et K.H. Burrell [Revue]. - [s.l.] : Phys. Plasmas 2 1648, 1995.

United Nations Energy Statistics Yearbook 2009 [Rapport]. - New York : United Nations, Department of Economic and Social Information and Policy Analysis, Statistical Division, 2009.

V. Basiuk et al. [Revue] // Nucl. Fusion 35 12. - 1995.

V. Basiuk et al. [Conférence]. - Geneva : European Physical Society 16C, 1992.

V. Basiuk et al. Studies of suprathermal electron loss in the magnetic ripple of Tore Supra [Revue] // Nuclear Fusion, Vol. 41, No. 5. - 2001.

V. Basiuk et al. Studies of suprathermal electron loss in the magnetic ripple of Tore Supra [Revue] // Nuclear Fusion, Vol. 41, No. 5. - 2001.

W. Zwingmann Equilibrium analysis of steady state tokamak discharges [Revue]. - [s.l.] : Nucl. Fusion 43 842–850, 2003.

www.bp.com Statistical review of word energy 2009 [Revue]. - 2009.

X. Garbet et al. [Revue]. - [s.l.] : PHYSICS OF PLASMAS 20, 072502, 2013.

X. Garbet et al. [Revue] // Physics of Plasma, 072505. - 2010. - p. 17.

X. Garbet et al. [Revue]. - [s.l.] : Phys. Plasmas 9 3893, 2002.

X. Guan et al. On the toroidal plasma rotations induced by lower hybrid waves [Revue] // Phys. Plasmas 20. - 2013. - 022502.

Y. Camenen et al. [Revue]. - [s.l.] : Phys. Rev. Lett. 102 125001, 2009.

Y. Peysson and J. Decker [Revue] // Fusion Science and Technology. - 2014. - Vol. 65.

Y. Peysson et al. [Revue] // Plasma Phys. Control. Fusion 42 B87. - 2000.

Y. Peysson et al. [Revue] // Physics of Plasmas 3 , 3668. - 1996.

Y. Peysson F. Imbeaux, Tomography of the fast electron bremsstrahlung emission during lower hybrid current drive on TORE SUPRA [Revue]. - [s.l.] : Rev. Sci. Instrum., vol. 70 n°10 , p.3987-4007., 1999.

Y. Peysson J. Decker and L. Morini [Revue] // Plasma Phys. Controlled Fusion . - 2012. - 045003 : Vol. 54.

Y.A Podpaly et al. [Revue] // PSFC/JA-11-30. - [s.l.] : PhD thesis MIT, 2011.

Y.B. Kim et al. Neoclassical poloidal and toroidal rotation in tokamaks [Revue]. - [s.l.] : Physics of Fluids B, vol. 3 (8) pp. 2050–2060, 1991.

Y.Sakamoto et al. [Revue] // Plasma Phys. Control. Fusion 48 A63. - 2006.

Y.Shi et al. [Revue] // Phys. Rev. Lett. 106 235001. - 2011.

Ya. Kolesnichenko et al. [Revue] // Nucl.Fusion 40 1326. - 2000.

Z. Gao and N. J. Fisch [Revue] // PHYSICS OF PLASMAS 18. - [s.l.] : PHYSICS OF PLASMAS 18, 082507, 2011. - 082507.

Z. Lin et al. [Revue]. - [s.l.] : Phys. Rev. Lett 83 3645, 1999.

Z. Lin et al. Turbulent transport reduction by zonal flows: Massively parallel simulations [Revue]. - [s.l.] : Science, vol. 281 pp. 1835–1837, 1998.